Matthieu B. Rhomberg

OPTIMIZING THE STRUCTURAL LIFETIME OF MONOPILE-BASED OFFSHORE WIND TURBINES WITH GENETIC ALGORITHMS: IS IT WORTH PLANNING FOR LIFETIME EXTENSION?

MASTER THESIS

Graduation Committee:

Prof. Dr. A. Metrikine	TU Delft
Prof. Dr. M. Muskulus	NTNU
Dr. E. Lourens	TU Delft
Dr. F. Pisanò	TU Delft
Dr. ir. K.N. van Dalen	TU Delft
L. Ziegler, M.Sc.	Rambøll

Delft University of Technology
Faculty of Mechanical, Maritime and Materials Engineering

Norwegian University of Science and Technology
Faculty of Engineering

Salzburg, September 2017

TU Delft Delft University of Technology
RAMBØLL
EWEM
NTNU – Trondheim Norwegian University of Science and Technology

Supervisors:

Professor Dr. Andrei Metrikine, Delft University of Technology, Faculty of Civil Engineering and Geosciences, Department of Hydraulic Engineering, Section Offshore Engineering

Professor Dr. Michael Muskulus, Norwegian University of Science and Technology, Department Civil and Environmental Engineering

Assistant Professor Dr. Eliz-Mari Lourens, Delft University of Technology, Faculty of Civil Engineering and Geosciences, Department of Hydraulic Engineering, Section Offshore Engineering

Lisa Ziegler M.Sc., PhD Candidate Rambøll Wind&Towers Hamburg

Abstract

Optimization of structures in a domain with large uncertainties is rather difficult. This also applies for the offshore wind energy sector. For current offshore wind energy development locations with monopile-based support structures the fatigue limit state is the driving design criteria. These analyses are connected with long time domain evaluations to cover non-linearities. Model, statistical and data uncertainties lead to a combined fatigue damage prediction uncertainty. The former are either covered by a design fatigue factor or a material factor, which are stated in certification standards, e.g. DNVGL-ST-0126. The influence of mass changes regarding different lifetimes and the impact of this design fatigue factor has not been published yet.

Based on this, within this graduation project, the monopile support structure is optimized for different lifetimes in order to identify mass changes and influences of the design fatigue factor. Literature shows that automatized optimization using genetic algorithms in offshore wind energy is possible but limited, due to the algorithm methodology including a large number of design evaluations. This graduation project shows the applicability of Importance Sampling for load case reduction in a genetic algorithm optimization for offshore wind. Compared to previous approaches Importance Sampling assists to use a full certification procedure for fatigue limit state computations in a feasible amount of time with high fatigue life estimation accuracies. Subsequently, the fatigue limit state load case table is reduced by 93%. By optimizing the monopile with this reduced amount of load cases the algorithm is computationally feasible for the industry.

Rambøll simulation software for offshore wind turbine support structure design is used in combination with the genetic algorithm function in Matlab®. The combination of the software leads to the optimization of monopile based offshore wind support structures for different lifetimes. The algorithm runs with a reduced amount of load cases. Resulting critical fatigue damage values of converged designs are showing deviations from actual fatigue damage values using full fatigue limit state load case tables at maximum 6.6% and minimum 1.7%. This high accuracy leads to an optimization of monopile structures for desired lifetimes and consequently to the mass versus lifetime curve. A mass increase of approximately 22% is observed from 25 to 100 years lifetime. After reaching 75 years lifetime the curve shows a flattening behavior. Besides, parameter evolutions of optimized monopile designs are discussed in terms of different fatigue life. The design variables are embedment depth, cone angle, and corresponding wall thicknesses of monopile sections.

Summarized, this thesis proved the implementation of a full state of the art fatigue limit state computation in the genetic algorithm by Importance Sampling with reduced load cases and also visualized the impact of mass changes for different projected lifetimes. As a conclusive remark, the application of Importance Sampling for load case reduction in the design process opens new possibilities of optimization in the offshore wind energy sector.

Acknowledgments

A person I want to thank is my grandfather *A. Weiss*, who mainly contributed to my choice of engineering studies. During hard times one simple expression stayed in my mind, which helped me not to lose sight of the main goal and stay on track:

"Baisse la tête et rentre dans le brouillard."

Various influences by many people from Rambøll and the university helped me to bring this graduation project to a successful end, due to their valuable recommendations, essential suggestions and groundbreaking comments. My Rambøll colleagues influenced this thesis especially with their project experience and also led to discussions that helped me to develop more and also refine my skills, which supported me to get even more attracted to the offshore wind energy domain. In general, I want to thank Rambøll for providing the computational resources and especially the Hamburg office for integrating me into the team from the very first day on. People I especially want to thank are:

Professor Michael Muskulus from NTNU and Lisa Ziegler from Rambøll for their guidance throughout this graduation project, even by being geographically separated. Professor Andrei Metrikine and Dr. Eliz-Mari Lourens for the constructive talks and advices in the progress meetings. These discussions helped in particular to lead this graduation project to success.

Also, I am grateful to have such great parents that made these studies possible and supported me with all their possibilities. Thank you!

My closest friends and my girlfriend also contributed to my success by giving me support and distraction during the whole studies, especially during these intense seven months of thesis work.

Salzburg, September 2017

Matthieu B. Rhomberg

Contents

List of Figures

List of Tables

Nomenclature

Latin	Explanation	Unit
c_b	Genetic Algorithm buckling constraint	[-]
c_t	Genetic Algorithm wall thickness change constraint	[-]
c_{FLS}	Genetic Algorithm fatigue limit state constraint	[-]
c_{f1}	Genetic Algorithm lower soft-stiff frequency	[Hz]
c_{f2}	Genetic Algorithm upper soft-stiff frequency	[Hz]
$\|\|D_{est}\|\|$	Fatigue damage estimation normalized by final true damage	[-]
D_{crit}	Critical fatigue damage weld handed over to GA constraint evaluation	[-]
$\mathbf{D}_k$	Fatigue damage design estimation of the three dimensional monopile including the statistical factors	[-]
$D_{i,top}$	Inner cone top section diameter	[m]
$D_{i,tip}$	Inner cone tip section diameter	[m]
$D_{o,top}$	Outer cone top section diameter	[m]
$D_{o,tip}$	Outer cone tip section diameter	[m]
D^{real}	Fatigue damage value of computed load cases	[-]
D_i^{real}	Fatigue damage value of computed load case i	[-]
D_{fin}^{real}	Final fatigue damage obtained by full fatigue limit state load case table	[-]
D_V	Wind direction	[deg]
$D_{V,W}$	Wind/wave misalignment	[deg]
f_1	Average of first and second monopile natural frequency	[Hz]
f_{RP}	Radial position factors for the factor approach	[-]
f_{CW}	Circumferential weld factors for the factor approach	[-]
f_i	Scaling factor obtained by the division: $D_i^{real}/\overline{\mu}_j$	[-]
$\overline{f}$	Mean value of scaling factors f_i	[-]
$\tilde{f}$	Median of scaling factors f_i	[-]
g_i	Importance Sampling weight	[-]
G_I	Steel monopile block one weight	[ton]
G_{II}	Steel monopile block two weight	[ton]
G_{III}	Steel monopile block three weight	[ton]
$\mathbf{I}_k$	Importance Sampling fatigue damage design estimation of the three dimensional monopile	[-]
k	Accuracy stage in the Importance Sampling fatigue limit state load case reduction	[#]
LC_{HtL}	Highest to lowest standard deviation load case sorting for one one circumferential weld and radial position	[#]
LC_{HtL}^{opt}	Highest to lowest standard deviation load case optimal sorting per radial position	[#]
LC_{HtL}^{Pw}	Highest to lowest standard deviation load case sorting weighted by probability of occurrence and mean value contribution	[#]
LC_{rand}	Randomly selected load case	[#]
L_1	Monopile block one length	[m]
L_2	Monopile block two length	[m]
L_3	Monopile block three length	[m]
t_1	Monopile block one wall thickness	[mm]
t_2	Monopile block two wall thickness	[mm]
t_3	Monopile block three wall thickness	[mm]
V	Wind speed at hub height	[m/s]
V_{in}	Wind turbine cut-in wind speed	[m/s]
$V_{idl,low}$	Lowest design load case 6.4 wind speed	[m/s]
$V_{idl,up}$	Highest design load case 6.4 wind speed	[m/s]
V_{out}	Wind turbine cut-out wind speed	[m/s]

Y_{err}	Wind turbine yaw error	[deg]

Greek	**Explanation**	**Unit**
α	Monopile cone angle	[deg]
ΔV	Wind speed discretization	[m/s]
ΔD_V	Wind speed direction discretization	[deg]
$\Delta D_{V,W}$	Wind/wave misalignment discretization	[deg]
σ_{DMG}	Design set fatigue damage standard deviation per load case	[-]
σ_{est}	Design set fatigue damage estimation standard deviation of accuracy step one	[-]
σ_{ijk}	Fatigue damage estimation standard deviation for GA FLS implementation of stage k	[-]
σ_{est}^{RP}	Design set radial position fatigue damage estimate standard deviation for one circumferential weld of accuracy step two	[-]
σ_{est}^{CW}	Design set circumferential weld fatigue damage estimate standard deviation for one position of accuracy step three	[-]
σ_{est}^{CWRP}	Design set fatigue damage estimate standard deviation for all circumferential welds and radial positions of accuracy step four	[-]
$\overline{\mu}_{DMG}$	Design set fatigue damage mean value per load case	[-]
$\overline{\mu}_{DMG}^{corr}$	Scaled design set fatigue damage mean value per LC	[-]
$\overline{\mu}_{est}$	Design set fatigue damage estimation fatigue damage mean value of accuracy step one	[-]
$\overline{\mu_i}$	Fatigue damage mean value of a computed load case	[-]
$\overline{\mu_j}$	Fatigue damage mean value of all un-computed load cases	[-]
$\overline{\mu}_{est}^{RP}$	Design set radial position fatigue damage estimation mean value of accuracy step two	[-]
$\overline{\mu}_{est}^{CW}$	Design set circumferential weld fatigue damage estimation mean value of accuracy step three	[-]
$\overline{\mu}_{est}^{CWRP}$	Design set fatigue damage estimate mean value for all circumferential welds and radial positions of accuracy step four	[-]

List of Abbreviations

Abbreviation	Explanation
ALS	Accidental limit state
ALT	Actual lifetime
CW	Circumferential weld
CAPEX	Capital expenditure
COE	Cost of energy
CGN	Converged generation number
DFF	Design fatigue factor
DLC	Design load case
DMG	Fatigue Damage
DNV	Det Norske Veritas
FLS	Fatigue limit state
FEM	Finite Element Method
GA	Genetic Algorithm
IFL	Interface level
IS	Importance Sampling
JONSWAP	Joint North Sea Wave Project
LCT	Load case table
MC	Monte Carlo
MP	Monopile
MSL	Mean sea level
NFA	Natural frequency analysis
NSS	Normal sea state
OPEX	Operational expenditure
OWT	Offshore wind turbine
PLT	Projected lifetime
RNA	Rotor nacelle assembly
RP	Radial position on circumferential weld
SE	Super-Element
SLS	Service ability limit state
TP	Transition piece
ULS	Ultimate limit state
WT	Wind turbine

1 | Introduction

Offshore wind energy is gaining territory on the global wind energy market. The offshore location brings new structural and maintenance challenges compared to onshore wind energy, but also advantages due to higher wind speeds leading to higher energy output and no influences by urban planning issues caused by shadowing, noise and alleged view pollution. Ambitious but possible are the offshore wind energy EWEA goals for 2020 and 2030, i.e. 40 GW by 2020 and 150 GW by 2030 [9].

Currently, most selected commissioned offshore wind turbine (OWT) support structure in Europe is, according to the 2015 EWEA report [1], the monopile (MP), see Figure 1.1. There, the cumulative share of wind support structures within the European Union is shown.

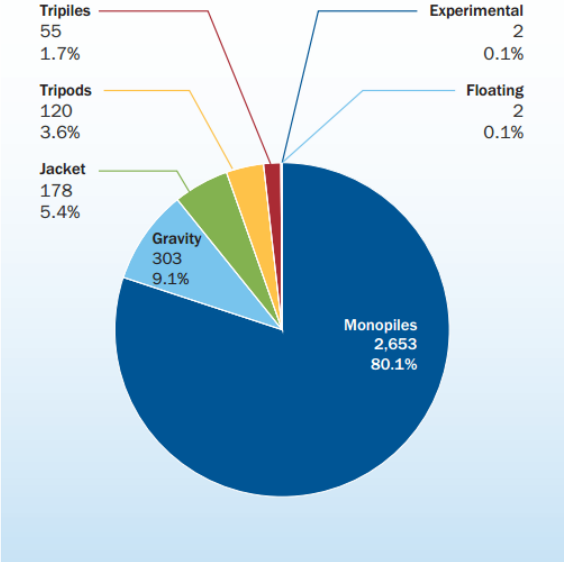

Figure 1.1: *Cumulative wind support structure types within the European Union* [1].

The structure selection is mainly based on the fact that the mean water depth of installed OWT is 22 meters according to a 2013 EWEA report [10]. For this water depth, the MP is a favorable support structure [11]. Optimization and cost reduction of the MP structure is the aim of the wind turbine industry to increase offshore wind energy profitability and competition with other energy resources. Energy profitability is measured by the cost of energy (COE). This parameter can be decreased by lowering expenditures or increasing profit by:

- Reduction of capital expenditures
- Reduction of operation and maintenance expenditures
- Installing larger rated power capacity wind turbines
- Projection for longer lifetimes/life time extension

Capital expenditure (CAPEX) reduction is accomplished by structure optimization and cost reduction in the design, fabrication, installation and de-commissioning period. CAPEX reduction leads to a shift of the financial amortization point towards the commissioning date. This needs to be planned in the design phase, since the influence of costs decreases rapidly after passing this stage.

Operational expenditure (OPEX) reduction deals with the maintenance strategy of the operating wind turbine. Identified strategies taken from [12] are: corrective, preventive, condition-based/predictive and opportunity maintenance. These depend on decisions made in the design process for each wind farm in particular, e.g. harbor distance to shore, wind farm and turbine size. Additionally, many sub-domains are in development for industrial use in offshore wind, such as structural monitoring.

Larger rated power capacities lead to a higher possible energy output with more energy dispensed into the electrical grid. This leads to a higher possible profit.

Lifetime extension or longer projected lifetime due to conservatism and loading uncertainties in design leads to possible extension of profitable years after the financial amortization point.

The four possible COE reduction possibilities influence each other during the design and operation phase. Future trends of projected OWT locations are leading to deeper water depths and larger rated turbine power capacities towards 2018 [1]. Changes in water depth and rated power will lead to new challenges coming hand in hand with new opportunities. On one hand larger turbines lead to more energy output and on the other hand to heavier rotor nacelle assemblies. These heavier rotor nacelle assemblies will subsequently influence the whole design of the support structure. Deeper water depths will increase the share of wave fatigue loading [13], making fatigue damage to the design driving criteria [13, 14, 15]. The MP fatigue damage vulnerability is caused by the close proximity of the structures natural frequencies towards the environmental and operational excitation frequencies.

In terms of design for fatigue damage in offshore wind energy, the process is connected with high uncertainties. Currently, the state of the art in offshore wind structure design for fatigue damage is following specific regulations, determined in DNV-GL-0126 and DNVGL-RP-C203 [6, 8]. There, the characteristic fatigue damage results are emphasized by one specific factor to cover data, statistical and model uncertainties. This factor, called design fatigue factor, is depending on the maintenance strategy and the regarded structural part [6], and is introducing possible conservatism leading to more material consumption, i.e. higher CAPEX. Optimization of OWT MP-based structures is therefore limited by the size of the implemented factor at the end.

1.1 Motivation and Objectives

Optimization of structures for different lifetimes and elaborating the resulting MP mass changes will give an indication of the influence of the design fatigue factor, but also an indication for the worth of higher lifetimes. The automated structure optimization of offshore wind support structures in intermediate water depths is brought to its computation ability limits, since full fatigue limit state (FLS) load case table (LCT) analysis are computationally expensive. This limitation reflects itself in the research completed in the offshore wind domain using the genetic algorithm (GA). Researchers in [16, 17, 18, 19, 20] optimized OWT support structures, i.e. jacket or MP foundations, using the GA. The large amount of design evaluations are tackled by including fatigue and ultimate limit states with reduced LCTs [16, 17, 18]. Additionally, [19, 20] reduced the simulation time per load case of a lumped FLS LCT to 90 seconds. The FLS LCT reductions are justified by assembling a set of governing load cases for a given location. The outcome of load case reduction especially for MP structures is deviating from the full LCT. Subsequently, the GA design evaluations are not completely following the standard regulations [5, 21] for OWT certification.

The graduation project objectives including a MP-based wind support structure optimization by use of the GA are the following:

- Implementation of a FLS LCT reduction technique in the GA with fatigue damage estimation for an accurate MP fatigue lifetime optimization, including time domain simulations following FLS LCT recommendations [5, 21].
- MP optimization with realistic manufacturing requirements, i.e. discrete wall thickness steps.
- Insight into GA performance with changing constraint evaluation, i.e. augmenting accuracy with increasing generation number.
- Setting up a steel mass versus lifetime curve. This curve acts as an indicator for primary steel masses between different optimized MP lifetimes and for the worth of higher design lifetimes.

The implementation of current FLS state of the art LCT in the GA is contributing to current offshore wind energy research. This implementation will help to find optimized MP structures for specific lifetimes and answer the research question:

Is it worth planning for lifetime extension for monopile-based offshore wind turbines?

The project is completed by connecting the Rambøll analysis software with the GA function in Matlab® serving as the main operating tool. The GA optimizes a MP-based OWT taken from a Rambøll reference project. Long GA FLS LCT design evaluations are tackled with cluster computation and FLS LCT reduction, including fatigue damage estimation.

1.2 Project Structure

Chapter two gives relevant background information about current state of the art in OWT support structure design and the large optimization space of MP-based OWT. In addition, the GA general functionality description is presented.

Chapter three deals with the implemented GA model description, including the OWT design tools. Subsequently, the methodologies for FLS LCT reduction, including fatigue damage estimation and implementation in the GA optimization are presented. The final section discusses the model and simulation software limitations.

Chapter four compares different FLS LCT reduction techniques with each other. Additionally, different methodologies are tested for FLS LCT reduction implementation in the GA. Subsequently, the best FLS LCT reduction and methodology is implemented in the GA and multiple runs with different projected structure lifetimes are completed. Next, the converged GA MP designs for different lifetimes are compared to full FLS LCT simulations. This full FLS analysis results in the simulated true structure lifetime. Combination of the converged design mass and true structure lifetime leads to the mass versus lifetime curve as indication of mass changes with increasing lifetime.

Chapter five discusses conclusions of obtained results and closes with further research recommendations.

2 | Background

This chapter contains a literature review on structural optimization of monopile-based offshore wind support structures and computational optimization, using evolutionary algorithms.

Firstly, the monopile (MP) support structure is discussed in section 2.1, followed by section 2.2 with current state of the art for designing a MP-based offshore wind support structure. Within this section load and soil modeling practices are introduced. Next, general structural requirements, that an offshore wind turbine (OWT) needs to be designed for, are discussed. Section 2.3 is presenting computational optimization with emphasis on genetic algorithms (GAs).

2.1 Wind Support Structures - Monopile

Figure 2.1 taken from [2], illustrates the main components from a monopile-based OWT.

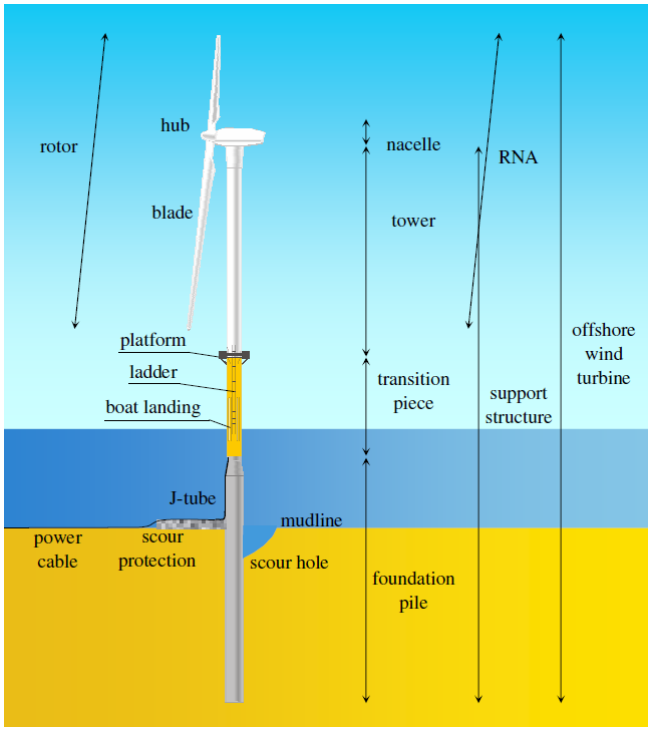

Figure 2.1: *Monopile wind support structure terminology taken from* [2].

The monopile (MP) support structure, suited for shallow to intermediate water depths [11] and soft soils with large horizontal loading [22], is a cylinder on which a transition piece (TP) is mounted [6]. The TP is a connective element between MP and the tower [6]. On the tower top, the rotor nacelle assembly (RNA), containing the nacelle, hub and blades, is fixed, as shown in Figure 2.1. The height of the MP and the TP are site specific and also result from environmental conditions: water depth, soil conditions, wave, wind, current and tide environment [23]. The tower specifications are mostly designed by the wind turbine manufacturer in combination with the RNA and handed over to the foundation designer with fixed lengths and specifications. Starting from the structure-bottom in Figure 2.1 the MP support structure consists of a primary steel tube [6], which ensures to transfer the resulting forces and overturning moment into the soil. The structure is maintained in position by the lateral and the vertical support capacity. The MP with an uniform or multiple diameter and different wall thicknesses over height is rammed into the soil and acts as a cantilever beam. In case of a multiple diameter MP, the sections are connected by a cone section. Cone sections are used to obtain a larger diameter at the mudline. Firstly, due to structural requirements and secondly to keep loading of the structure close to the interface level small. Secondary steel parts, also called appurtenances, are mounted on the primary steel structure to enforce specific parts or for accessibility reasons.

Access to offshore wind turbines is completed by boat or helicopter in case of too high wind and waves [24]. Boat access requires boat landing and ladder constructions at the TP. The helicopter access in [24] is placed on the nacelle top.

The tower is mostly a conical shaped tower with a large diameter on the bottom and a smaller on the top [25]. Firstly, this is due to the fact that the stiffness needs to be increased at the bottom. Secondly, to reduce the oscillating added mass at the top, that would increase loads, i.e. especially the bending moment for the MP close to mudline.

Soil erosion around the pile, due to wave and current, needs to be prevented or accounted for. Since to a certain degree, the integrity of the structure would be endangered by scour, due to a changing geotechnical capacity [6].

Last element shown in Figure 2.1 is the power cable, which is transferring the produced energy to the closest transformation station off-/ or onshore. For most offshore wind turbines the power cable is lead through a steel J-tube above the mudline towards the transformation station [26].

2.2 Structural Optimization of Wind Support Structures

The aim of structural optimization is to create a more efficient and cost reduced structure. The ability of influencing the costs within early stages of the life cycle is high and decreases rapidly as soon as the design is handed over to manufacturing. Therefore the design process is essential for the overall cost evolution.

The cost function of MP-based OWT primary steel can be almost directly related to the weight of the structure, whereas a weight reduction for other structure types, e.g. jacket-type structures, usually is not directly related to lower costs. This is due to possible complicated welding, which is resulting in increased manufacturing costs [14]. A trade-off needs to be completed here to find a safe and in all life cycle stages cost efficient structure.

Examples for cost reduction considerations for OWTs life cycle phases after the concept and design stage are:

- **Manufacturing**: Lowering the costs by using available materials, delivery lengths and thicknesses in accordance with the manufacturer processing capabilities.
- **Transport&Installation**: Costs are dependent on the carrying capacity of available ships in the planned construction period and the required driving energy [14].
- **Operation&Maintenance**: Ensuring structural integrity (static&dynamic) for safe load carrying during operation by selection of an appropriate and economic advantageous maintenance strategy. The latter is influencing the structure in already design phase. There, the design is performed according to maintenance strategies. These are defined by design fatigue factors [6]. During operation monitoring plays an important role to perform the selected operation and maintenance strategy by strain, acceleration and deformation measurements.
- **Decommissioning**: Additional lifetime for decommissioning should be accounted in the design phase, i.e. the structure needs to be safe after the projected lifetime expired until decommissioning is completed. Decommissioning costs are wind farm dependent expenses due to pricing dependency on: wind farm size, vessel carrying capacity, support structure type and distance to feasible storage harbor [27]. Additionally recycling benefits are unknown, e.g. difficulty to predict an accurate steel price decades ahead. Up to now an economically feasible recycling of composite material based wind turbine blades is not possible [28].

The consideration of these cost reduction possibilities in design phase is a strategy to optimize the structure by best means of feasibility and costs for each life cycle phase. The main challenges in design phase for OWTs, repeated from [15] are:

- Complex environment (wind/waves/current) with limited available information interacting with the coupled structure systems [15].
- Design driving fatigue loads, which demand computationally expensive simulations, due to a high amount of load cases [15].
- Overall non-linearities in loading conditions and support structure design [15].

2.2.1 State of the Art

Due to structural dynamic dependency between the OWT support structure and the RNA, an integrated design of the structure is unavoidable. Integrated design is the combined computation of the different structural parts of the offshore wind turbine, such as tower, TP, MP and the wind turbine. This simulates the wind turbine in combination with the interaction of the sea environment on the support structure. A loop of iterations is recommended in order to obtain an optimized structure for the desired lifetime. This design process can be either manually or automatic/computer based.

Hitherto design optimization is completed in a manual way by the empirical knowledge and experience of the engineer. Since time is playing an important role, this manual optimization can only be completed by several iterations. Subsequently, this might lead to an over-designed/conservative structure, but on the other hand the experienced engineer might find an optimized design in a smaller amount of time, compared to computer based optimization.

Nevertheless, within these iterations the structure is analyzed following the standards DNVGL and DNV GL-0126 [21, 6] in two different types of analysis, depending on the regarded design situation:

- Time domain
- Frequency domain

The *time domain* analysis is the required method to analyze offshore structures, because the method is taking the non-linear effects, that are encountered while designing a offshore wind support structure, into account [29]. Hence this method is also the most time consuming method, due to the calculation of the dynamic response for each time increment [29].

For the *frequency domain* OWT applicability, the method requires simplifications, since non-linearities can not be accounted using this method [29]. Therefore, all non-linearities need to be linearized [29], e.g. soil models, wave and current particle velocities in the Morison equation.

Nevertheless, within detail design process, the engineer is referring to the current codes and recommendations, in which current practice for designing the wind turbine and its support structure design are described. Since time domain simulations take non-linear effects into account [29], time domain simulations are required to certify a OWT. The encountered non-linear effects for OWTs are repeated in a summarized manner from [30, 31] hereafter:

- Aero-elastic effects increase the relative wind velocity and thus the thrust [30].
- Blade pitch, soil-structure interaction modeling and rotational speed depending blade dynamics [30].
- Breaking waves in case of large wave heights or shallow water depths [30].
- Second order effects for heavy RNAs that influence the frequency [31]. Due to the influence on the frequency, this effect might have also influences on buckling and fatigue damage.
- Second order effects need to be accounted for large rotor blade displacements [30].

2.2.2 Load and Soil Modeling

The MP presented in section 2.1 is mainly loaded by hydro-and aerodynamic loads. Hydrodynamic MP load modeling is mostly completed by use of the Morison equation. The aerodynamic loading instead, is implemented with a BEM (Blade Element Momentum) code. Soil-structure interaction is inserted in the modeling by non-linear springs.

Hydrodynamic loading - Morison equation

The Morison equation in expression 2.1 taken from [32], shows the discrete wave force dF^w acting on a cylinder segment dS:

$$dF^w = \frac{1}{2}\rho_w C_D^w u|u|DdS + \frac{\pi}{4}\rho_w C_M a D^2 dS \tag{2.1}$$

$$u = u_{wave} + u_{curr} \tag{2.2}$$

dF^{w}	...	Force on pile segment	[N/m]	dS	...	Pile segment	[m]
ρ_w	...	Water density	[kg/m^3]	D	...	Pile diameter	[m]
C_D^w	...	Water drag coefficient	[-]	C_M	...	Inertia coefficient	[-]
u	...	Horizontal particle velocity	[m/s]	a	...	Horizontal particle acceleration	[m/s^2]

In case of water current presence, the current u_{curr} and wave u_{wave} in eq. 2.2 velocities add up as described in [2], and form the new velocity input u for the drag term in eq. 2.1.

Eq. 2.1 consists superimposed drag and an inertia term. For small pile diameters, larger wave steepness and shallow water drag is governing [32]. Hence, it is the inertia component for large pile diameters and small wave steepnesses [32]. The empirical inertial parameter C_M in expression 2.1 has been further evaluated by MacCamy&Fuchs, since the original Morison equation is not taking diffraction into account. Diffraction occurs when the structure influences the incoming waves [2]. The presented solution in [33], modifies the inertial part of the Morison equation in 2.1 to account for diffraction [34]. There the factor C_M, depending on the cylinder diameter D and the wave length λ, is decreasing the inertia contribution of expression 2.1 with increasing MP diameter or decreasing wave length. The limit for a vertical cylindrical structure, below which diffraction needs to be accounted for, is $\lambda/D < 5$ [34, 35].

Aerodynamic loading - Blade Element Momentum

Similar to the hydrodynamic forces the total load on a rotor blade can be split up into two parts, a drag and a lift force. The forces result from the incoming wind speed V_0 and the angle of attack α with respect to the airfoil [2]. Figures in 2.2 and expression 2.3 are taken from [3] and [2].

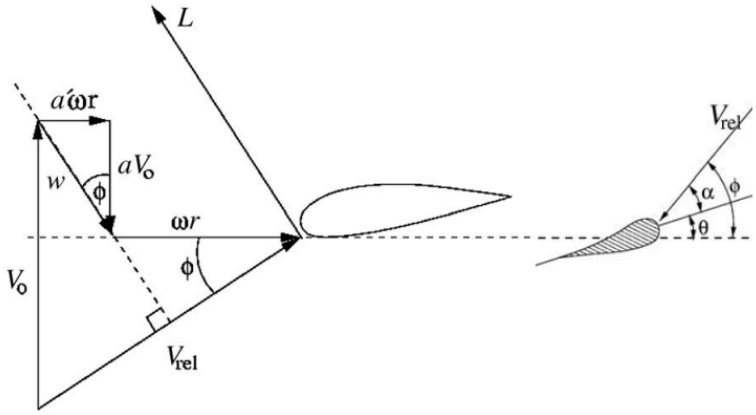

Figure 2.2: *Velocity triangle showing angle of attack α, pitch angle θ and main descriptive parameters taken from* [3] .

$$dF^a = \frac{1}{2}\rho_{air} C_L(\alpha) V_{rel}^2 c \cos(\phi) dr + \frac{1}{2}\rho_{air} C_D^a(\alpha) V_{rel}^2 c \sin(\phi) dr \tag{2.3}$$

dF^a	...	Aerodynamic blade load	[N/m]	ρ_{air}	...	Air density	[kg/^{3}]
c	...	Airfoil cord length	[m]	V_{rel}	...	Relative wind speed at airfoil	[m/s]
$C_D^a(\alpha)$	...	Drag coefficient	[-]	$C_L(\alpha)$	...	Lift coefficient	[-]
α	...	Angle of attack	[deg]	θ	...	Blade pitch angle	[deg]
ϕ	...	Inflow angle	[deg]	V_0	...	Incoming wind speed	[m/s]
a'	...	Tangential induction factor	[-]	a	...	Axial induction factor	[-]
dr	...	Discrete blade element	[m]	ω	...	Rotational speed	[rad/s]

The lift and drag coefficients are a function of the angle of attack with respect to the airfoil of the current blade section. For each airfoil, corresponding lift and drag curves exist.

Soil modeling

One option to account for the soil-structure interaction is by a Winkler (1867) based method, recommended by standards such as API, DNV and ISO. This method is taken as a mean to describe the soil-structure interaction by replacing the linear springs from the original model by uncoupled non-linear springs (p-y curves) [36]. Input

parameters are soil properties of the different soil layers, i.e. variations of sand and clay.

2.2.3 Structural Requirements for the Design - Natural Frequency

Structural requirements are set to maintain a safe operation during the whole lifetime of the structure. Since an OWT is exposed to a highly dynamic environment, the structures frequencies need to be placed outside of the excitation ranges [14].

Primary excitation ranges are defined by the wave and wind frequency spectrum, 1P and 3P region. 1P represents the rotor frequency and 3P the blade passing frequency. The OWTs first natural frequency should not be placed neither in the 1P nor in the 3P region to prevent resonance [2]. This also applies for higher support structure frequencies for multiplicatives of the rotor dynamic regions (3P, 6P, 9P etc. for a three bladed rotor) [37]. The region below 1P is called: soft-soft, the intermediate between 1P and 3P: soft-stiff and above 3P: stiff-stiff [38, 2]. Problems arise in the soft-soft region for ultimate and fatigue limit states, since within this region the wave and wind spectrum are located [38]. Hence, obtaining a MP frequency above 3P requires a large amount of steel and thus is economically expensive [13]. Therefore, the soft-stiff region is the region of interest [39].

For tower optimization the best optimization objective function, according to [40], is the weighted sum of the natural frequencies, i.e. a stiffer structure. The first two natural frequencies of a MP-based OWT are almost compliant, since the first two are representing the bending modes in the horizontal planes. These frequencies are close together, due to the approximately symmetric structure.

2.2.4 Structural Requirements for the Design - Limit States

According to [6] a support structure needs to be checked against fatigue (FLS), ultimate (ULS), service ability and accidental limit states. FLS and ULS are based on load case tables (LCTs) for the verification that the critical component is within the safe limits, while the service ability is taking the highest possible loading of the ULS and verifying that the deflection is not exceeding a certain limit. The accidental limit state, also based on LCTs, need to be defined to cover possible accidental events. More emphasis is put on FLS, since this limit state will be regarded more precisely within this graduation project.

Fatigue Limit State

Fatigue limit states are regarding the failure of the structure due to cyclic loading, i.e. cumulative damage [6]. The fatigue limit state is the design driving criteria, when designing a MP-based OWT in intermediate water depths, due to the highly dynamic environment [13, 14, 15, 41]. Since the whole structure is as strong as its weakest link, FLS is governing at the detail of the structure with the highest fatigue damage.
The following FLS explanation is split into the following characteristic bullet points:

- Load Cases (LCs)
- Stress cycle counting methods
- SN-Curve and Miner sum
- Design Fatigue Factor (DFF)

(a) Load Cases

For design verification, the occurring environment and also situations, that deviate from normal operation, need to be simulated. This ensures to a certain extend that a structure is withstanding the encountered events. For this in standard code IEC-61400 [5], design load cases (DLC) are set as a benchmark to design the structure. These are representing the minimum number of LCs that need to be considered to certify an OWT. Categorization of the latter is completed by different loading situations and are repeated in Table 2.1:

Table 2.1: *Design* LCs *for fatigue summarized from* IEC-61400 [5].

Design Situation	**DLC**	**Wind Condition**	**Directionality**
Power Production	1.2	$V_{in} \leq V_{hub} \leq V_{out}$	COD,MUL
Power Production with fault occurrence	2.4	$V_{in} \leq V_{hub} \leq V_{out}$	COD,UNI
Start-Up	3.1	$V_{in} \leq V_{hub} \leq V_{out}$	COD,UNI
Normal Shut Down	4.1	$V_{in} \leq V_{hub} \leq V_{out}$	COD,UNI
Parked/Idling	6.4	$V_{hub} \leq 0.7 \cdot V_{ref}$	COD,MUL
Parked with fault	7.2	$V_{hub} \leq 0.7 \cdot V_1$	COD,MUL
Transport, assembly,maintenance and repair	8.3	$V_{hub} \leq 0.7 \cdot V_{ref}$	COD, MUL

In IEC-61400 [5] the wave generation for all fatigue LCs presented in Table 2.1, are completed by a normal sea state (NSS). For this peak periods T_p, significant wave heights H_s and the corresponding wind velocities at the wind turbine hub, V_{hub} are required. The latter parameters are from a site specific scatter diagram based on environment measurements. There, the significant wave heights, peak periods and wind velocity combinations are defined with their probability of occurrence in terms of direction.

The abbreviations COD, UNI and MUL used in Table 2.1 are defining the directionality of the combined wind and waves: co-, uni- and multi directional. The directionality takes either a worst case scenario (UNI) or many directions (MUL) into account, to which the resulting loads are depending on the degree of the non-axis symmetry of the structure [5]. The variables V_{in} and V_{out} are the cut-in and cut-out wind speed, i.e. at which the turbine starts/stops the operation. A minimum discretization of ± 2 meters per second for all wind speeds are required according to [5]. The reference wind speed V_{ref} is set as the average velocity of a ten minutes signal and represents the upper limit of the occurring wind speeds.

According to [5] per LC a minimum of six simulations, with a duration of ten minutes, need to be completed. The combined probabilities of a load case P_{10min} with a simulation duration t_{Sim} of 600 seconds each is resulting from the environmental condition probability of occurrence P_{Envi}, up-scaled to the total structure lifetime LT, see expression 2.4. This is completed in order to simulate the occurrences of a specific loading situation during the structures lifetime.

$$P_{10min} = \frac{P_{Envi} \cdot LT}{t_{Sim}} \tag{2.4}$$

Further, OWT availability influences the probabilities. The availability of the turbine is a guarantee of the turbine manufacturer, based on the operation and maintenance strategy, at which share of the total lifetime the wind turbine will be operating. The presented DLC 6.4 is partially resulting by the OWT projected availability for the simulation of a non-operational wind turbine within and outside the range of possible production wind speeds [14]. This DLC is particularly important for the MP fatigue damage, since due to the non-presence of aerodynamic damping during non-operational times the fatigue loading is higher [14].

(b) Stress cycle counting methods

Several methods for cycle counting for stress histories are listed in [42], such as zero crossing, peak, range pair and rainflow counting. Rainflow counting is pointed out to be a more favorable method for welded components in comparison to others [43]. Further information about rainflow counting is found in [44].

(c) SN-Curve and Miner sum

Fatigue detail design is completed by use of SN-curves. These curves are expected to be selected according to DNV-RP-C203 [8] for a given structure by detail geometry, stress direction, fabrication and inspection.

The unmodified SN-curve is a bi-linear line with the negative inverse slope m on a double logarithmic plot, on which the x-axis represents the number of cycles and the y-axis the stress range, usually in Mega Pascal. The basic design SN-curve according to [8] is defined by expression 2.5:

$$\log N = \log(a) - m \log(\Delta\sigma) \tag{2.5}$$

N	...	Number of cycles	[#]
m	...	Negative inverse slope	[-]
$\log(a)$	...	Interception of SN-curve with the x-axis	[m]
$\Delta\sigma$	...	Stress range	[MPa]

Equation 2.5 is extended to expression 2.6, that is taking the plate thickness into account [8]. In equation 2.6, t represents the structure detail plate thickness, t_{ref} the reference thickness and k the thickness exponent [8].

$$\log N = \log a - m \log \Delta\sigma \Big(\frac{t}{t_{ref}}\Big)^k \tag{2.6}$$

The SN-curves in [8], obtained from experiments, are defined with a 2.3% chance of failure, i.e. two times the standard deviation is subtracted from the experiments mean value. The experiments behind the SN-curves are performed by testing small specimens with no stress redistribution possibility until failure by through cracks [8]. According to the DNV-RP-C203 design recommendations [8] fatigue life needs to be checked for different failure cases by pointing out the failure mode: "*weld toe into base material*".

Fatigue damage D_{DMG}, according to the Miner rule (1945) of linear cumulative damage [43], is calculated by combining the stress bins n_i of the loading history with the SN-curve, see expression 2.7:

$$D_{DMG} = \sum_{i=1} \frac{n_i}{N_i} \tag{2.7}$$

For cycles below the fatigue limit, the SN curve can either be linearly extended or the *Haibach* approach can be applied [43]. The latter is the SN-curve slope change due to material degradation by cycles above the fatigue limit [43].

(d) Design Fatigue Factor (DFF)

The calculated characteristic damage D_{DMG} from expression 2.7 is emphasized by a partial safety factor DFF, leading to the design damage [6]. The fatigue damage design requirement is that the cumulative fatigue damage is below one. This DFF is depended on type and accessibility of the structure, maintenance philosophy and applied corrosion protection [6]. The different DFF factors are repeated in a summarized way from [6] in Table 2.2.

Table 2.2: *Design fatigue factors* (DFF) *taken from* [6].

Location	Accessibility [Yes|No]	Value
Atmospheric Zone	Y&N	1|2|3
Splash Zone	Y|N	1|2|3
Submerged Zone	Y|N	1|2|3
Scour Zone	N	3
Below Scour	N	3

Another option for the design damage elaboration is by material factors [6]. According to Table 2.2 the structure below the scour zone needs to be designed for three times the lifetime that the structure is actually designed for, e.g. a structure design life of 25 years results in a MP-below-scour zone design of 75 years. For structure parts that can be inspected, the DFF can be set equal to one or two. The required inspection intervals are computed as follows: the design lifetime divided by three times the applied DFF [6].

This shows the high uncertainty of the fatigue damage prediction, even though many load cases and load situations are considered. Uncertainties reach from the real environmental structure loading uncertainty to uncertainties in the prediction model. Therefore, this factor might lead to a too conservative design. In case it can be certified that the safety level of an lifetime extended structure is given, lifetime extension is feasible. This implies that the fatigue damage of non-inspectable parts are below the margin of the extended lifetime.

Ultimate Limit State

The ultimate limit state of offshore wind support structures is defined in [6] as a ultimate load carrying capacity check. The LCTs include extreme loads with return periods, e.g. one, five and 50 years. According to [6] all elements of a structure need to be checked against amongst other failure criteria:

- Yielding and buckling
- Brittleness

Possible failure modes for yielding and buckling of components need to be considered [6]. Guidance for the design of tubular members is given in the NORSOK standard N-004 [45] by stating a diameter to wall thickness ratio (D/t).

Brittleness must be avoided for the structural parts or a verification of additional resistance must be completed [6]. Since brittle failure may occur abruptly, whereas with ductile failure the structure is redistributing the loads [6] and might be predicted beforehand by measurements and inspections.

Service Ability Limit State

SLS is connected to the deflections and vibrations of the structure or structural elements that might influence the service ability of the structure [6]. A limited permanent structure rotation during the entire lifetime is allowed. This includes an installation and the loading induced rotation tolerance. In general, in case of fulfilling the requirements of ULS and FLS of a wind support structure, the SLS criteria is not the limiting state.

Accidental limit state

The ALS is defined as a resistance verification of a structure during and after the accidental event [6].

2.2.5 Manufacturing Requirements

Parallel to the presented structural requirements in sub-section 2.2.3 and 2.2.4, the design is restricted by the manufacturing requirements. Availability of materials, dimensions and welding ability is essential to keep the costs low or even for feasibility purposes in fabrication. The following information is based on Rambøll project experience:

Firstly, plate thicknesses are only available in discrete and not continuous steps. Costs are kept low by choosing from standard thicknesses. Utilization of non-available thicknesses may cause higher costs, even though the overall steel mass is less, i.e. mainly due to production waiting times of the non-standard plate thicknesses. The MP diameter is rolled from a continuous steel plate.

Secondly, manufacturers are only able to handle a specific maximum dimension and/or weight of a section, depending on their available machinery. These are limited by space and crane capabilities within the factory. A minimum length of a section is also defined to keep the welding costs low. Besides, each wall thickness change requires a different rolled plate and thus includes more welding during fabrication. This rises not only the manufacturing costs, but also increases the amount of locations that are vulnerable to fatigue. These limiting values are defined in the design phase, i.e. when the manufacturer is selected and his capabilities are known.

Thirdly, maximum wall thickness changes are representing a limit at which manufacturers are still able to perform the weld between two sections.

2.2.6 Transport Installation Requirements and Recommendations

The transport and installation possibilities of the MP are mainly restricted by the lifting capacities of the vessel. The lifting capacities depend on the regarded installation vessel and reach from approximately 800 tons up to 5000 tons, i.e. jack-up and floating crane [46]. The current availability of the vessels, as well as driving hammers need to be checked for the current project. From Rambøll project experience the main constraining parameter for MP hammers is the MP top diameter. The diameter difference can be adjusted to a certain extend by a conical piece between hammer and MP. Additionally, hammers need to be selected according to the geotechnical situation on site.

2.3 The Genetic Algorithm

Computational optimization of processes and quantities is used by the industry in many domains, mostly to reduce costs. The main goal of the computational optimization approach is to reach an equal or better result compared to manual iteration of experienced engineers, in equal or smaller amount of time. This approach in engineering practice is brought to a limit due to longer computation times of specific steps [7], e.g. structural analysis. The small allowable time frame, in which the optimizer needs to run through, is defined by the industry pressure to deliver results and offers to clients. Therefore, the main restriction of computational optimizers is time. Having this restriction set, this leads to cut-offs and simplifications of the computational model. These cut offs lead in further steps to a result accuracy influence.

With future increasing computational capacities, todays models may be computed in a smaller amount of time, but since also the analysis models will improve, it will lead to the same issue. Considering this, the

main attention, after setting the design constraints, is to find ways to save computational resources by not losing accuracy of the results. Within the following paragraph the optimization algorithm, namely the genetic algorithm (GA), is presented.

The GA origins from nature, in which the survival of the strongest/fittest is part of the evolutionary process since the beginning of time. Basis of the algorithm are the individuals, which are containing the design variables, and the population, an assembly of individuals in one generation [7]. The fitness function evaluates the individuals along with the constraints, with which the combination of different optimization variables are compared [7]. By procreation, evaluated individuals of a previous generation are forming the following population [7]. For illustrative purposes the general work flow within a GA generation is shown in Figure 2.3:

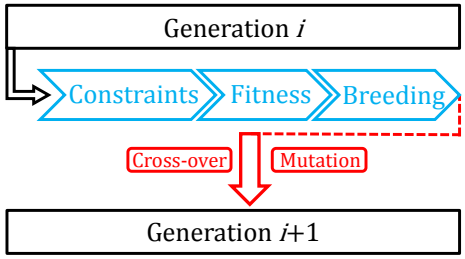

Figure 2.3: *General* GA *work flow within one generation.*

Population

Having a wide population size, the optimization space is covered to a larger extend, but with the drawback that the computation time is increasing [7]. The initial population is created with random values of the optimization variables to envelop a large optimization space [47]. Following populations are created on basis of the previous generation, see Figure 2.3.

Constraints & Fitness

First the variables in $\vec{x}$ that define the fitness function need to be elaborated. The minimization of y in eq. 2.8 by optimizing the variables in the vector $\vec{x}$ is the objective. Therefore, y represents the corresponding fitness evaluation of $\vec{x}$.

$$f(\vec{x}) = \min(y) \tag{2.8}$$

For each optimization problem, the fitness function needs to be defined. The optimization using GAs may be constrained or unconstrained. Unconstrained problems imply that the optimization variables in $\vec{x}$ are not required to fulfill any specific requirements. Hence, a constrained optimization restricts the optimization variables and thus the search space is limited [47]. In case the requirements are not fulfilled the fitness function outcome is penalized [47], i.e. a factor is artificially increasing the value of y.

Breeding

In the breeding stage new individuals are formed for a new generation [7]. This process is consisting three steps: parent selection, crossover and mutation [7]. The selection as a parent of an individual depends on the fitness evaluation and its ranking compared to the other individuals within the population [47]. The most striking selection techniques described in [7, 47] are repeated and summarized below:

- Roulette wheel selection is based on a rotating wheel, divided according to fitness evaluations of individuals within a population [7]. This method may not select the best individuals, due to the random selection [7, 48].
- Random selection selects the individuals randomly and emphasizes that the fittest individuals may not be selected [7].
- Rank selection, ranks the fitness values of the individuals within one population [7]. Later convergence, but diversity is emphasized by this method [7].
- Tournament selection is completed by running tournaments of randomly selected individuals [47]. In each tournament the best individual is selected [7, 49].

Cross-overs are generating new individuals generating after parent selection. Crossing occurs at single or multi-crossover points [7, 47] and is defined by a crossover-mutation ratio [50].

The *Mutation* is an important parameter to keep diversity within the population and the wide search space active [7]. Nevertheless, a large mutation rate would degenerate the GA to a random search, i.e. no links between generations are created [7].

Convergence behavior

The algorithm terminates if one of the following criteria is met:

- Generation limit [7, 47, 49]
- Time limit [7, 49]
- No improvement of best fitness for a set number of generations [7, 47, 49]

Advantages and challenges of the GA are partially repeated from [7] in Table 2.3:

Table 2.3: *Selected advantages and disadvantages of* GAs *repeated from* [7].

Advantage	**Challenge**
+ Parallelism	- Finding the fitness function
+ Applicable in many domains	- Numerous design evaluations
+ Larger optimization space	- Early convergence
+ Not getting stuck in local optima	- Uncertain to find the global optimum

The most striking challenge of the GA is to tackle numerous fitness evaluations [7]. This is an actual problem of the algorithm applicability in engineering design, since each individual usually includes extensive calculations, e.g. a large LCTs or complicated structural analysis models. Therefore, pre-processing work needs to be completed before starting the algorithm to throttle down the computation time by not loosing accuracy.

3 | Primary Steel Optimization

This chapter deals with the model and structure description for a monopile (MP) based offshore wind turbine (OWT) support structure optimization using the genetic algorithm (GA). Section 3.1 presents the model description. There, soil and environment, wind turbine and support structure modeling, as well as load cases (LCs) and used software are presented. Section 3.2 describes the GA implementation in the design process addressing variables, constraints and settings. In section 3.3 fatigue limit state (FLS) load case table (LCT) reduction techniques are presented, followed by Section 3.4 with possible GA FLS LCT implementations. Next, Section 3.5 discusses selected GA tuning parameters. The last Section 3.6 points out model and simulation software assumptions and uncertainties.

3.1 Model Description

3.1.1 Loading, Soil & Environment

The information in this sub-section is obtained from a design basis of a Rambøll reference project. Details about the site and structural features are not listed due to confidentiality.

(a) Loads

Loading on OWTs is a combination of permanent, variable and primarily horizontal environmental loading. Permanent vertical loadings are dead loads originating from structural primary, secondary steel and the rotor nacelle assembly (RNA) mass. Variable loads change in magnitude and location for a short time period regarding the total design life time, e.g. installation or maintenance. Environmental loading originates from wind, waves and current. For this thesis only permanent and environmental loads are included, while variable loadings are disregarded.

(b) Waves & Current

Directional velocities of wind and current as well as tide elevations are taken from a Rambøll reference project with available met-ocean data. The normal sea state for the FLS LCT are defined by a Joint North Sea Wave Observation Project (JONSWAP) spectrum [51] with peak periods and significant wave heights as parameters. The significant wave height is given as a function of wind speed. Subsequently, peak periods are computed from the significant wave heights. With the latter information the JONSWAP spectrum is formed.

(c) Wind

The wind probability distribution is described by a Weibull distribution [52]. Weibull scale and shape parameters, as well as turbulence intensities and standard deviations per wind speed are obtained from the Rambøll reference project. Wind speeds are extrapolated by a power law profile to hub height [52].

(d) FLS Design Load Cases 1.2 & 6.4

Within this graduation project, only fatigue limit state design load cases (DLC) in power production (DLC 1.2) and in idling/non-production (DLC 6.4) [5, 21] are regarded, see sub-Section 2.2.4. The environmental loads are combined for possible design situations within those DLCs as described in sub-Section 2.2.4. In Table 3.1 the LCT creation specifications are listed. There, V represents the wind speed, D_V the wind direction, $D_{V,W}$ the misalignment of wind and wave, and Y_{err} as the nacelle yaw error:

Table 3.1: *DLC 1.2 and DLC 6.4 combinations partially repeated from [5].*

DLC	V [m/s]	Y_{err} [Yes|No]	D_V [Deg]	$D_{V,W}$ [Deg]
1.2	$V_{in} \leq \Delta V \leq V_{out}$	Y	[0,330] $\Delta D_V = 30$	[0,90] $\Delta D_{V,W} = 30$
6.4	$V_{idl,low} \leq \Delta V \leq V_{idl,up}$	N	[0,330] $\Delta D_V = 30$	[0,90] $\Delta D_{V,W} = 30$

The wind velocity discretization ΔV is set to two meters per second and the direction discretization ΔD_V to 30 degrees. In the operational DLC 1.2 the wind velocity limits are the cut-in V_{in} and cut-out V_{out} wind speeds of the wind turbine.

The non-operational DLC 6.4 is partially formed by the non-availability parameter and wind speeds below/above V_{in} and V_{out}, according to wind speed probabilities. Therefore, the DLC 6.4 velocity range reaches from below cut-in to above cut-out wind speed, $V_{idl,low}$ and $V_{idl,up}$. For wind speeds above cut out, the wind turbine blades are pitched out. The water depth for the location is intermediate. Therefore the fatigue damage is expected to be wave-governed [14].

The probabilities of each LC inside the considered DLCs are formed by available met-ocean data. OWT availability is implemented by factorizing the wind speed probabilities by the availability ratio. Subsequently, the total LC probability is obtained by consulting a scatter diagram, including wind speeds and wind/wave misalignment combined with the yaw error probability. For DLC 6.4, no yaw error is included. The resulting LC probability is subsequently scaled to a ten minute duration load as described in eq. 2.4.

(e) Soil

Soil-structure interaction is modeled by a Winkler based non-linear spring model presented in sub-section 2.2.2 from the API recommendation [36]. These include non-linear springs, such as p-y, t-z and q-w for lateral, frictional and tip resistance respectively.

Soil specifications are based on cone penetration tests and laboratory tests (triaxial, oedometer) taken from the Rambøll reference project. General soil composition for this site is a combination of different layers of sand and clay.

3.1.2 Geometrical Definitions

Monopile

The MP is divided into three blocks as illustrated in Figure 3.1:

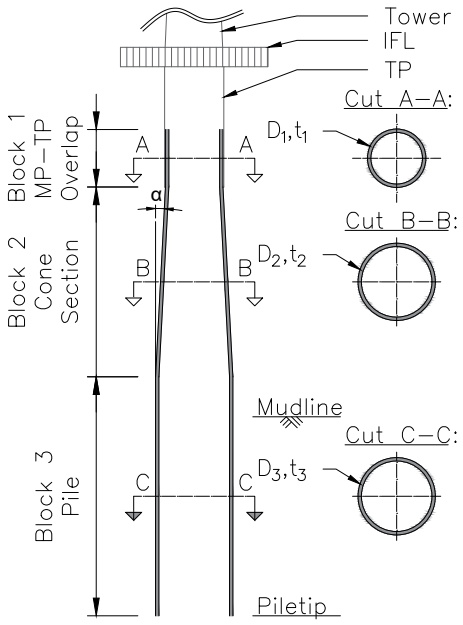

Figure 3.1: *Schematic illustration of the* MP*-model including the transition piece* TP *and the interface level* (IFL).

Block one reaches from the MP top until below the splash zone and the MP-TP overlap. The conical section is forming block two. The third block reaches from the end of the cone section above the mudline until the pile tip. Block one and three are defined by a constant diameter and wall thickness. Block three is depending on the cone angle and length of block two. For more specifications regarding the MP structure see section 2.1.

- *Block* I is defined by the splash zone, for which a upper and an lower limit exists. Those limits are obtained by combining the highest and lowest water level with an occurrence of one year, including 60% and 40%

of the wave height and the vertical installation tolerance [11]. Influences of climate change on the sea level are included in the upper limit. A length tolerance for the MP-TP overlap close to the cone section top is included.

- *Block* II is defined by the cone angle α, a cone length, an upper and a resulting lower diameter. The cone angle α is defined with a minimum of 2.5 up to a maximum of 3 degrees.

- *Block* III is defined by a constant diameter and a wall thickness. The minimum length above mudline is seven meter, due to the cable guidance radius and the peak stress prevention. The maximum length is defined by the drive ability for the given soil conditions.

TP, Tower and Appurtenances

The secondary steel and the platform are included as a fixed added mass distributed along the pile. The implementation of appurtenances is especially important for the hydrodynamic force computation. Access ladders and boat landing are fixed along the TP, cathodic protection along the MP. The corresponding masses and length specifications of secondary steel, platform, TP and tower specifications are taken from a Rambøll reference project and are not part of the optimization. Primary and secondary steel material is considered to be S355 steel with a density of 7850 kg/m^3.

Wind turbine

The RNA is taken from a Rambøll reference project and due to confidentiality issues no further details are given within this report.

3.1.3 Simulation Model Definitions

The Rambøll sequentially design tool is a combination of two simulation programs, namely *Sheila* and *LACFlex*. *Sheila* is the structural analysis execution program and *LACFlex* the wind turbine simulation tool. The steps of the semi-integrated design loop in case of a monopile (MP) geometry modification are illustrated in Figure 3.2:

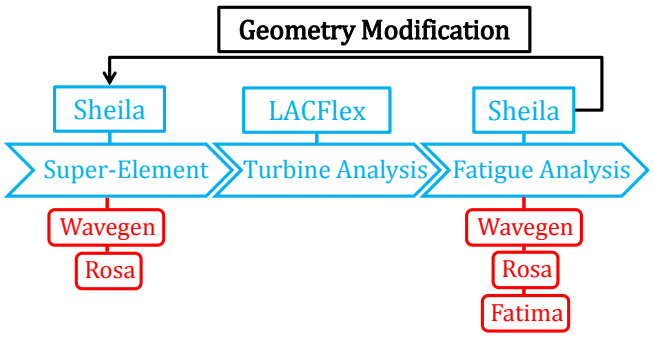

Figure 3.2: *Design work flow using the Rambøll analysis software.*

Starting from the left in Figure 3.2, *Sheila* reads all the input files and redirects the information to the modular based sub-programs for specific OWT foundation analysis and saves the data for post processing. The modular sub-programs can be activated or deactivated for specific computations. Activated sub-programs for this graduation project are:

- *Wavegen* creates the wave state for the structural analysis of the super-element and FLS computations. Irregular waves, generated by the spectrum are a summation of linear regular waves with different frequencies and amplitudes. The corresponding velocities and accelerations are stretched to the instantaneous water surface by Wheeler stretching [53]. Current is defined as a constant volume discharge using the surface velocity and is aligned with the waves.

- *Rosa* represents the finite element structural analysis program and is called in the super-element and fatigue analysis [4]. The hydrodynamic forces on the substructure are computed with the Morison equation, see sub-section. 2.2.2. The inertia parameter C_M in eq. 2.1 is implemented by the MacCamy&

Fuchs [33] correction, changing with the corresponding MP section diameter and incoming wave length. The drag coefficient C_D is depended on the Reynolds number and Keulegan-Carpenter number. Marine growth values from [6] are included in the sub-surface locations by implementing an increased diameter in the Morison equation, see expression 2.1.

- *Fatima* performs the fatigue damage computation as described in 3.1.1. All type of welds, such as circumferential and longitudinal can be implemented and verified. Knowing from Rambøll project experience, circumferential welds (CWs) are design driving elements for MP-based wind support structures. Therefore only these welds are enabled. CW governing fatigue damage is caused by the mainly horizontal loading leading to large stress cycles in vertical direction in the tubular elements. CW locations are allocated by *Sheila* depending on pre-defined maximum/minimum weight/length per element according to manufacturing possibilities and at locations with changes of the cross section geometry. Since the circumferential weld locations and segment lengths are varying in the GA, due to changing geometries, fixed circumferential weld locations over the MP height are implemented, see Table 3.2.

Table 3.2: *Circumferential weld* (CW) *locations* (z) *measured from mean sea level.*

CW [#]	z [m]	CW [#]	z [m]	CW [#]	z [m]	CW [#]	z [m]
01	+4.5	07	-9.0	13	-23.0	19	-33.0
02	+2.5	08	-11.5	14	-24.0	20	-35.5
03	+0.5	09	-14.0	15	-26.0	21	-38.0
04	-1.5	10	-16.5	16	-27.5	22	-40.5
05	-4.0	11	-19.0	17	-29.0	23	-43.0
06	-6.5	12	-21.5	18	-30.5	24	-45.5

Stress cycle counting is completed by rainflow counting and the used specification SN-curve is: D with cathodic protection from [8], see Table 3.3.

First design loop step of Figure 3.2 is the super-element generation performed by *Sheila*. There, the sub-structure with the hydrodynamic environment is simulated. Subsequently, the MP structure is condensed into a generated super-element including the hydrodynamic loads in transfer files. Next, the super-element is handed over to the Rambøll wind turbine analysis program *LACFlex*.

LACFlex is an aero-elastic wind turbine simulation program based on FLEX5 [54], originally developed for onshore wind turbines. The simulation program represents the wind turbine including blades, nacelle, rotor, drive train, tower and foundation [55]. The model include a full turbine dynamics simulation with reduced 28 degrees of freedom [55]. *LACFlex* simulates the LCs with a super-element at the tower bottom. Next, the forces at the interface are included in transfer files. The forces include time series of forces and moments at the interface. For further reading on the aero-elastic simulation software, the reader is referred to [54, 55].

The last step of the sequentially integrated design loop is the inclusion of the hydro- and aerodynamic forces in the finite element program *Sheila*. Afterwards, the fatigue damage analysis performed in *Fatima* at each CW for twelve radial positions (RPs) at the circumference of the MP, see Figure 3.3 and Table 3.2 for specifications. The RP are set to record the fatigue damage for wind-wave misalignments sufficiently.

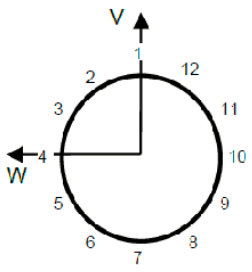

Figure 3.3: *Radial position* (RP) *numbers taken from* [4].

Table 3.3: SN-curve parameters D repeated from [8].

Parameter	Value	Unit
a_1	$5.808 \cdot 10^{11}$	[-]
m	3	[-]
t_{ref}	25	[mm]
k	0.20	[-]

Application of the design fatigue factor, presented in sub-section 2.2.4, is set to one. This does not reflect the state of the art, see Section 2.2.1, but for the purpose of this graduation project it is sufficient and is not biasing the results. Since the thesis goal is to identify the relation between optimized MP primary steel masses for different design lifetimes, the application of a constant parameter can be excluded.

To cover non-linearities all simulations are completed in the time domain.

3.2 Genetic Algorithm Implementation

The geometry modification from Figure 3.2 is now completed by the genetic algorithm (GA), see Figure 3.4. There the offshore wind turbine (OWT) analysis tools presented in section 3.1.3 are used to optimize a monopile (MP) based OWT with respect to the requirements presented in sub-section 2.2.3 with an emphasis on frequency and fatigue limit states (FLSs).

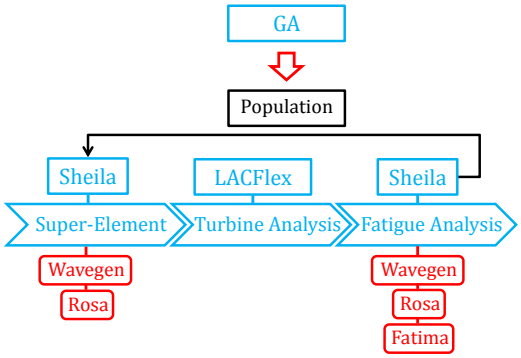

Figure 3.4: *General overview of the design loop inside the* GA *including analysis softwares.*

Firstly, main GA definitions from sub-section 2.3 are defined in sub-section 3.2.1, followed the penalty and exiting mechanism description in sub-section 3.2.2. GA tuning parameters are defined in sub-section 3.5.

The present GA optimization is containing partially continuous and discrete steps, resulting from available material delivery dimensions. Therefore, integer computation in the GA Matlab® function is selected. Scripts for MP geometry modification, analysis program steering and result evaluation are created.

3.2.1 Genetic Algorithm - Variables and Constraints

Optimized Variables

The optimization variable vector $\vec{x}$ of expression 2.8, is defined in expression 3.1. The vector $\vec{x}$ consists of parameters, that describe the MP primary steel structure geometry, i.e. cone angle α, section length L_3 and corresponding block wall thicknesses t_1 to t_3. The structure illustration is shown in Figure 3.1.

$$f(\vec{x}) = G \tag{3.1}$$

With the aim to reduce the MP weight G, the fitness function f evaluates the optimization variables $\vec{x}$ in each loop, see Figure 3.4. In Table 3.4 the constrained optimization variables with their minimum and maximum values are listed:

Table 3.4: *Constrained optimization variables.*

Variable	Min.	Max.	Unit
α	2.5	3.0	[deg]
L_3	30	50	[m]
$t_{1,2,3}$	55	113	[mm]

The diameter is defined within the computation resulting from block length two, the cone angle α and the pile top diameter.

Fitness Function

The design fitness evaluations are divided into three blocks, see Figure 3.1. Mass computations of block I and block III are equivalent due to a constant diameter, see expression 3.2:

$$G_{I,III} = \rho \frac{\pi}{4} \left[{D_o}^2 - (D_o - 2t_{1,3})^2 \right] L_{1,3} \tag{3.2}$$

The conical section, i.e. block II, the mass evaluation is computed by eq. 3.3:

$$G_{II} = \rho_{Steel} \frac{\pi}{3} \left[\left(\frac{{D_{o,top}}^2}{4} + \frac{D_{o,top} D_{o,tip}}{2} + \frac{{D_{o,tip}}^2}{4} \right) - \left(\frac{{D_{i,top}}^2}{4} + \frac{D_{i,top} D_{o,tip}}{2} + \frac{{D_{i,tip}}^2}{4} \right) \right] L_2 \tag{3.3}$$

$$D_{i,top} = D_{o,top} - 2t_2 \quad D_{i,tip} = D_{o,tip} - 2t_2$$

$D_{o,top}$	...	Outer cone top section diameter	[m]	$D_{o,tip}$	...	Outer cone tip section diameter	[m]
$D_{i,top}$	...	Inner cone top section diameter	[m]	$D_{i,tip}$	...	Inner cone tip section diameter	[m]
$L_{1,2,3}$	...	Block length	[m]	ρ_{Steel}	...	Steel density	[kg/m^3]

By summing the block masses G_I, G_{II} and G_{III} the overall total monopile mass G is obtained. The latter represents the fitness evaluation f of the design vector $\vec{x}$.

Constraint Function

The MP weight minimization without constraints would reduce the optimization variables to their minimum in the intervals given in Table 3.4. Subsequently, the structure would not meet the requirements for a safe operation during its lifetime. Therefore, the weight minimization is constrained by requirements presented in sub-section 2.2.1. Those requirements are re-formulated in mathematical definitions in Table 3.5:

Table 3.5: GA *design constraints.*

Variable	**Formulation**	**Origin**
c_b	D/t <120	Buckling [11, 45]
c_t	t_{n-1}/t_n <10%	Weld ability
c_{f1}	$f_1 > f_{low}$	Lower soft-stiff frequency
c_{f2}	$f_1 < f_{up}$	Upper soft-stiff Frequency
c_{FLS}	$D_{crit} < D_{Lim}$	Limiting Damage

c_b is the requirement for buckling prevention. c_t in Table 3.5 refers to the thickness change of two adjacent sections. The design frequency f_1 is the average value of the first two natural frequencies, since due to MP structure symmetry, the two bending modes are close together. f_{up} and f_{low} are the soft-stiff frequency boundaries. D_{crit} represents the critical fatigue damage of the current structure. Since the structure is as strong as its weakest link, only the maximum damage is handed over to the GA constraint function. D_{Lim} is the projected maximum fatigue damage during the design lifetime, i.e. 0.04 for a lifetime of 25 years without any design fatigue factor.

For each design the constraints are evaluated and subsequently create a basis for design comparison within a population.

3.2.2 Exiting Mechanism & Constraint Violations

Since the GA constraint evaluation is stepwise, see Figure 3.5, a conditional exiting mechanism is activated, when buckling and frequency constraints are not fulfilled. These designs will not be selected as a final design. This ensures that computational recourses are only allocated for feasible designs. Feasible designs for this graduation project are MP structures fulfilling all the constraints in Table 3.5.

In case the exiting mechanism is activated, an artificial fatigue constraint value is handed over to the GA. This constraint value is set to be a fixed value, which is violating the FLS constraint. If the exiting mechanism is not activated, the FLS computation is completed and the real fatigue constraint value is calculated, which is crucial for the evaluation of the design.

After the artificial or real constraint FLS, the weld ability constraint is evaluated. This constraint is not part of the exiting mechanism, since the importance of this manufacturing constraint is lower compared to the structural constraints.

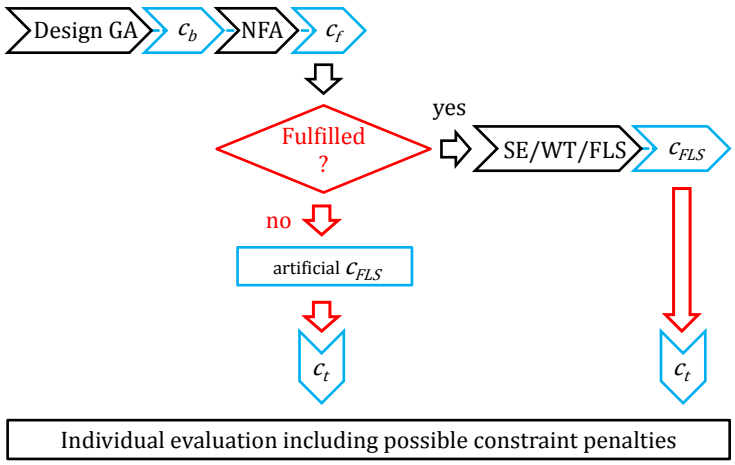

Figure 3.5: *Computation process inside the genetic algorithm including the exiting mechanisms.*

For each constraint violation a penalty is applied by the GA. The penalties are implemented in the Matlab® GA function as described in [50]. There, for constraint violating designs, the number of normalized constraint violations of the current designs is summed with the populations worst, but feasible fitness value [50, 56]. Thus, comparison of unfeasible designs is completed with their constraint function, while feasible designs are compared with their fitness function [56]. The severity of constraint violations also influences the design comparison and influences further selections [56]. For further reading on the penalty implementation in the GA, the reader is referred to [50, 56].

3.3 FLS Load Case Reduction - Methodology

In cluster computation a full fatigue limit state (FLS) load case table (LCT) computation varies from a maximum of approximately two hours to a minimum of 45 minutes, depending on the current cluster loading degree. This Section presents required load case (LC) reduction techniques with the aim of high accuracy. Assuming the computation time of each LC is equal, the maximum LC number is set to 120, i.e. approximately five minutes per individual or design evaluation. This implies a LC reduction from the original FLS LCT in Section 3.1.1 of approximately 90%. Without the time reduction the genetic algorithm (GA) optimization of offshore wind turbine (OWT) MP primary steel including the FLS would not be feasible.

The methodology of LC reduction techniques within this graduation project is based on a sensitivity analysis, containing a FLS analysis using the full LCT for a design set. This design set contains different MP geometries obtained by a prior GA run. The designs are fulfilling the frequency and weld ability listed in Table 3.5. Differences in geometry imply a variation of embedment depths, cone angles and thickness distributions. In Table 3.6 design set formative parameters, including their maximum, minimum, mean values $\overline{\mu}$ and standard deviations σ, are listed:

Table 3.6: *Covered geometry and frequency parameters of the design set, which is containing* 41 *designs.*

Physical Quantity	$\overline{\mu}$	σ	Min.	Max.	Unit
Frequency	0.21	$1.2{\cdot}10^{-2}$	0.19	0.23	[Hz]
Wall thicknesses	93.40	12.12	45.00	113.00	[mm]
Penetration depth	32.14	7.68	45.24	23.6	[m]

For each design, fatigue damage is evaluated at 24 circumferential welds (CWs) at twelve radial positions (RPs) using the full FLS LCT. The information about damage contribution per LC over the design set will create the basis for the estimation techniques presented in Section 3.3.1-3.3.4. For RP and CW specifications, see Figure 3.3 and Table 3.2.

Four techniques for LC reduction using fatigue damage estimation are described in the sub-Sections 3.3.1 - 3.3.4:

- Load Case Ranking
- Random load case set
- Factor approach
- Importance Sampling

The LC reduction with fatigue estimation using the techniques mentioned above is completed in gradually increasing complexity steps as listed in Table 3.7. Fatigue damage estimation techniques are tested, starting from a single position, i.e. one CW and one RP, to the full three dimensional MP structure, i.e. all 24 CWs and twelve RPs.

Table 3.7: *Prospected steps for damage estimation technique comparison for circumferential welds* (CWs) *for each radial position* (RP).

Step [#]	CW [#]	RP [#]
1	1	1
2	1	1-12
3	1-24	1
4	1-24	1-12

Technique comparison is completed by use of statistical values: mean value and standard deviation of fatigue damage. The nomenclature of the fatigue damage mean value and standard deviation is following the steps stated in Table 3.7 and is listed in Table 3.8:

Table 3.8: *Nomenclature of fatigue estimation mean value* $\overline{\mu}$ *and standard deviation* σ *of* LC *reduction techniques.*

Step [#]	$\overline{\mu}$ [-]	σ [-]
1	$\overline{\mu}_{est}$	σ_{est}
2	$\overline{\mu}_{est}^{RP}$	σ_{est}^{RP}
3	$\overline{\mu}_{est}^{CW}$	σ_{est}^{CW}
4	$\overline{\mu}_{est}^{CWRP}$	σ_{est}^{CWRP}

3.3.1 Load Case Ranking

The LC ranking approach includes the computation of LCs following different LC sortings and adding the corresponding design set fatigue damage mean value of un-computed LCs. In other words, the true fatigue damage values from a reduced set of LCs of a design are combined with the fatigue damage mean value and consequently result in the fatigue damage prediction of a particular RP or CW. Three expressions to estimate the fatigue damage of a particular point (CW, RP) on the MP are presented below, see eq. 3.4, 3.6 and 3.8. The LC sortings are obtained taking the design set fatigue damage LC contribution into account, e.g. computation of LCs, from which the fatigue damage outcome variates largely over the design set. Eq. 3.4 shows the first fatigue estimation D_{est} technique:

$$D_{est} = \sum_{i=1}^{N} D_i^{real} + \sum_{j=N+1}^{LC_{max}} \overline{\mu_j} \tag{3.4}$$

D_{est}	...	Fatigue damage estimation	[-]
D_i^{real}	...	Real LC damage of LC_i	[-]
N	...	Number of computed LCs	[#]
LC_{max}	...	Maximum number of LCs in LCT	[#]
$\overline{\mu_j}$	...	Mean value of un-computed LCs in the LCT of remaining designs in the design set	[-]

Inclusion of an increasing amount of LCs leads to a reduction of the total damage estimation variance, since for each computed LCs, the corresponding LC variance is reduced to zero. Possible improvement can be obtained by introduction of a global scaling factor $\overline{f}$, applied to the design set fatigue damage mean value $\overline{\mu}_j$ of the remaining LCs in eq. 3.4. The global scaling factor $\overline{f}$ is the mean value of factors f_i per LC. f_i is obtained by dividing the computed LC damage D_i^{real} with the corresponding LC mean value $\overline{\mu_i}$ of the design set, i.e. $f_i = D_i^{real}/\overline{\mu_i}$, see eq. 3.5. With increasing amount of computed LCs, the number of f_i is increasing proportionally.

$$\overline{f} = \overline{\sum_{i=1}^{N} \frac{D_i^{real}}{\overline{\mu_i}}} \tag{3.5}$$

$$D_{est} = \sum_{i=1}^{N} D_i^{real} + \overline{f} \sum_{j=N+1}^{LC_{max}} \overline{\mu_j} \tag{3.6}$$

Another approach of factorizing the remaining LC fatigue damage mean value $\overline{\mu_j}$ is by computing the median value $\tilde{f}$ of factors f_i, see eq. 3.7. $\tilde{f}$ is forming the new eq. 3.8.

$$\tilde{f} = \sum_{i=1}^{N} \frac{D_i^{real}}{\overline{\mu_i}} \tag{3.7}$$

$$D_{est} = D_i^{real} + \tilde{f} \sum_{j=N+1}^{LC_{max}} \overline{\mu_j} \tag{3.8}$$

3.3.2 Random Load Case Set

This approach is using eq. 3.6 and 3.8. In comparison to the LC ranking approach the LCs are selected randomly. For each design in the design set the computation is repeated in many seeds. In each seed one random LC is inserted in the eq. 3.6 and 3.8. The outcome of each seed results in a scaling factor f_i of the random LC. This factor scale the remaining LC fatigue damage mean value $\overline{\mu_j}$. The LC creating the smallest error to the true damage value is saved for each design. Assembling the single LC of each design forms the random LC set, i.e. LC_{rand}.

3.3.3 Factor Approach

This approach is used for step one and step three, see Table 3.7. The goal is to compute the damage with LC ranking in eq. 3.6 for one CW or RP and estimate the remaining CWs or RPs, using factors f_{CW} and f_{RP}. The factors are computed by use of the CW or RP fatigue damage mean values, i.e. $\overline{\mu}_{DMG}^{CW}$ $\overline{\mu}_{DMG}^{RP}$, and standard deviations, i.e. σ_{DMG}^{CW} and σ_{DMG}^{RP}, over the design set. This ensures that fatigue damage is only computed for one CW RP. The remaining fatigue damage of the eleven RPs or 23 CWs are obtained by multiplying the factors with the outcome of the fatigue damage estimation of eq. 3.6. In case of step two in Table 3.7, the factors f_{RP} are obtained by normalizing all radial positions $n = [1, 12]$ in the nominator by RP j in the denominator, see eq. 3.9. In case of step three in Table 3.7, f_{CW} is obtained similarly by normalizing all circumferential welds $n = [1, 24]$ by CW j, see eq. 3.10.

$$f_{RP} = \frac{\overline{\mu}_{DMG_n}^{RP} + 3 \cdot \sigma_{DMG_n}^{RP}}{\overline{\mu}_{DMG_j}^{RP} + 3 \cdot \sigma_{DMG_j}^{RP}} \tag{3.9}$$

$$f_{CW} = \frac{\overline{\mu}_{DMG_n}^{CW} + 3 \cdot \sigma_{DMG_n}^{CW}}{\overline{\mu}_{DMG_j}^{CW} + 3 \cdot \sigma_{DMG_j}^{CW}} \tag{3.10}$$

3.3.4 Importance Sampling

The integral over a volume V in eq. 3.11, taken from [57], can be either computed random sampling of x_i from V with the probability distribution $p(x_i)$ or with samples y_i from a different non-uniform probability distribution $g(y_i)$ [57, 58].

$$\int f dV = \int \frac{f}{g} g dV \tag{3.11}$$

f/g represents the weighted sample. Knowing from Monte Carlo (MC) simulation, the integral of a function I_{MC} , i.e. left hand side of eq. 3.11, can be expressed as a sum of N randomly selected samples x_i, see eq. 3.12 taken from [57]:

$$I_{MC} \approx \frac{\sum_{i=1}^{N} f(x_i)}{N} \pm \sqrt{\frac{\frac{\sum_{i=1}^{N} f(x_i)^2}{N} - \left(\frac{\sum_{i=1}^{N} f(x_i)}{N}\right)^2}{N}} \tag{3.12}$$

Expression 3.12 represents the mean value $\overline{\mu}_{MC}$ plus/minus the standard error σ_{MC} [57], see eq. 3.13:

$$I_{MC} \approx \overline{\mu}_{MC} \pm \sigma_{MC} \tag{3.13}$$

If $N \to \infty$, the integral is estimated perfectly, the standard error goes to zero $\sigma_{MC} \to 0$ and the Importance Sampling (IS) integral estimate I_{IS} converges to the actual value [58]. Applying this methodology for the right hand side of eq. 3.11 leads to eq. 3.14 taken from [57]:

$$I_{IS} \approx \frac{\sum_{i=1}^{N} \frac{f(y_i)}{g(y_i)}}{N} \pm \sqrt{\frac{\frac{\sum_{i=1}^{N} \left(\frac{f(y_i)}{g(y_i)}\right)^2}{N} - \left(\frac{\sum_{i=1}^{N} \frac{f(y_i)}{g(y_i)}}{N}\right)^2}{N}} \tag{3.14}$$

The IS integral estimate I_{IS} from eq. 3.14 reduces to eq. 3.12 in case the probability densities p and g collide, i.e. $p/g = 1$ [57]. The standard error defines how well a sample mean is estimating the actual mean of the original distribution [57] and is also known to decrease with increasing amount of samples N, as shown in eq. 3.15:

$$\sigma_M = \frac{\sigma}{\sqrt{N}} \tag{3.15}$$

σ_M is the standard error of the mean and σ the standard deviation of the sample distribution. The fatigue damage estimation in eq. 3.16 is representing the sample mean value estimation in eq. 3.14, using a different sample distribution g:

$$D_{est} = \frac{\sum_{i=1}^{N} \frac{D_i^{real}}{g_i}}{N} \tag{3.16}$$

D_{est}	...	Fatigue damage estimation	[-]
D_i^{real}	...	Real LC fatigue damage of LC i	[-]
g_i	...	IS weight	[-]
N	...	Number of included LCs	[#]

The non-normally distributed cumulative probability density g is formed by the fatigue damage mean value over the design set, ranging from zero to one. The number of circumferential welds and radial positions taken into account for the cumulative probability curve depends on the current accuracy step, see Table 3.7.

IS includes random LC selection. Therefore, random numbers between zero and one are selected, pointing to one LC each. LCs with large contribution to the total fatigue damage have a higher chance to be selected. The randomly selected numbers are also the corresponding LC weighting factors g_i. By the weighting the LC damage outcome D_i^{real} by g_i, fast convergence is expected, see eq. 3.15, e.g. by inclusion of four LCs, the standard error towards true damage mean reduces by approximately 50%.

3.4 Genetic Algorithm - Load Case Reduction Implementation

In Section 3.3 different techniques for fatigue damage estimation were presented and will be compared in Section 4.1 regarding the criteria: accuracy and amount of LCs. The best resulting technique is implemented in the GA fatigue limit state constraint evaluation, see Table 3.5. First, two possible methodologies are presented in sub-Section 3.4.1. Next, in sub-Section 3.4.2 the critical MP fatigue damage for the GA FLS constraint evaluation is explained.

3.4.1 Genetic Algorithm Load Case Reduction Implementation Methods

3.4.1.1 Refining Accuracy

Since in the early generations of the GA the search space is quite coarse, it is assumed that the required accuracy is lower compared to the later generations, i.e. the search space refines towards later generations. To save computation time, less LCs with a lower accuracy are implemented in early generations. With increasing generation number the LC number is augmented. Towards later generations the GA constraint will be close to the constrained limits. Therefore, higher accuracy is essential if a design is passing or failing the constraint criteria.

Simplest approach to tackle the refinement, is by implementing the LC sets in stages k. Here, four stages are implemented. 30 LCs are set as minimum since file-loading times by the programs presented in sub-section 3.1.3 is the same for the first 30 LCs. LC numbers in the following stages $k = [2, 4]$ are set to 50, 90 and 120. Subsequently, this approach follows a variable constraint evaluation during the GA optimization. In Figure 3.6 the damage refinement stages, including generation numbers, are illustrated.

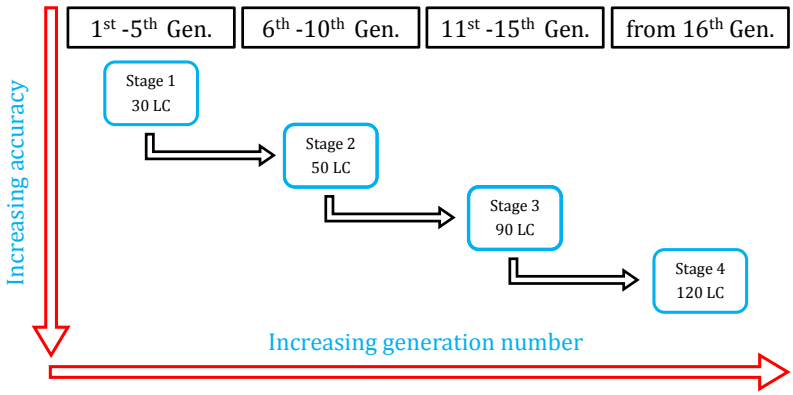

Figure 3.6: *Implemented* LC *reduction using Importance Sampling in the genetic algorithm* MP *optimization.*

3.4.1.2 Constant load case number

This approach is following a constant constraint evaluation during the whole genetic algorithm optimization. For this, the stage $k = 4$ of the LC refinement shown in Figure 3.6 is used.

3.4.2 Critical damage for genetic algorithm constraint function

The actual constraint evaluation inside the genetic algorithm is completed with one critical fatigue damage value. LCs of the actual stage k are computed, see Figure 3.6, and emphasized by the corresponding damage estimation technique mean value $\overline{\mu}_{ijk}^{CWRP}$ and standard deviation σ_{ijk}^{CWRP}, with i=[1,24] and j=[1,12]. This implies that for each stage k one $\overline{\mu}_{ijk}^{CWRP}$ and also one σ_{ijk}^{CWRP} [24x12] matrix is created.

Fatigue damage in a refinement stage k is combined with the obtained σ_{ijk} around the mean value $\overline{\mu}_{ijk}$, see eq. 3.17 with a multiplicand n. There, the [24x12] matrix $\mathbf{D}_k$ represents the fatigue damage estimate of the three dimensional MP structure including statistical factors and the [24x12] matrix $\mathbf{I}_k$ the un-factorized fatigue damage of the MP in stage k for each CW and RP.

$$\mathbf{D}_k = \mathbf{I}_k \cdot (\overline{\mu}_{ijk}^{CWRP} + n \cdot \sigma_{ijk}^{CWRP}) \tag{3.17}$$

From $\mathbf{D}_k$ the scalar critical fatigue damage D_{crit}, i.e. the largest fatigue damage value, is selected as the genetic algorithm constraint value, since the structure is as strong as its weakest link, see eq. 3.18:

$$D_{crit} = \max(\mathbf{D}_k) \tag{3.18}$$

3.5 Genetic Algorithm - Settings

GA implementation in the design process is completed by use of the GA Matlab® function. Since mixed integer computation for discrete steps of the wall thickness is applied, several genetic algorithm options are restricted. Relevant restrictions are repeated from [50]:

- No linear constraints. These can be circumvented by two non-linear constraints.
- No custom cross-over, mutation and creation functions.
- Tournament selection is the fixed parent selection technique.
- No custom penalty factors.

In Table 3.9 several set GA key parameters are defined:

Table 3.9: GA *tuning parameters.*

Variable	Value	Unit
G_{max}	45	[-]
P	15	[-]
f_{tol}	10^{-3}	[ton]
G_{stall}	20	[#]
E_{count}	1	[-]
C_{over}	0.8	[-]

G_{max} is the predefined maximum GA generations after which the algorithm stops the global optimum search. Since the prospected maximum evaluation time per individual or design is five minutes, the algorithm would stop after 2.3 days depending on the cluster loading.

Population size P is influencing the convergence of the algorithm, since with a larger pool of individuals the optimum is more likely to be reached. On the other hand, a larger population implies more individual evaluations and subsequently higher computation time per generation. In a prior run the GA is tested with populations containing 15 and 20 individuals. Both optimizations led to the same converged results. Therefore, the smaller population size is selected.

f_{tol} is representing the function tolerance. In case of a 1000 ton MP, an accuracy of one ton is assumed to be an appropriate resolution for a discrete optimization problem. This limit is important for discrete optimizations, since the algorithm might jump between two possible wall thicknesses and not converge in case the tolerance benchmark is set too low.

Maximum stall generations G_{stall} are set to terminate the GA in case the best fitness value is not improving over set generations [50] in the range of f_{tol}.

E_{count} is defining the number of best designs that are copied from one generation to another without modification by cross-over and mutation. Regarding the small population size P the recommended elite count according to [50] is one.

The cross-over fraction C_{over} is the ratio of the cross-overs and mutation between designs within one generation. In the Matlab® GA function a crossover ratio of 0.8 is set as default [50] and is also used for this optimization. This ensures that a population is formed by previous generations, but also to keep the search space wide. The mutation is Gaussian distributed [50] and is performed by random number selection.

3.6 Model Assumptions, Uncertainties and Limitations

Assumptions for different parts in the model are simplifications and lead to model limitations. Those limitations combined with model, statistical and data uncertainties form the whole limitation of the computation model. Regarding the monopile (MP) structure optimization for different fatigue life times, the assumptions and uncertainties of the current model are sorted by themes: environment, structural and wind turbine analysis, and genetic algorithm (GA).

3.6.1 Environment Modeling

Assumptions

- Waves and current are aligned.
- Environment is represented by the eight seeds per wind speed in the discretization proposed in [5] and is considered to be sufficient to describe the fatigue loading on the OWT.
- Marine growth is implemented according to [59], depending on the water depth for the given site location.
- For this location no occurring ice loads are considered.
- Availability percentage of the wind turbine is assumed. In case the true availability of the OWT is higher than expected the structural system experiences more damping during its lifetime. Subsequently, the structure oscillations would be expected to be lower. Hence, a lower availability is leading to higher oscillations and to possible under conservatism in the design.
- The yaw error is set as a fixed $\pm$ value to the true wind direction in DLC 1.2. The true value of misalignment may be obtained by measurements in operation.

Uncertainties

- Data is obtained from measurements and is subsequently used for the load evaluation, that a structure is facing during its lifetime. For extended design lifetime, uncertainties of the environment prediction are rising.
- Lumping of wind-wave misalignments to four directions, i.e. 0, 30, 60, and 90 degrees.
- Resolution of two meters per second is assumed to be sufficient according to [59]. This resolution assumption should be evaluated on real OWT by measurements.
- The equal un- and loading path is not fully representing the dynamic soil loading behavior, i.e. hysteresis [55, 60]. Therefore, no accurate beneficial soil damping can be applied. Additionally, the p-y curve inputs of a soil layer are described by a limited amount of parameters, i.e. soil density and a soil specific parameter of the soil layer (friction angle for sand and undrained shear strength for clay).
- Uncertainty of API based methods are rising, because the industry is moving towards larger foundations, for which the p-y curves were not calibrated [61]. These curves, obtained from long flexible small diameter pile experiments, are used for relatively short MPs with a large diameter [60, 62].
- Soil is heterogeneous and may not be in horizontal layers as modeled.
- Soil conditions are not evaluated for each OWT location. The OWTs within a wind farm are clustered with the assumption of equal soil conditions within a cluster.

3.6.2 Structural and Wind Turbine Analysis

Assumptions

- The first two bending mode natural frequencies are taken into account for the placement in the soft-stiff region. Locations of higher frequencies are not verified.
- There is no occurring soil erosion due to applied scour protection.
- LCs with probabilities lower than 10^{-7} have negligible contribution to fatigue damage.
- Circumferential welds are considered to be the governing welds for fatigue design.

- Structural, soil and hydrodynamic damping are left unchanged from the Rambøll reference project. This value results from project experience. Possible reduction of fatigue damage is shown in [63], in which damping ratios between one and five percent are applied for fatigue prediction. Actual drag damping can not be implemented since the MP is assumed to be a rigid structure in the Morison equation [32, 55].
- MP, TP and tower modeling is taken from a Rambøll reference project. The model is a linear finite element model with Timoshenko beam elements. This beam theory takes, in contrast to the Bernoulli beam theory, shear deformation of sections into account.
- The MP sub-structure is considered as Craig-Bampton super-element in the aeroelastic analysis [64].
- Wheeler stretching is applied for the wave particle acceleration and velocities at the free surface elevation [53].

Uncertainties

- Hydrodynamic damping values are inserted from Rambøll project experience, but may deviate from real behavior.
- Non-linear soil behaviour is linerarized in the super-element approach.
- Cut-in and cut-out wind speeds are considered as exact as given from the wind turbine manufacturer. This is important for the border between the operational and non-operational LCs in terms of aerodynamic damping.
- Rainflow counting is considered the most accurate counting technique, but the influence of sequence effects is not taken into account [43].
- In reality the applied material is not fully homogeneous with the equal parameters over the whole section or thickness. Especially for FLS computation, in which characteristic loads are applied, this adds additional uncertainty in the true lifetime of the structure.
- Breaking down the complex fatigue phenomenon to a single parameter by the Miner Rule is leading to uncertainties in the lifetime prediction [43].
- Cycles below the fatigue limit are considered non-damaging, according to [43]. Using the Miner rule, the fatigue damage caused by previous cycles are disregarded [43]. This introduces an error, since the damage of an already degraded material should be higher compared to an undamaged one.
- The weld classification does not imply that the structural fatigue resistance of the whole assembly is the same as for single specimens in experiments.
- The time depended phenomenon corrosion plays an important role for a structure in the marine environment, especially in the air-water transition zone, since corrosion is a process of material degradation and influences the fatigue lifetime of a structure [43]. The influence of corrosion on fatigue is large, due to the fatigue limit reduction and large crack grow rates depending on the wave shape [43]. Additionally, the SN curves for free-corrosion are expected being 1/3 of the in air SN-curve [65].

3.6.3 Genetic Algorithm

Uncertainties

- There is no certainty that the global optimum is found. This strongly depends on the meters, see section 3.5.
- Optimal number of wall thicknesses, that should be optimized, need to be defined by several GA runs. A high number of wall thicknesses may not lead directly to smaller costs, since the manufacturing expenses are higher, if many sections with different wall thicknesses need to be assembled. Additionally the GA may take longer to converge.
- Block length one and two are kept unchanged. It is unclear if the global optimum may be found by including these two block lengths into the optimization.
- High sensitivity on inputs, such as function tolerance, cross-over fraction and mutation rate and number of individuals in a population influence the convergence behavior of the algorithm. Changing the inputs have different impact on the outcome of the algorithm.

- Corresponding fatigue life accuracy of converged genetic algorithm design, i.e. the global optimum design, depends on the current load estimation accuracy step and fatigue damage estimation technique, see Figure 3.6. In other words the estimation of the fatigue damage and the corresponding lifetime of the structure is highest, when the algorithm converges in the last stage, i.e. stage four.
- In design optimization it is very difficult to design a structure for an exact lifetime. Small changes in geometry influences the whole dynamics of the structure and may lead to a different governing detail on the structure.
- Possible errors are introduced with the fatigue damage estimation model. The critical fatigue damage result handed over to the GA constraint evaluation is on the conservative side. Difficulties will arise to acquire an exact projected life time.

4 | Results and Discussion

This chapter presents the results of the elaborated model in chapter 3. Section 4.1 discusses the results of the load case (LC) reduction techniques and their comparison. Section 4.2 presents the evaluation of the LC reduction implementation within the genetic algorithm (GA). In Section 4.3, the comparison of converged GA results for different lifetimes with a full fatigue limit state (FLS) load case table (LCT) analysis including the monopile (MP) mass versus lifetime graph is presented.

4.1 FLS Load Case Reduction - Results

Within this sub-section different results of LC reduction techniques are presented. Following the accuracy steps from Table 3.7, these techniques are compared. First, one dimensional LC reduction, including the fatigue damage estimation is presented in sub-section 4.1.1. Next, results of the two dimensional LC reduction, including fatigue damage estimation, are shown in sub-section 4.1.2 and 4.1.3 and finally, three dimensional, in sub-section 4.1.4. The main challenge is to find a robust and exact method, that is able to cover the directionality dependence of the MP fatigue damage.

4.1.1 Step 1: Damage Estimation of one circumferential weld position

The first step from Table 3.7 is the FLS LC reduction, including fatigue damage estimation of the circumferential weld one (CW1) at radial position one (RP1), see Table 3.2 and Figure 3.3. Within the following sub-sections three different LC reduction approaches are evaluated and compared with each other:

- Load case ranking
- Random load case set
- Importance Sampling (IS)

The three approaches are tested and compared with each other at the end of this sub-section. The fatigue damage estimation D_{est} of each design is normalized by the true fatigue damage value D_{fin}^{real} of a design location (CW) and position (RP) obtained from a full FLS LCT analysis, resulting in $||D_{est}||$.

4.1.1.1 Load case ranking - Results

The fatigue damage mean values $\overline{\mu}_{DMG}$ and standard deviations σ_{DMG} per LC over the design set at CW1 RP1 are illustrated in Figure 4.1. There, the contribution of each LC to the total fatigue damage can be observed. The boarder between DLC 1.2 and 6.4 [5] is marked by the dashed red line. For this OWT site, idling LCs contribute 53.7% and production LCs 46.3% in average to the design set mean damage $\overline{\mu}_{DMG}$ for CW1 RP1.

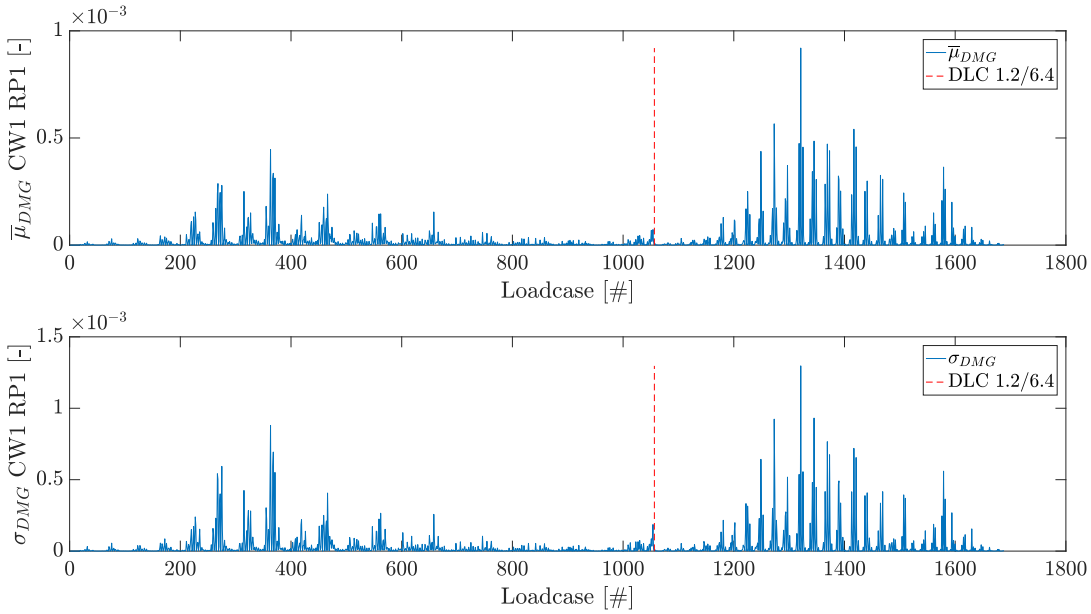

Figure 4.1: *Unsorted σ_{DMG} and $\overline{\mu}_{DMG}$ per* FLS LC .

In Figure 4.2 the LCs are sorted in descending σ_{DMG} order from highest to lowest, LC_{HtL} respectively. A similar trend is observed in terms of the mean value by using the LC_{HtL} sorting. This can be seen by comparing the upper and lower illustration in figure 4.2.

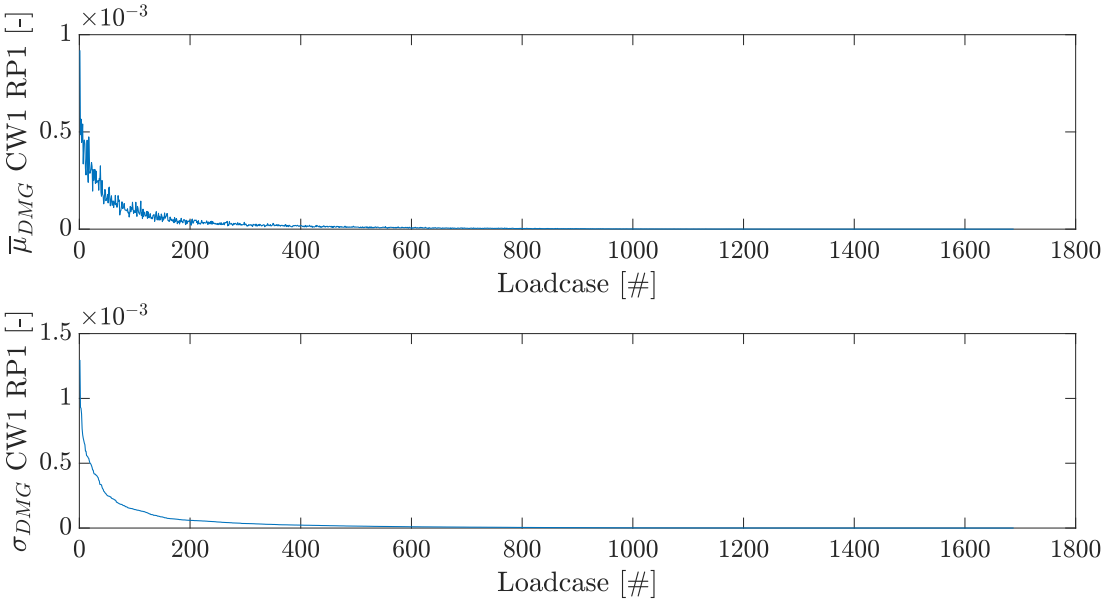

Figure 4.2: *Fatigue damage standard deviation σ_{DMG} and mean value $\overline{\mu}_{DMG}$ with LC_{HtL} sorting.*

Subsequently, fatigue damage estimation eq. 3.4 is conducted for fatigue damage estimations with LC sorting LC_{HtL}. Using eq. 3.4 for each design in the design set, the normalized fatigue damage estimate $||D_{est}||$ results in Figure 4.3. Additionally, the designs best/worst $||D_{est}||$ are compared. The required LCs to reach an error equal to 1% are: 650 and 1315 respectively. Due to large differences of the designs in terms of geometry and frequency, $||D_{est}||$ are largely over-/underestimated, since D_{fin}^{real} values are close or far away from the overall fatigue damage mean of the remaining 40 designs. This implies that the geometry and frequency are statistical outliers within the design set.

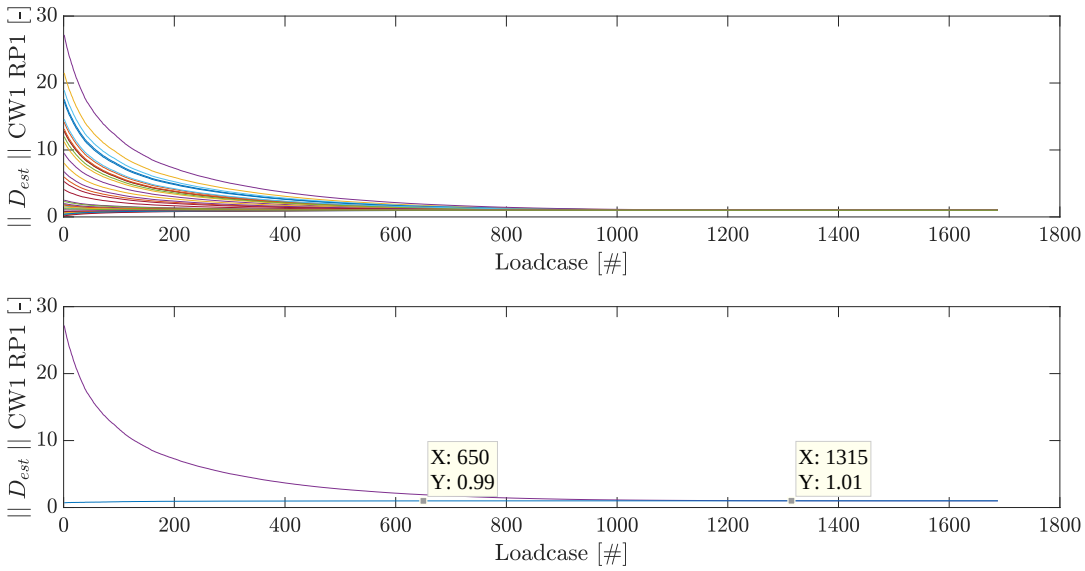

Figure 4.3: *Normalized fatigue damage estimates of all designs in the design set (upper figure) and best/worst estimates of the design set (lower figure)* CW1 RP1 *with sorting* LC_{HtL} *and estimation expression 3.4.*

In Table 4.1 the corresponding fatigue damage estimation mean values $\overline{\mu}_{est}$ and standard deviations σ_{est} over the design set at different amounts of computed LCs are listed.

Table 4.1: *Estimation mean values* $\overline{\mu}_{est}$ *and standard deviations* σ_{est} *at different amounts of computed* LCs *using* LC_{HtL} *sorting and eq. 3.4.*

LC [#]	$\overline{\mu}_{est}$ [-]	σ_{est} [-]
50	4.12	4.19
100	3.19	2.95
200	2.27	1.72
400	1.54	0.88
800	1.09	0.19
1600	1.00	$2.9{\cdot}10^{-5}$

In Figure 4.4 the updated damage estimation eq. 3.6 is leading to a clear fatigue damage estimation improvement using the LC ranking LC_{HtL}:

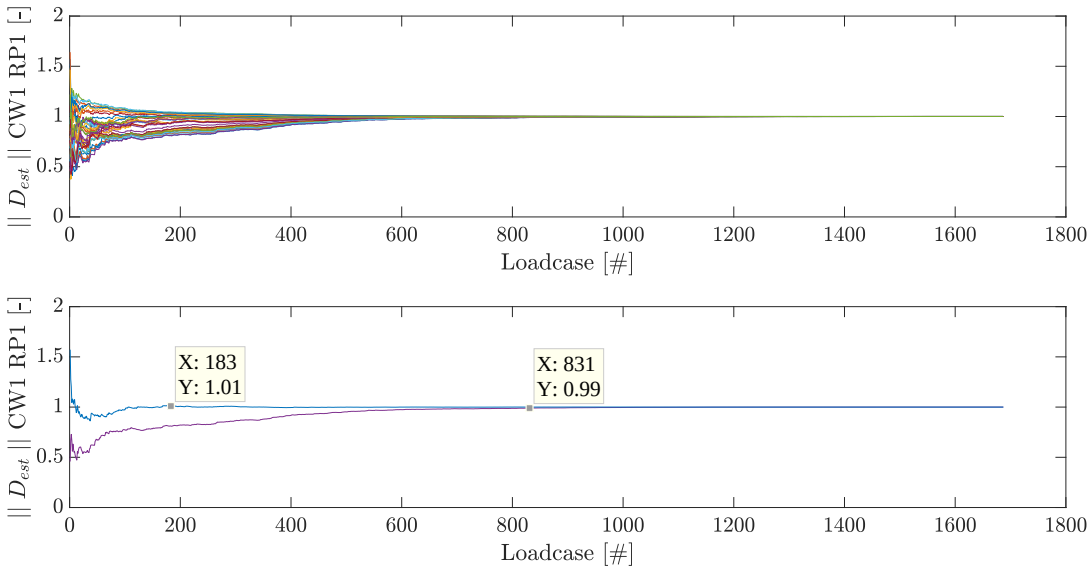

Figure 4.4: *Normalized fatigue damage estimates of all designs in the design set (upper Figure) and the best/worst estimates of the design set (lower Figure)* CW1 RP1 *with sorting* LC_{HtL} *using eq.* 3.6.

Again, as in the lower illustration in Figure 4.3, the comparison of best/worst normalized fatigue damage estimate $||D_{est}||$ within the design set are shown in Figure 4.4. There, the required LCs to reach an accuracy of 1% are reduced by 28% and 29% with respect to the total LC amount. In the uppermost sub-Figure 4.5, the scaled overall mean value $\overline{\mu}_{DMG}^{corr}$ is plotted next to the unscaled $\overline{\mu}_{DMG}$. Underneath the latter Figure, the factor f_i of eq. 3.5 is illustrated per LC. D^{real} in the bottom sub-Figure is representing damage value evolution in case all LCs are computed following the LCT numbering. The latter converges towards D_{fin}^{real} at approximately 800 LCs. In comparison $||D_{est}||$ is showing a fast convergence for an exemplary design.

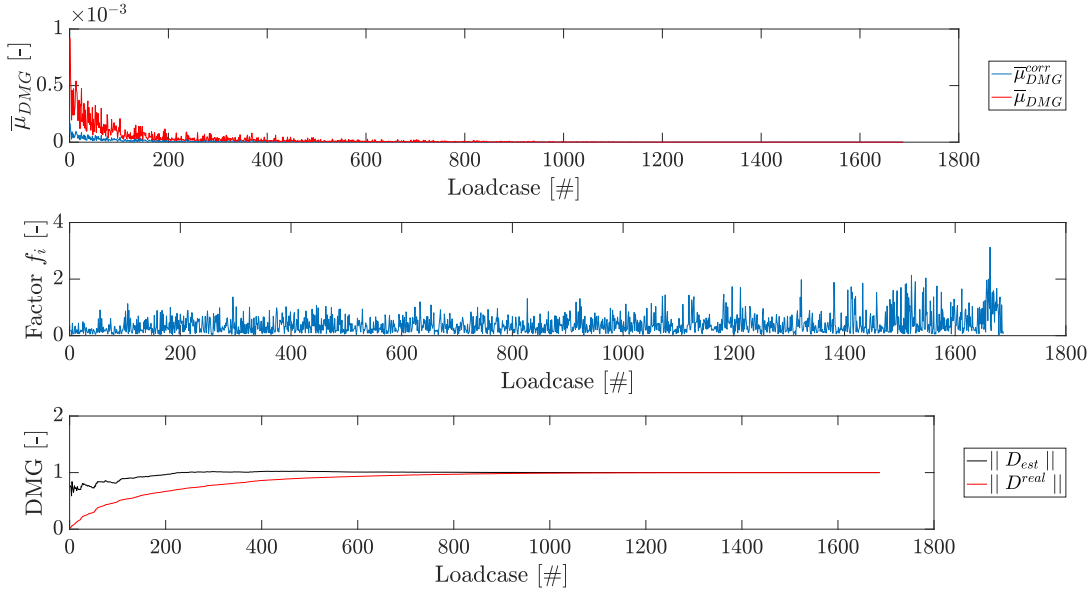

Figure 4.5: *Scaled overall mean value* $\overline{\mu}_{DMG}^{corr}$ *of an exemplary design by use of a global factor* $\overline{f}$ *per* LC*, depending on the number of simulated* LCs.

Resulting $\overline{\mu}_{est}$ and σ_{est} obtained with eq. 3.6 are tabulated in Table 4.2 and show a clear improvement in comparison to Table 4.1. Firstly, $\overline{\mu}_{est}$ reaches D_{fin}^{real} with less included LCs. Secondly, significant reduction of σ_{est} per LC stage is observed, i.e. for 50 LCs with a factor of approximately 36.

Table 4.2: *Fatigue damage estimation mean value $\overline{\mu}_{est}$ and standard deviation σ_{est} at different amounts of computed* LC *for the global factor approach using* LC_{HtL} *sorting and eq. 3.6.*

LC [#]	$\overline{\mu}_{est}$ [-]	σ_{est} [-]
50	0.87	0.12
100	0.91	0.10
200	0.94	0.07
400	0.97	0.03
800	1.00	$4.7 \cdot 10^{-3}$
1600	1.00	$2.0 \cdot 10^{-6}$

Further, the highest to lowest standard deviation sorting LC_{HtL} is probability weighted by the probability of occurrence and by the relative contribution of $\overline{\mu}_{DMG}$ to the overall fatigue damage mean sum: $\overline{\mu}_{DMG}/\sum\overline{\mu}_{DMG}$, leading to a new sorting LC^{Pw}_{HtL}, see Figure 4.6. Some LCs with higher contribution to the mean value are now shifted and computed earlier.

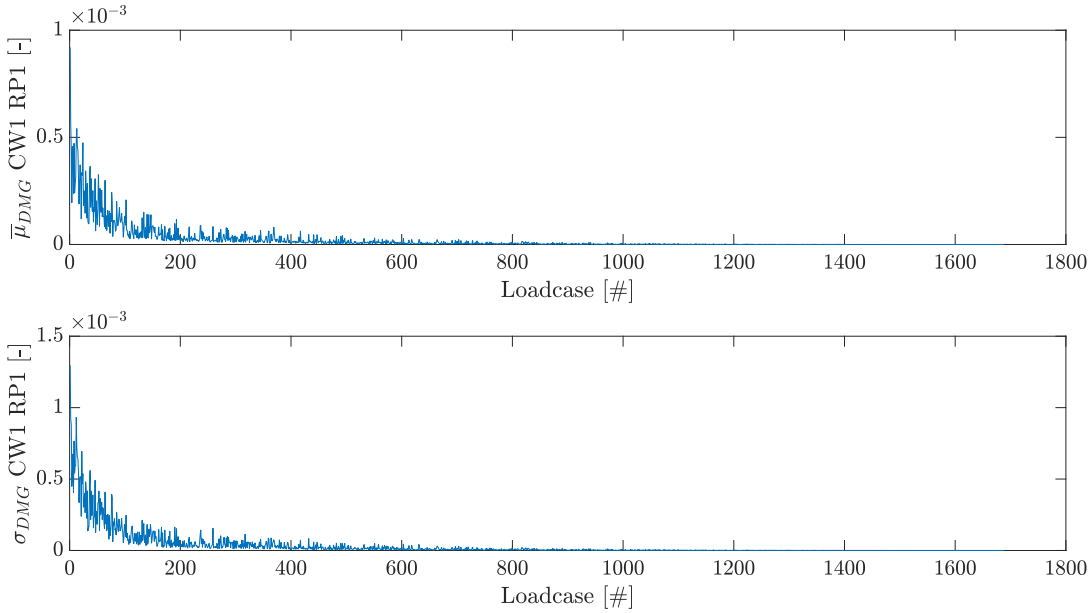

Figure 4.6: *σ_{DMG} and $\overline{\mu}_{DMG}$ of the LCs with LC^{Pw}_{HtL} sorting.*

Normalized fatigue damage estimates $||D_{est}||$ of all designs using eq. 3.6 with LC ranking of Figure 4.6 are illustrated in Figure 4.7. Corresponding $\overline{\mu}_{est}$ and σ_{est} values are tabulated in Table 4.3.

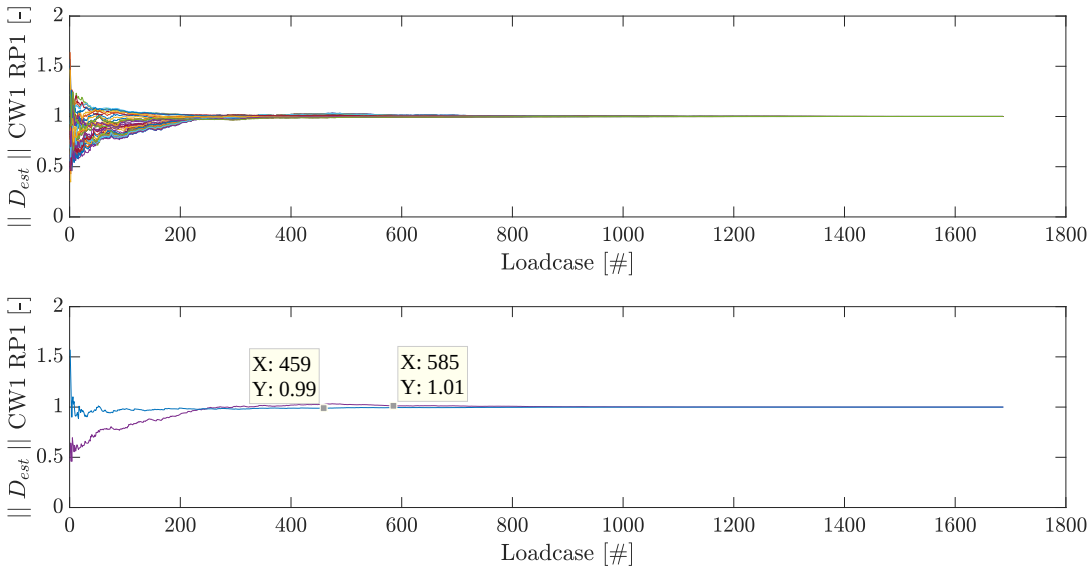

Figure 4.7: *$||D_{est}||$ of all designs in the design set (upper Figure) and the best/worst estimates of the design set (lower Figure), including the with LC^{Pw}_{HtL} sorting and estimation eq. 3.6.*

Table 4.3: *$\overline{\mu}_{est}$ and σ_{est} at different amounts of computed LC for the global average factor $\overline{f}$ approach with a LC^{Pw}_{HtL} sorting using eq. 3.6.*

LC [#]	$\overline{\mu}_{est}$ [-]	σ_{est} [-]
50	0.88	0.12
100	0.91	0.09
200	0.97	0.03
400	1.01	0.01
800	1.00	$3.8 \cdot 10^{-3}$
1600	1.00	$5.4 \cdot 10^{-7}$

In comparison to the LC_{HtL} sorting, convergence has not improved significantly, see Table 4.2 and 4.3. Improvements can only be observed for σ_{est} from LC 800 on, but also a small deterioration for stages 50, 100, 200 and 400 LCs. $\overline{\mu}_{est}$ remained approximately the same.

Inferring from the three presented methods, the influence of the global factor $\overline{f}$, defined in eq. 3.5, is high. In case of computing a LC, that is resulting in a damage value D_i^{real} with a large deviation to the LC corresponding mean value, the scaling is completed using a too high/low factor. This results in a late convergence to the true value D_{fin}^{real} in early stages. Estimations with LC sorting LC_{HtL} by use of the median $\tilde{f}$ for the obtained factors f_i in estimation eq. 3.8 are illustrated in Figure 4.8 and Table 4.4. $||D_{est}||$ deteriorates in all LC stages in terms of mean and standard deviation.

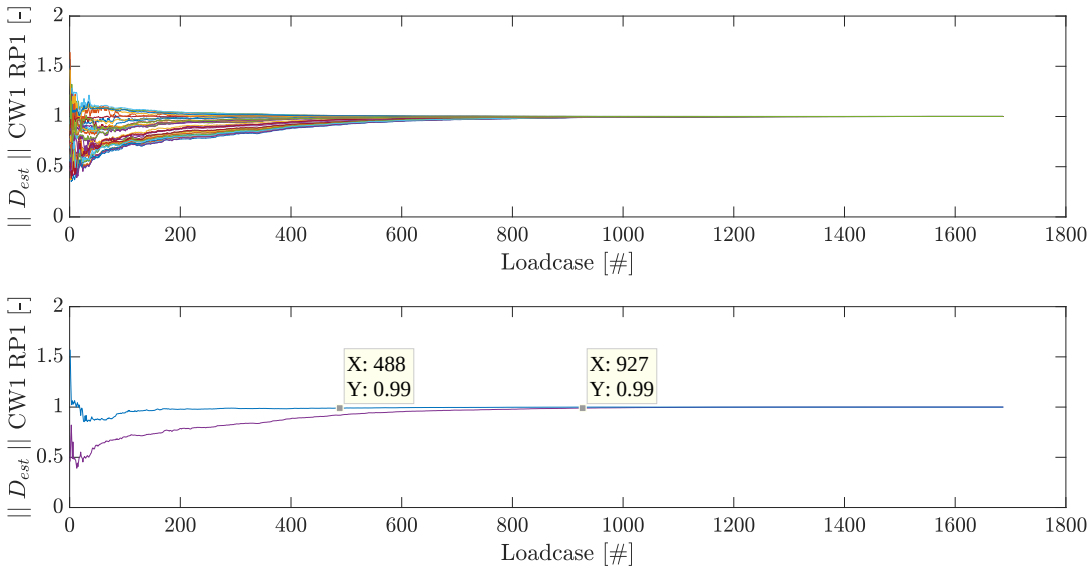

Figure 4.8: *$||D_{est}||$ of all designs in the design set (upper Figure) and the best/worst estimates of the design set (lower Figure), including the damage standard deviation ranking of* CW1 RP1 *with the updated estimation expression 3.8 and* LC_{HtL} *sorting.*

Table 4.4: *$\overline{\mu}_{est}$ and σ_{est} at different amounts of computed* LC *for the global median factor $\tilde{f}$ approach with a* LC_{HtL} *sorting using eq.* 3.8.

LC [#]	$\overline{\mu}_{est}$ [-]	σ_{est} [-]
50	0.80	0.17
100	0.85	0.12
200	0.91	0.08
400	0.95	0.04
800	0.99	$7.3 \cdot 10^{-3}$
1600	1.00	$2.4 \cdot 10^{-6}$

The most efficient and robust technique within the LC ranking approach leading to faster convergence towards the true damage value D_{fin}^{real} is by taking the average of the scaling factors f_i per LC and apply it as a global factor $\overline{f}$ to $\overline{\mu}_j$, i.e. eq. 3.6. For further fatigue damage estimations only eq. 3.6 with LC_{HtL} sorting will be considered.

4.1.1.2 Random load case set - Results

Fatigue damage estimations $||D_{est}||$ using eq. 3.6 per design is completed multiple times by selecting one randomly selected LC. The remaining LCs are included by the factorized fatigue damage mean value sum of the remaining designs and LCs in eq. 3.6 using the factor f_i from the design LC outcome. In Figure 4.9 $||D_{est}||$ scatter with high/low deviation to D_{fin}^{real} is illustrated. The conclusion is that some LCs result in a factor f_i, that is scaling the mean value of the remaining 1687 LCs in such a way, leading to an estimation close to D_{fin}^{real} using only one LC per design.

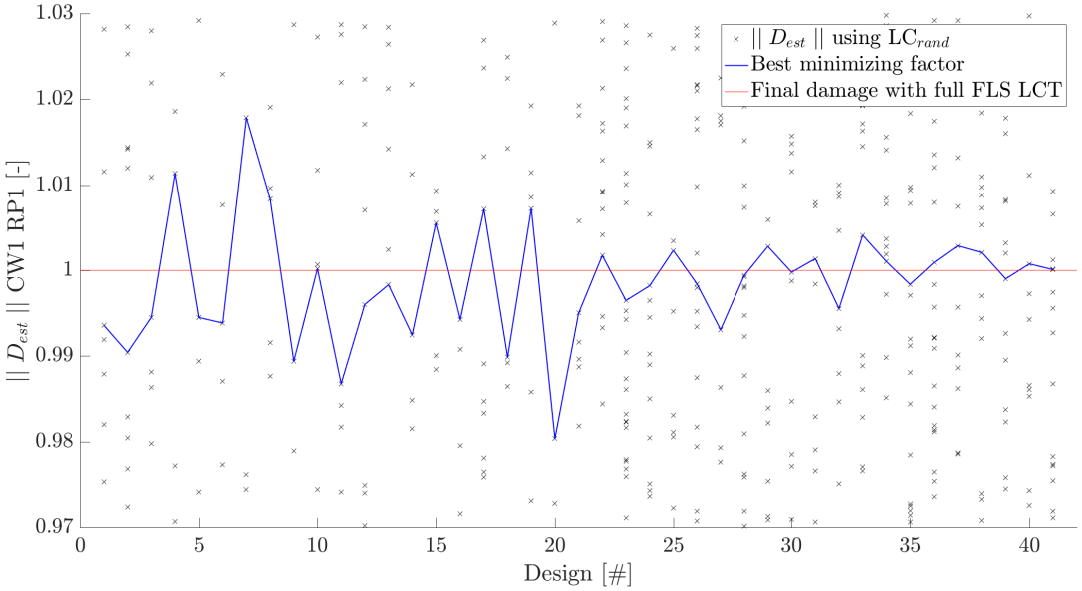

Figure 4.9: *Damage estimation per design including one* LC *using 500 seeds.*

The random LC set LC$_{rand}$ is created by taking the best resulting scaling factor f_i from a LC per design. This leads to a random LC set LC$_{rand}$ of 41 designs by assembling the best scaling factor f_i per design. Due to similar designs for the same locations the LC numbers may repeat themselves within the LC set LC$_{rand}$. Only unique LC numbers are used in LC$_{rand}$. This implies that the number of LCs within LC$_{rand}$ may be smaller than the design set of 41 designs, e.g. for the present case the LC set LC$_{rand}$ consists of 41 load cases. Locations of these LCs in the FLS LCT are illustrated in Figure 4.10. The resulting normalized fatigue damage estimate $||D_{est}||$ per design, using LC$_{rand}$ in combination with eq. 3.6, is illustrated in Figure 4.11. Application of LC$_{rand}$ per design leads for some designs to a high fatigue damage estimation standard deviation σ_{est}. By including more LCs in the design set LC$_{rand}$ with an accuracy better or equal to 0.5, 1, 2 and 3% deviation to one in the scatter Figure 4.9, deterioration of fatigue damage estimates is observed in Figure 4.11 and Table 4.5.

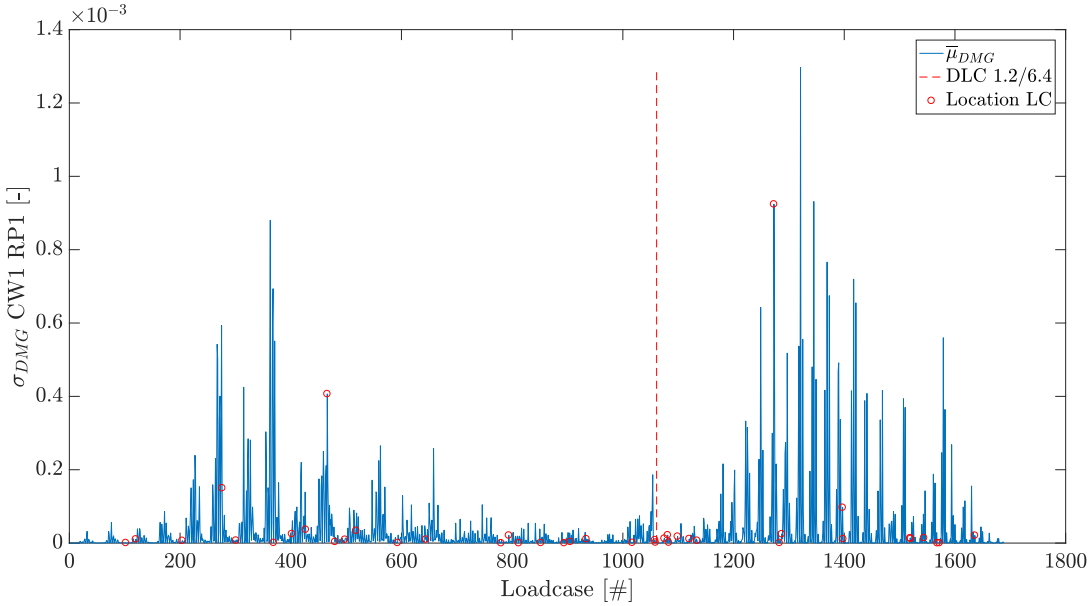

Figure 4.10: *Location of* LC *numbers in* LC$_{rand}$ *within the* LCT .

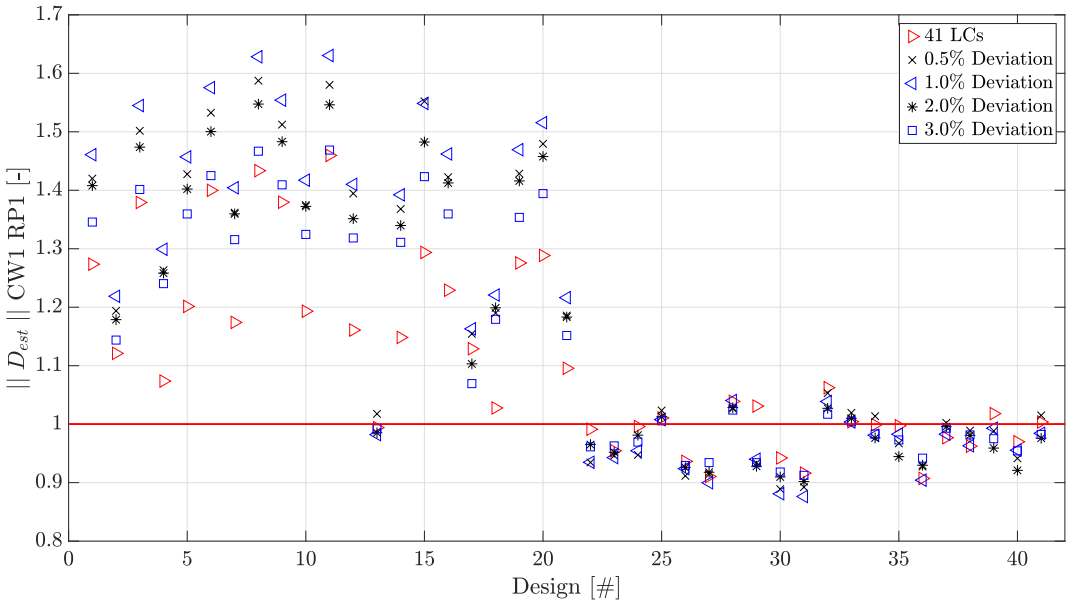

Figure 4.11: *$||D_{est}||$ per design by use of 41* LCs *and eq.* 3.6.

Unlike in the previous approach, increasing the amount of LCs decreases the accuracy. This can again be tracked back to the influence of the global factor in eq. 3.6. Best results are obtained by including 41 LCs, i.e. the LCs connected by the blue line in Figure 4.9.

Table 4.5: *$\overline{\mu}_{est}$ and σ_{est} at different amounts of computed* LCs *using random* LC_{rand} *sets with eq.* 3.6.

Dev. [%]	LCs [#]	$\overline{\mu}_{est}$ [-]	σ_{est} [-]
-	41	1.20	0.28
0.5	113	1.20	0.27
1.0	223	1.17	0.24
2.0	381	1.14	0.18
3.0	529	1.15	0.20

The median factor computation of eq. 3.8 is leading to better results in terms of the fatigue damage estimation mean value $\overline{\mu}_{est}$ and standard deviation σ_{est} over the design set by including 41 LCs, see Table 4.5. Again, a fatigue damage estimation deterioration is observed by including more LCs. This shows, that this method with random LC selection is not robust in this applied form. Therefore, due to the non-ability of improvement, this method is disregarded in further estimation steps, see Table 3.7.

Table 4.6: *$\overline{\mu}_{est}$ and σ_{est} at different amounts of computed* LCs *using random* LC *sets eq.* 3.8.

Dev. [%]	LC [#]	$\overline{\mu}_{est}$ [-]	σ_{est} [-]
-	41	1.14	0.13
0.5	113	1.06	0.15
1.0	223	1.02	0.10
2.0	381	1.00	0.06
3.0	529	1.01	0.07

4.1.1.3 Importance Sampling - Results

The probability distribution mentioned in eq. 3.14, used for random LC selection is illustrated in Appendix A.1, specifically $\overline{\mu}_{DMG}$ CW_1 RP_1. The curve shows the different contributions of specific LCs in the LCT with steep parts for high contributions to the fatigue damage mean value and flat curve for low contributions. Figure 4.12 shows the IS fatigue damage estimation, completed for CW1 RP1 using up to 5000 random LC selections within one randomly selected LC set.

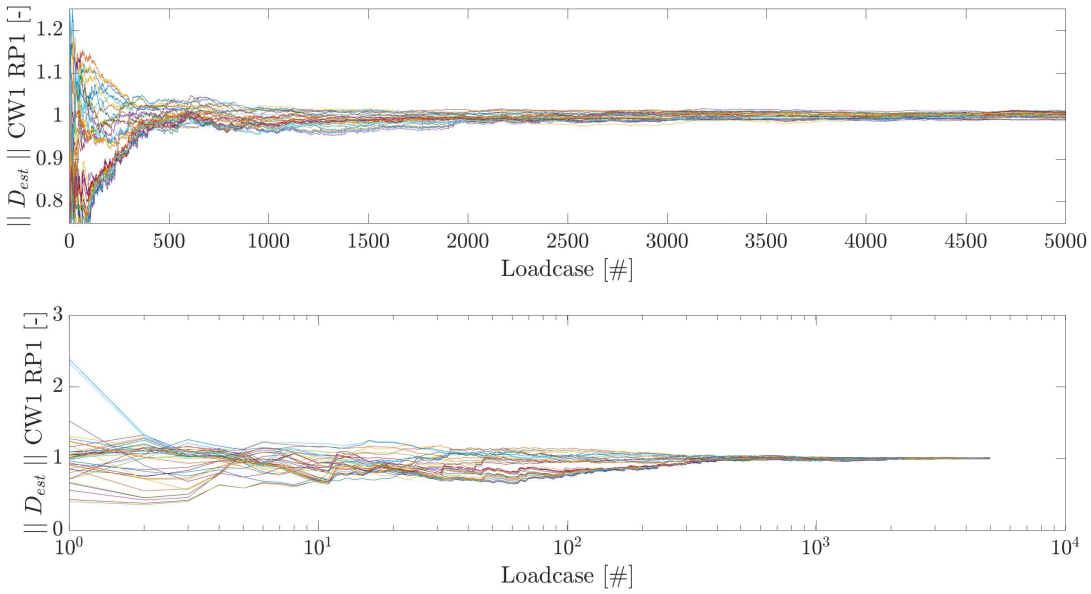

Figure 4.12: IS CW1 RP1 *fatigue damage estimation using eq.* 3.16.

To evaluate the IS method, 500 randomly selected LC sets with 1600 LC each are computed and the resulting $\overline{\mu}_{est}$ and σ_{est} are listed in Table 4.7:

Table 4.7: $\overline{\mu}_{est}$ *and* σ_{est} *at different amounts of computed* LCs *using the* IS *approach in eq.* 3.16.

LC [#]	$\overline{\mu}_{est}$ [-]	σ_{est} [-]
50	1.00	0.08
100	1.00	0.06
200	1.00	0.04
400	1.00	0.03
800	1.00	0.02
1600	1.00	0.02

Comparison of the CW1 RP1 fatigue damage estimation using LC ranking, random LC set and IS method is summarized in Figure 4.13. There, different fatigue damage estimation mean values $\overline{\mu}_{est}$ and standard deviations σ_{est} from Table 4.1 up to Table 4.7 are illustrated.

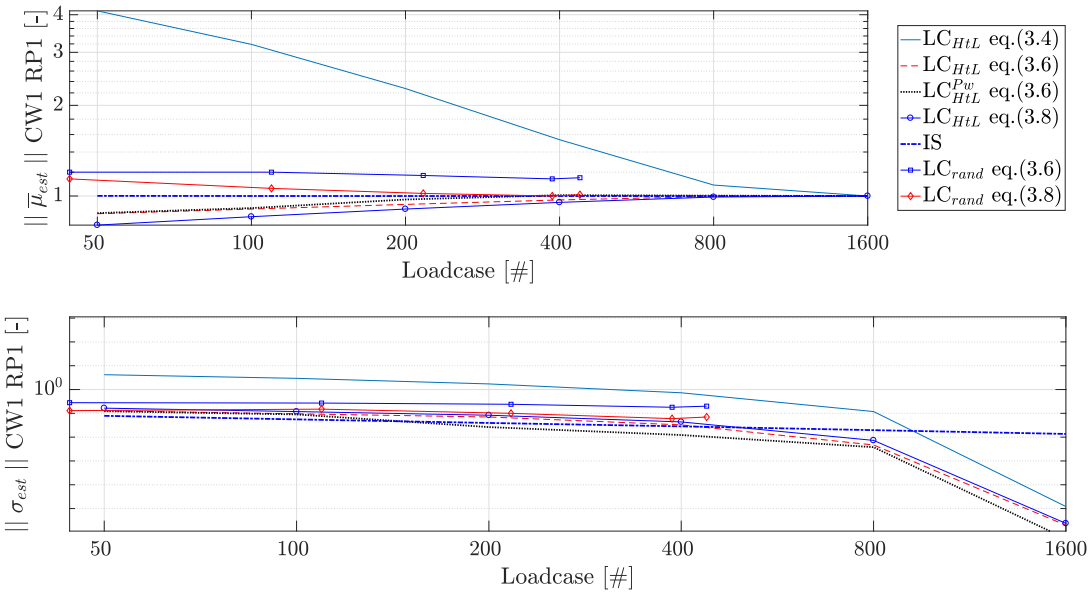

Figure 4.13: *Comparison of mean and standard deviation values of the four presented approaches within this sub-section.*

- The LC ranking approach is producing best results with eq. 3.6 using LC$_{HtL}$ sorting, defined in Figure 4.2. The probability weighted LC sorting LC$^{Pw}_{HtL}$, defined in Figure 4.6, is less favorable in comparison. σ_{est} is reduced in both LC sortings from 800 LC on significantly. The worst results using the LC ranking approach are obtained by the factorless method, using eq. 3.4. There, $\overline{\mu}_{est}$ convergence can be detected after 800 LCs.
- The random LC selection, that produces the optimal scaling factor for $\overline{\mu}_j$, shows as only method within this sub-section no significant improvement of σ_{est} and $\overline{\mu}_{est}$ by including a higher amount of LCs.
- IS is the most favourable fatigue damage estimation method for CW1 RP1. IS stands out by a fast convergence of $\overline{\mu}_{est}$. In terms of standard deviation, IS is decreasing with $1/\sqrt{N}$, while LC ranking methods are more accurate from 800 LC on. Since the objective is to find the most accurate method within the first 120 LCs, IS is still in favor. The single mean for IS improvement is by changing the density function in Appendix A.1. The only requirements of this curve are: monotonically increasing and between values of zero and one. Therefore, it looks promising, that the IS method is leading to a satisfactory damage estimation for the other steps mentioned in Table 3.7.

4.1.2 Step 2: Damage estimation of weld location for 12 positions

This sub-section presents the results of different methods for estimating the twelve radial positions (RP1-12) fatigue damage for circumferential weld one (CW1), i.e. step two in Table 3.7. the MP fatigue damage directionality dependence is the difficult part to tackle, see Appendix A.2. There, the standard deviations over different radial positions variate. Highest variance can be observed in the range of load case (LC) 200-400 and 1200-1500 over the design set. These are also different in height over the radial positions (RPs). For other LCs, the fatigue damage standard deviation is small compared to the latter regions, but the directionality is visible as well, i.e. LC 1-250 and from 1500 on. Fatigue damage standard deviation differences of opposite radial positions are illustrated in Appendix A.3. Those are rather small, due to the bending axis of the almost symmetric structure.

The following approaches are discussed and compared within this sub-section:

- Load case ranking
- Factor approach
- Importance Sampling (IS)

The three approaches are tested and compared with each other at the end of this sub-section. The damage estimation D_{est} of each design is normalized by the true fatigue damage value D^{real}_{fin} of a design location (CW) and RP obtained from a full FLS LCT analysis, resulting in $||D_{est}||$.

4.1.2.1 Load case ranking - Results

Figure 4.14 shows the normalized fatigue damage estimation $||D_{est}||$ over the design set with optimal LC sorting for each RP, LC_{HtL}^{opt} respectively. LC_{HtL}^{opt} represents the LC sorting for each RP from highest to the lowest standard deviation σ_{DMG}, similar to Figure 4.2. Due to directional dependency, the LC_{HtL}^{opt} differs per RP. This leads to a high number of required LCs and disagrees with the main LC reduction objective: high accuracy with less required LCs. Therefore, the single LC sorting LC_{HtL}, defined in Figure 4.2, for one RP is used to estimate fatigue damage as well. Radial $||D_{est}||$ for one exemplary design is illustrated for both LC sortings in Figure 4.14, i.e. upper sub-figure with LC_{HtL}^{opt} and lower with LC_{HtL} using eq. 3.6:

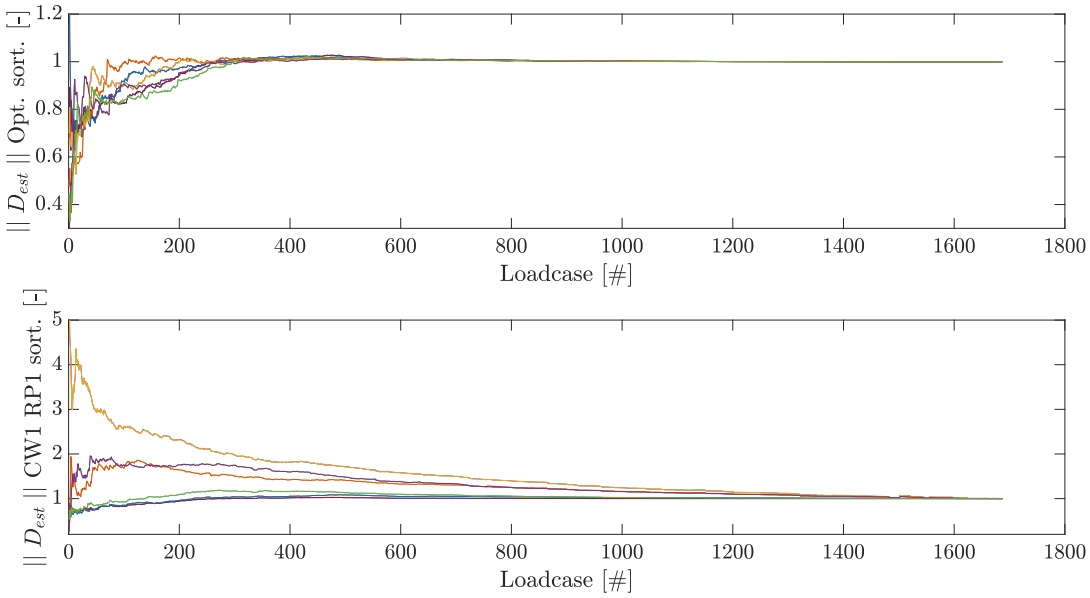

Figure 4.14: *Fatigue damage estimation of location* CW1 *at 12* RPs *for one exemplary design with* LC_{HtL}^{opt} *sorting and eq.* 3.6.

The overall design set fatigue damage estimation standard deviations σ_{est} and mean values $\overline{\mu}_{est}$ of the optimal and single sorting are illustrated in Figure 4.15 and 4.16

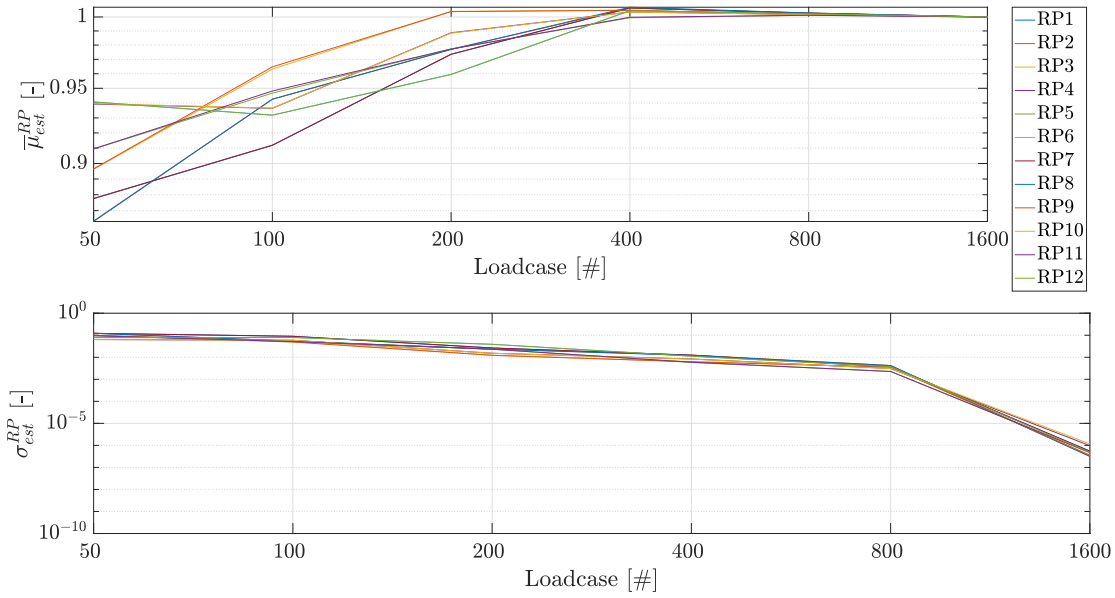

Figure 4.15: *Design set* $\overline{\mu}_{est}^{RP}$ *and* σ_{est}^{RP} *of location* CW1 *at 12* RPs *with* LC_{HtL}^{opt} *for each* RP.

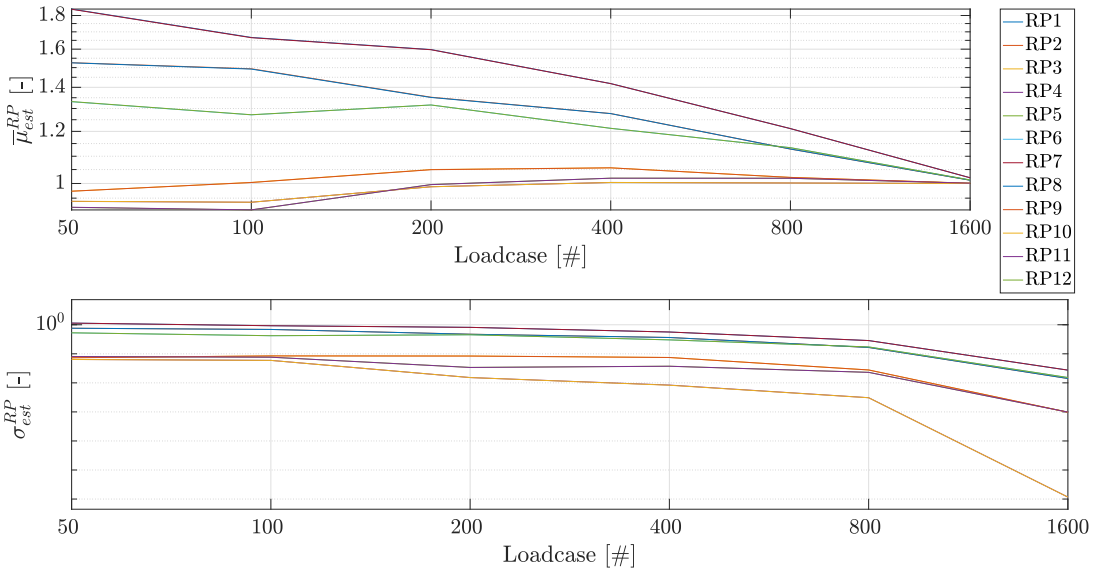

Figure 4.16: *Design set fatigue damage mean value* $\overline{\mu}_{est}^{RP}$ *and standard deviation* σ_{est}^{RP} *of location* CW1 *at 12* RPs *with* LC_{HtL} *using eq.* 3.6.

The conclusion is that the LC_{HtL}^{opt} sorting is not a viable option, since for example at LC step 500, 921 different LCs are required due to different LC sorting. Therefore, the sorting LC_{HtL}^{opt} will not be considered in further fatigue damage estimation steps, see Table 3.7.

Single RP sorting LC_{HtL} is covering the requirements of a small LC set, hence acceptable $||D_{est}||$ accuracy is reached after 1600 LCs only, see Figure 4.16. There, the fatigue damage estimation mean value $\overline{\mu}_{est}^{RP}$ and the standard deviation σ_{est}^{RP} show a converging behavior after 94% of the LCT is computed. Therefore, the LC ranking approach for RP damage estimation will not be regarded anymore for step four in sub-section 4.1.4 for the fatigue estimation of all 24 CWs and twelve RPs.

4.1.2.2 Factor approach - Results

Even though the directional dependence for MP fatigue damage is present over the FLS LCT, D_{fin}^{real} per position do not differ much from other positions, see Figure 4.17. Values of the upper two figures are normalized by RP1. The distribution of the fatigue mean damage damage $\overline{\mu}_{DMG}^{RP}$ is approximately circular shaped, i.e. is not showing any peaks at any RP. The largest standard deviation σ_{DMG}^{RP} of 5% is observed at RP4 and RP10.

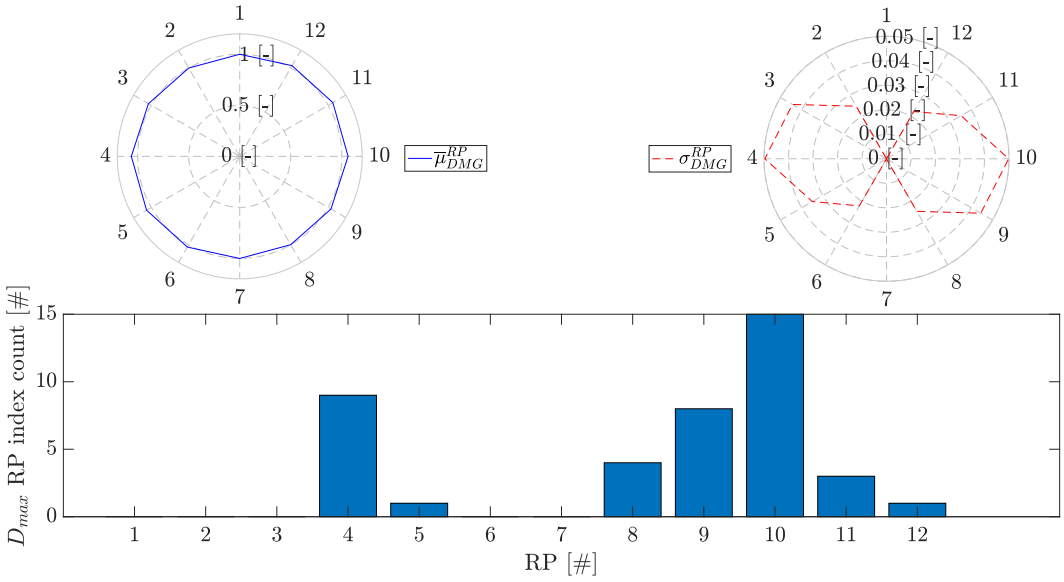

Figure 4.17: *Upper left figure:* RP1 *normalized circumferential weld* CW1 $\overline{\mu}_{DMG}^{RP}$*, upper right figure:* RP1 *normalized* σ_{DMG}^{RP}*, bottom figure: Maximum fatigue damage* D_{max} *radial position* (RP) *index count.*

Maximum damage position count over all designs is shown in the bottom figure. RP4 and RP10 are the governing RPs over the design set, which can be related to the occurring environmental conditions. Based on this knowledge, a fatigue damage estimation factor f_{RP} is computed by use of eq. 3.9 with fatigue damage mean value $\overline{\mu}_{est}^{RP}$ and standard deviation σ_{DMG}^{RP} of the design set for $n = [1, 12]$ and $j = 4$, see Table 4.8. In Figure 4.18 the RP fatigue damage estimation mean value $\overline{\mu}_{est}^{RP}$ and the standard deviation σ_{est}^{RP} per design are listed.

Table 4.8: *Factors f_{RP} obtained by eq. 3.9 for position P1-12 damage estimation.*

RP	f_{RP} [-]	RP	f_{RP} [-]
1	0.99	7	0.99
2	1.00	8	1.00
3	1.00	9	1.00
4	1.00	10	1.00
5	0.97	11	0.97
6	0.97	12	0.97

The clear shift of $\overline{\mu}_{est}$ in Figure 4.18 due to the applied factors is visible. An improvement is possible as long as the RP4 $||D_{est}||$ accuracy is increasing. When the latter has reached the maximum accuracy, the resulting deviations of $||D_{est}||$ are due to the factors in Table 4.8.

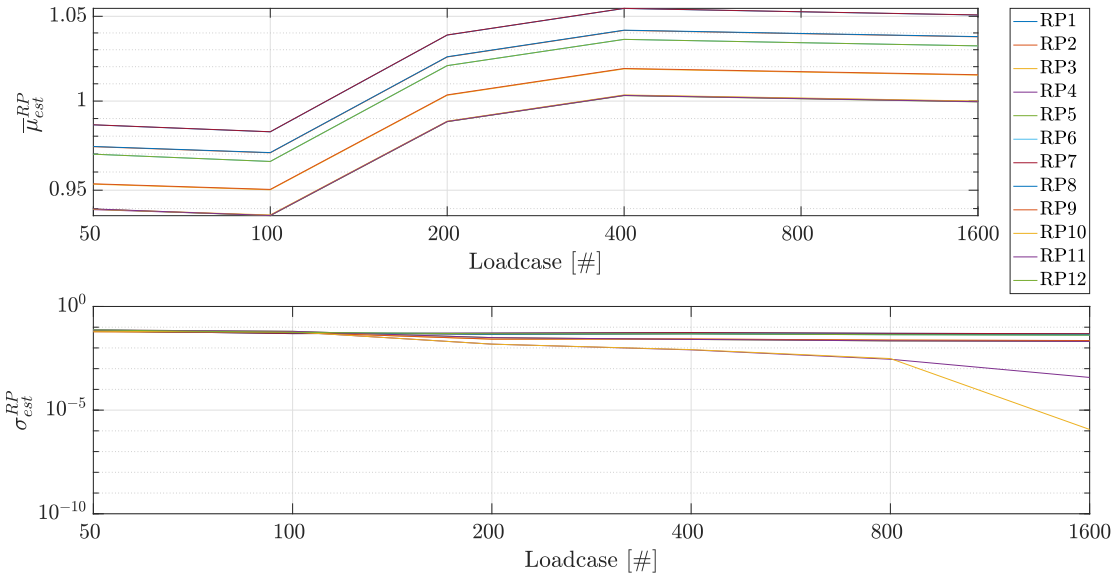

Figure 4.18: *$\overline{\mu}_{est}^{RP}$ and standard deviation σ_{est}^{RP} for an exemplary design* CW1 RP1-12 *using factor f_{RP}.*

4.1.2.3 Importance Sampling - Results

The probability distribution for IS is formed by the mean value for each LC over all twelve RPs for CW1, i.e. $\overline{\mu}_{DMG}$ $\mathrm{CW_1RP_{1-12}}$ in Appendix A.1. The IS fatigue damage estimation using the new probability distribution in eq. 3.16, is illustrated in Figure 4.19.

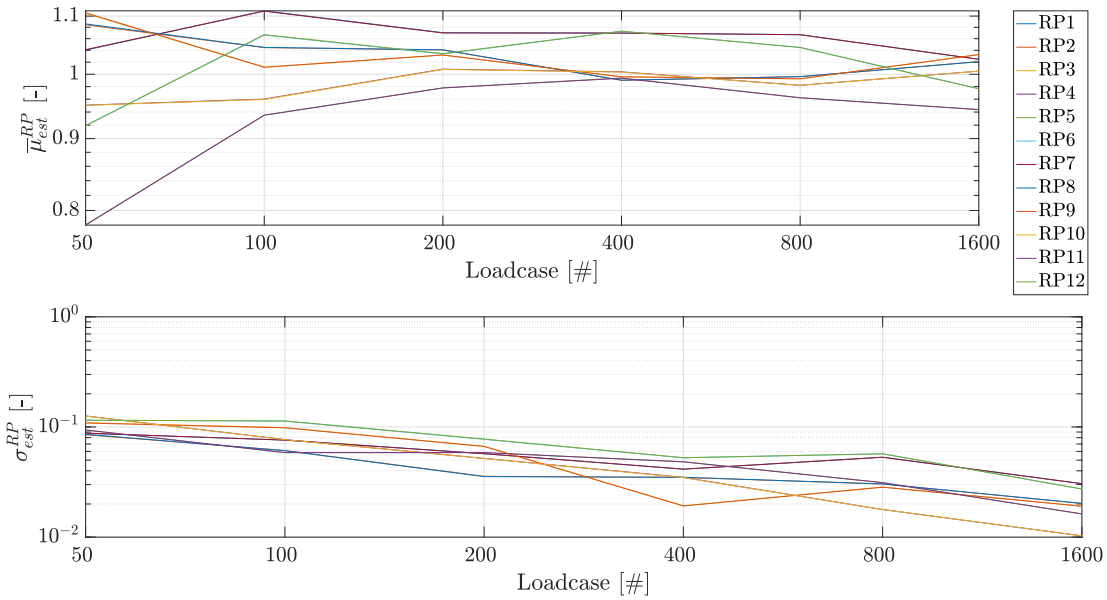

Figure 4.19: IS $||D_{est}||$ *for twelve radial positions using eq.* 3.16 *with one randomly selected* LC *set.*

For the accuracy of the IS method, 500 seeds with random LC sets are used for fatigue damage estimation over the design set. The mean value over all seeds is used to compute the standard deviation σ_{est}^{RP} and the mean value $\overline{\mu}_{est}^{RP}$.

Comparison of the three presented approaches are shown in Appendix A.6 and A.7 in which the fatigue damage estimation standard deviations σ_{est}^{RP} over twelve RPs are illustrated. The corresponding twelve fatigue damage estimation mean values $\overline{\mu}_{est}^{RP}$ are shown in Appendix A.8 and A.9 .

- The LC ranking approach following the LC_{HtL} sorting shows a large variability in terms of σ_{est}^{RP}. Only fast converging estimation is observed for RP4 and RP10, for which the optimal LC sorting is completed. Similar behavior is observed for $\overline{\mu}_{est}^{RP}$. There, the convergence towards D_{fin}^{real} is late, apart from RP4 and RP10. Overall, this method is not suited for RP fatigue damage estimations, due to the large variations of the estimations, apart from RP4 and RP10.
- The design set based factor approach produces better results compared to the LC ranking approach regarding σ_{est}^{RP}. There, up to LC 200 σ_{est}^{RP} is lower compared to IS and the mean value estimation is close to IS. The highest accuracy increase for RP other than for RP4 and RP10 is reached from approximately LC 400 on. From this point on, the shift is visible due to the factor approach, by the following approximately straight line of the estimation mean value $\overline{\mu}_{est}^{RP}$.
- IS is showing satisfying results for σ_{est}^{RP} and $\overline{\mu}_{est}^{RP}$. The variability of σ_{est}^{RP} over radial positions is the smallest one compared to the other approaches. Also $\overline{\mu}_{est}^{RP}$ convergence towards the final true damage value D_{fin}^{real} is reached with a lower amount of LCs.

The conclusion is that the IS method is clear in favor in terms of required LCs and accuracy. Therefore, the IS method is selected for the RP fatigue damage estimation for the last accuracy step in Table 3.7, due to its robust estimations over all RPs.

4.1.3 Step 3: Damage Estimation of 24 weld locations for one position

Since the fatigue damage standard deviation σ_{DMG} for CW1-24 RP1 over the design set for each LC in Figures A.4 and A.5 shows a similarity pattern over all LCs, the following techniques are used for fatigue damage estimation:

- Load case ranking
- Factor approach
- Importance Sampling (IS)

The three approaches are tested and compared with each other at the end of this sub-section. The fatigue damage estimation D_{est} of each design is normalized by the true fatigue damage value D_{fin}^{real} of a design location (CW) and position (RP) obtained from a full FLS LCT analysis, resulting in $||D_{est}||$.

4.1.3.1 Load Case Ranking - Results

In Figure 4.20 the fatigue damage estimation mean value $\overline{\mu}_{est}^{CW}$ and standard deviation σ_{est}^{CW}, over all 24 circumferential welds for RP1 using LC sorting LC_{HtL}, see Section 4.1.1, are illustrated. The resulting large deviations of 22% occur at LC 50 but decrease with increasing computed LC amount. Convergence occurs, similar to accuracy step one of Table 3.7 in Section 4.1.1, at approximately LC 800. Additionally, σ_{est}^{CW} decreases significantly from LC 800 as well.

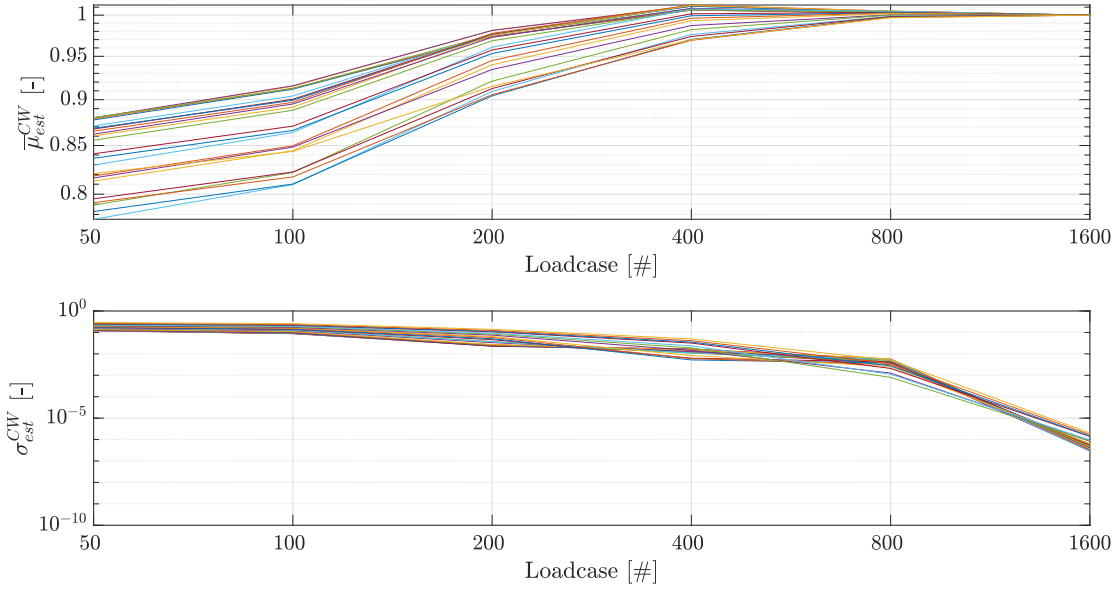

Figure 4.20: *Design set* $\overline{\mu}_{est}^{CW}$ *and* σ_{est}^{CW} *with* LC_{HtL} *for* CW1-24 RP1 *using eq.* 3.6.

4.1.3.2 Factor approach - Results

The factors f_{CW} from eq. 3.10 are obtained by taking the mean value $\overline{\mu}_{DMG}$ and the standard deviation σ_{DMG} over all circumferential welds at RP1, see Figure 4.21. The factors are listed up in Table 4.9. The fatigue damage estimation $||D_{est}||$ is completed by computing actual values of CW1 RP1 with the corresponding LC_{HtL} sorting and eq. 3.6. At the remaining welds the normalized fatigue damage estimations $||D_{est}||$ are computed by the obtained factors f_{CW}.

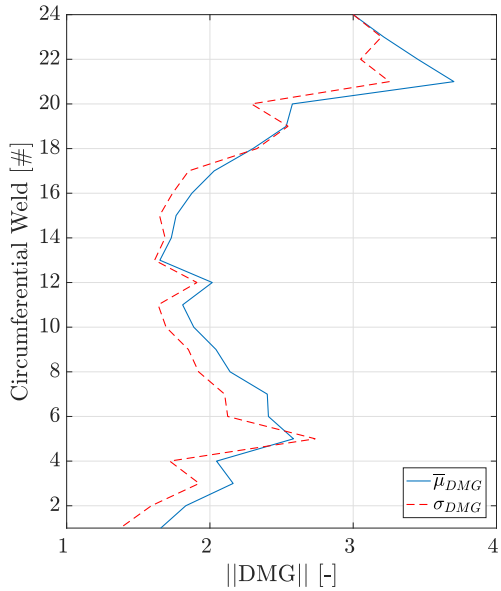

Figure 4.21: *Mean value and standard deviation of damage values over the monopile height.*

Table 4.9: *Factors f_{CW} obtained by eq. 3.10 for circumferential weld* CW1-24 *damage estimation.*

CW	f_{CW} [-]	CW	f_{CW} [-]	CW	f_{CW} [-]	CW	f_{CW} [-]
1	1.00	7	0.66	13	0.46	19	0.59
2	1.10	8	0.44	14	0.34	20	0.85
3	1.06	9	0.38	15	0.37	21	0.39
4	1.16	10	0.34	16	0.44	22	0.48
5	0.67	11	0.35	17	0.48	23	0.32
6	0.77	12	0.31	18	0.58	24	0.21

σ_{est}^{CW} is showing the shift of $\overline{\mu}_{est}^{CW}$ from the real damage value is high and therefore this method will not be selected, see Figure 4.22.

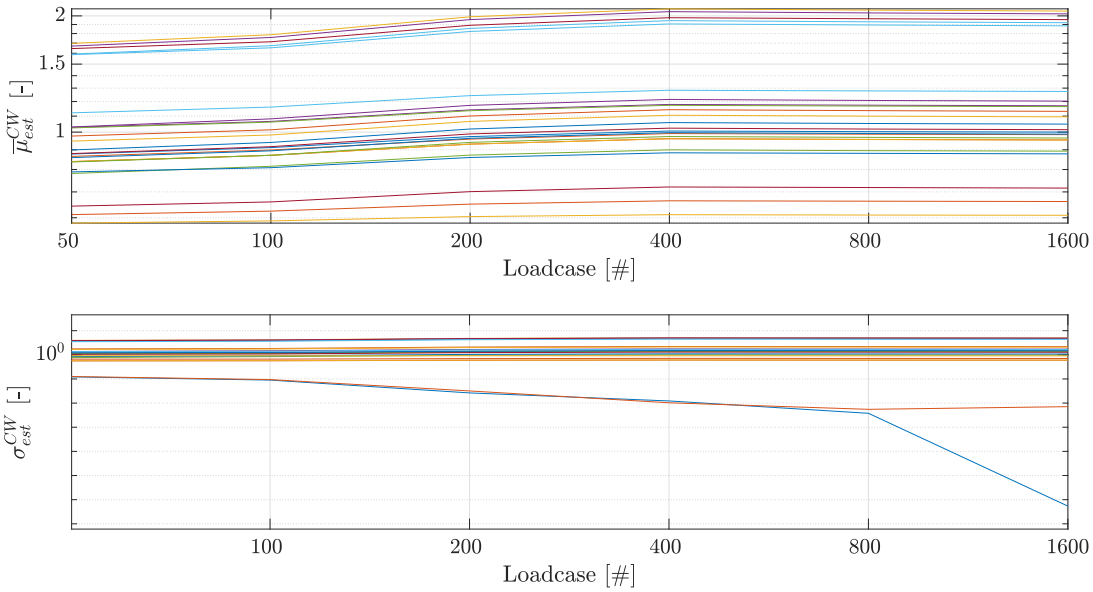

Figure 4.22: *Fatigue damage estimation mean values $\overline{\mu}_{est}^{CW}$ and standard deviations σ_{est}^{CW} for* CW1-24 RP1 *following the factor approach.*

4.1.3.3 Importance Sampling - Results

The IS fatigue damage estimations over all locations (CW1-24) are compared directly to other methods by creating a cumulative probability density distribution, formed by the fatigue damage mean value of all LCs over all locations (CW_{1-24} RP_1), see Appendix A.1. Next, eq. 3.16 is used to estimate the fatigue damage estimation $||D_{est}||$ over the design set, with which the $\overline{\mu}_{est}^{CW}$ and σ_{est}^{CW} are computed. The comparison of the IS σ_{est}^{CW} to other techniques within this sub-section is illustrated in Appendix A.10 to A.13. Additionally $\overline{\mu}_{est}^{CW}$ is shown in Appendix A.14 to A.17.

- For the LC ranking approach $\overline{\mu}_{est}^{CW}$ reaches D_{fin}^{real} at approximately LC 200 for CW1-12. Lower CWs reach convergence between 400 and 800 LCs. The corresponding σ_{est}^{CW} is approximately 1% higher compared to IS for all CWs up to LC 200, but shifts to a lower and rapidly decreasing value from LC 400 on. Therefore, this method is a competitor for the IS method regarding the overall accuracy.
- The design set based factor approach produces the worst results in comparison. Large deviations in $\overline{\mu}_{est}^{CW}$ and high σ_{est}^{CW} show that this method is not estimating fatigue damage over the MP circumferential welds accurately apart from CW1, i.e. the fatigue damage estimations for this CW are completed with the LC sorting from CW1 RP1 LC_{HtL}. Due to inaccuracy and no indication of improvement the factor approach will be disregarded in step four, see Table 3.7.
- The IS method shows fast convergence at LC 50 for $\overline{\mu}_{est}^{CW}$ and decreasing σ_{est}^{CW}, as shown eq. 4.1 over all CWs.

In general, the latter mentioned figures clearly show that by use of IS σ_{est}^{CW} is small and decreasing with similar pattern over all CWs. But also $\overline{\mu}_{est}^{CW}$ is converging faster to the normalized true values compared to the LC

ranking or factor approach. The significant parameter for the approach selection is the $\overline{\mu}_{est}^{CW}$. Therefore, the IS is recommended for the fatigue damage estimation over the three dimensional MP.

4.1.4 Step 4: Damage Estimation of all weld locations and positions

Step four of Table 3.7 is the damage estimation for the complete three dimensional MP, i.e. all 24 circumferential welds (CW) and 12 radial positions (RP). The best LC reduction technique from step one to three in Table 3.7 is used as only method within this sub-Section, i.e. the Importance Sampling (IS) method. The RP fatigue damage standard deviation per weld over the design set is illustrated from Appendix A.18 to A.21. The corresponding mean value is shown from Appendix A.22 up to A.25. This shows that the fatigue damage mean value over the RPs is circular shaped and the highest deviations occur at RP4 and RP10, similar to Section 4.1.2. The required IS cumulative probability density is formed by the mean value of all CWs and RPs $\overline{\mu}_{DMG}\mathrm{CW}_{1-24}$ RP_{1-12} over the design set, see Appendix A.1.

The fatigue damage estimation standard deviations σ_{est}^{CWRP} and mean values $\overline{\mu}_{est}^{CWRP}$ of all CWs and RPs are illustrated in Appendix from A.26 to A.31 . The latter figures are obtained by computing 20 seeds of random 1600 LC sets. Even with a small amount of LCs, the converging behavior is high for all locations and positions. σ_{est}^{CWRP} are in the order of 10^{-2} and decreasing up to 10^{-3}. This confirms the IS method as a general robust and accurate fatigue damage estimation technique and will therefore be used in Section 4.2.

4.2 Genetic Algorithm - Critical Damage and Load Case Reduction Implementation

4.2.1 Critical Damage Evaluation

Implementation of the load case (LC) reduction is completed, as described by eq. 3.17 and 3.18. For this, the accuracies of the IS method over the three dimensional MP are evaluated by the evaluation of v seeds of random LC sets containing stage k LCs, see Figure 3.6. Taking the mean value over all seeds v is leading to σ_{ijk}^{CWRP} and $\overline{\mu}_{ijk}^{CWRP}$, see eq. 4.1 and 4.2.

$$\sigma_{ijk}^{CWRP} = \overline{\sigma_{vijk}^{CWRP}} \tag{4.1}$$

$$\overline{\mu}_{ijk}^{CWRP} = \overline{\overline{\mu}_{vijk}^{CWRP}} \tag{4.2}$$

Results for LC steps between 30 and 120 in steps of 10 LCs are given in Appendix A.32 up to A.36. The latter expressions are used in eq. 3.17 for fatigue damage estimation.

A fatigue damage estimation trial of stage $k = 4$ is shown in Figure 4.23. There, the difference between the fatigue damage values of a converged GA result are computed by using the full FLS LCT and the IS estimation with $n = 3$, see eq. 3.17. The resulting graphical illustration is shown in Figure 4.23. Negative values imply a fatigue damage over-estimation. Hence, positive values an under-estimation.

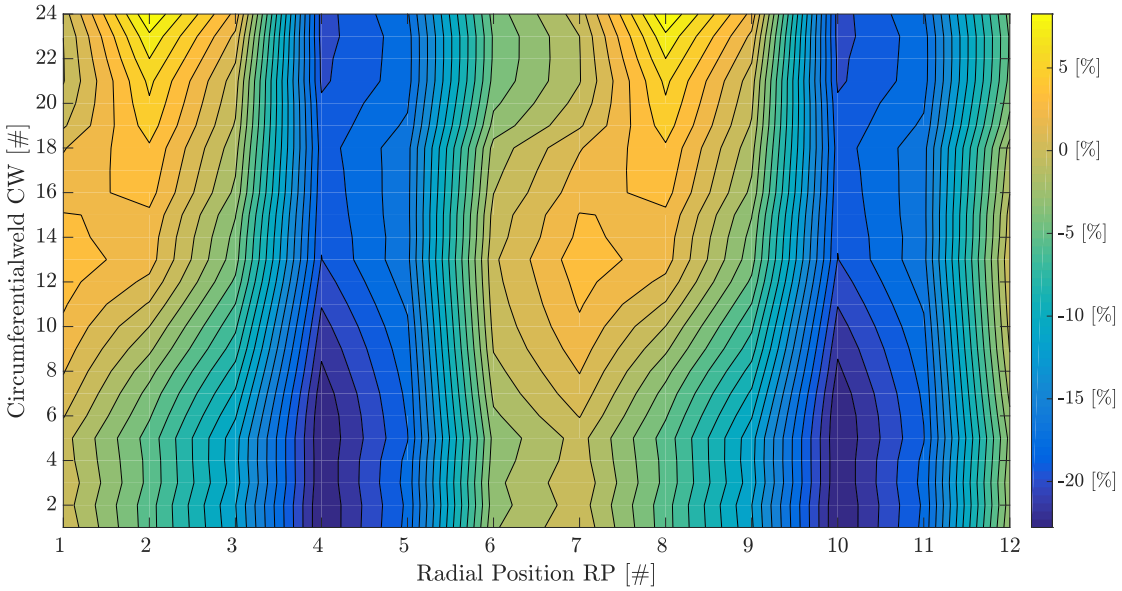

Figure 4.23: *Difference of a full* FLS LCT *and estimated fatigue damage results using* IS *at 120* LCs *with a multiplicative* $n = 3$ *in* eq. 4.2*, normalized by the fatigue damage values of the full* FLS LCT *analysis.*

Fatigue damage over- and underestimation can be explained by the applied IS method. There, LCs are selected randomly from the cumulative probability distribution, see section 3.3.4. Subsequently, the random selection is influenced by the probability distribution. There, LCs with a higher contribution to the mean value have a higher probability to be chosen, compared to others with a low contribution. This causes that LCs with a certain wind/wave misalignment are selected multiple times. This affects the corresponding RPs regarding the bending axis. Since final fatigue damage values per RP do not differ much from each other, a small error between the estimation and the full FLS LCT analysis is expected.

In Figure 4.24 the positions and locations containing the maximum fatigue damage per design are counted over the design set. These positions and locations are also over-estimated in Figure 4.23, specifically RP four, eight, nine, ten and eleven.

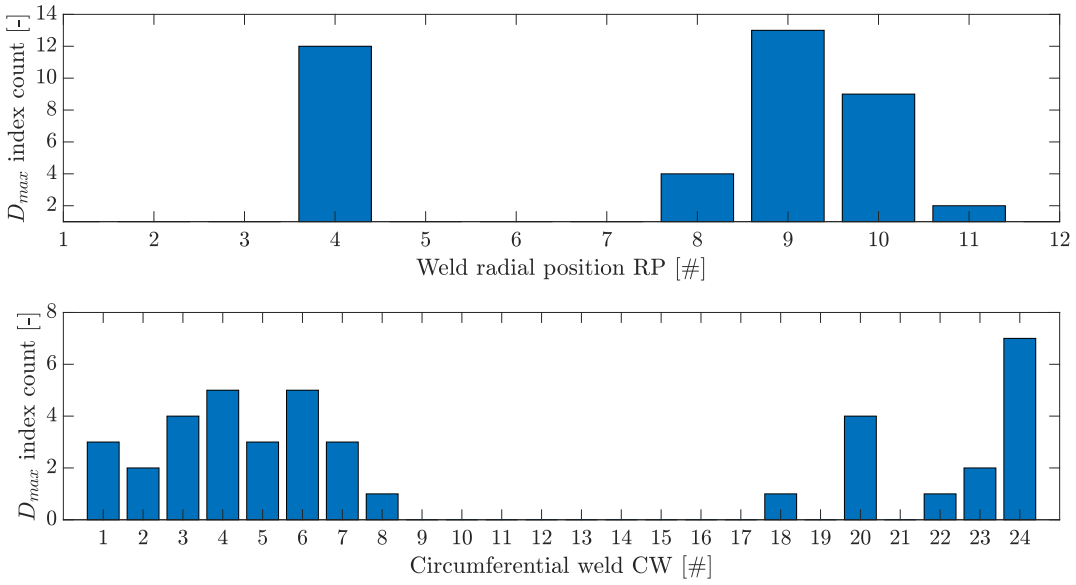

Figure 4.24: *Fatigue damage maximum count per* RP *and* CW*.*

Additionally the governing locations over height are located in the upper MP sections (around CW4) and some at the lower sections (around CW20). Governing RPs can be tracked back to the environmental conditions within this area. MP height does not influence the latter governing RP statement, see Figure 4.23. Therefore, it

can be concluded that the governing fatigue positions are the located in the over-estimated RPs for this OWT site. Deviations of the critical damage values ΔD_{crit} between the full FLS LCT analysis and an IS stage $k = 4$ fatigue estimation are listed up in Table 4.10 by variation of the multiplicative factor n in eq. 3.17:

Table 4.10: *Comparison of critical fatigue damage D_{crit} estimations using 120* LCs *with full* FLS LCT *fatigue damage results.*

n	3	2	1	0
ΔD_{crit}[%]	22.57	15.28	7.99	0.71

Three dimensional fatigue damage estimation by including $n = 1$ in eq. 3.17 Figure 4.25 is obtained:

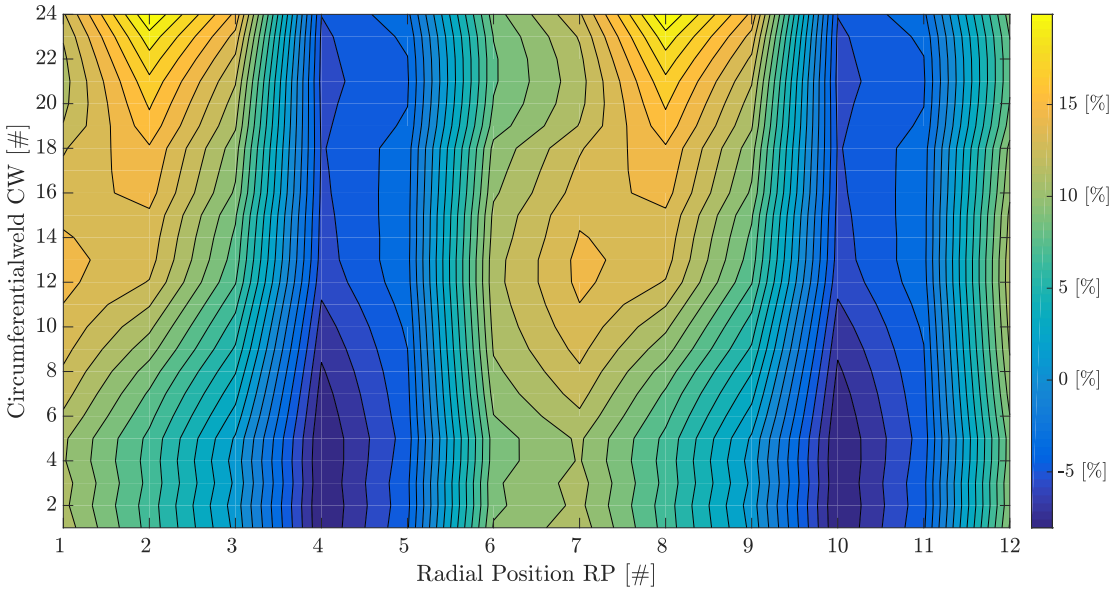

Figure 4.25: *Difference of a full* FLS LCT *and estimated fatigue damage results using* IS *at 120* LCs *with a multiplicative $n = 1$ in* eq. 4.2*, normalized by the fatigue damage values of the full FLS LCT analysis.*

Implementing a multiplicative factor n smaller than three in eq. 3.17 still leads to an over-estimation for the governing RPs, but also an under-estimation in other positions. A smaller error towards the critical fatigue damage weld is more important than over-estimating all welds. Additionally, the multiplicative n is not set to zero, even though the accuracy is high, since a fatigue damage estimation safety factor in form of a statistical value should be included, due to the appearance of different design geometries in the genetic algorithm (GA). In other words by factorizing $\mathbf{I}_k$ in eq. 3.17 with $n = 1$, the whole fatigue damage estimation is less conservative for the regions of interest and will allow the GA to converge closer to the the real fatigue damage constraint c_{FLS}. Therefore, the multiplicative factor n is set equal to one in Section 4.3.

4.2.2 Load Case Reduction Methodology Comparison

Two methodologies presented in Section 3.4.1 are evaluated in Figure 4.26. The first approach follows a constant FLS constraint evaluation over all generations and the second an accuracy refinement with increasing generation. In other words the constant LC approach contains 120 LCs and the refining accuracy approach is following the LCs increase from Figure 3.6.

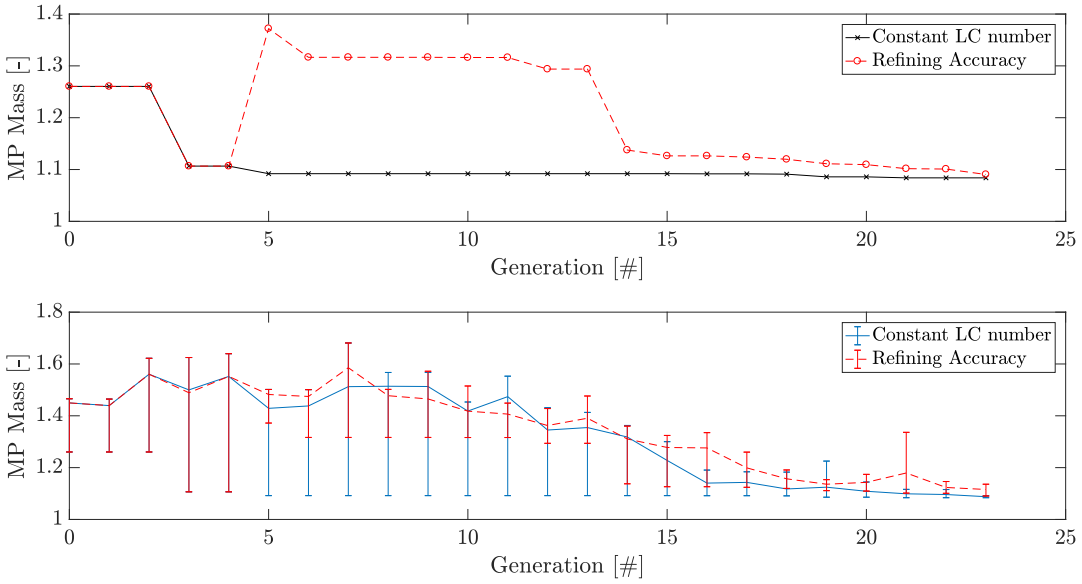

Figure 4.26: *Comparison of the* FLS *implementation methodologies showing the best fitness values per generation (upper Figure) and the best/mean/worst scores per generation (lower Figure).*

Sub-figures of Figure 4.26 show a fitness decrease at generation five. This can be explained by the change of accuracy at the 5th generation in the FLS constraint evaluation, see Figure 3.6. There, an increase from 30 to 50 LCs is recorded. The fitness increases for the refining accuracy approach after generation five and does not show fitness decreases in the following generations. The constant LC approach increases fitness by 0.8% from generation five on. Both methods converged at generation 23. In terms of computation time, the stage approach converged 40% faster compared to the constant LC number approach with a final MP weight deviation of +9% to the constant LC approach. By setting the function tolerance to a lower value, the GA would converge in a later generation, but might find the same optimum of the constant LC number approach. The refining accuracy approach is a viable and faster method to optimize the structure. Improvement of the accuracy in LC stage 30 is required. This can be completed by changing the multiplicative factor n in the critical damage estimation eq. 3.17, or augmenting the LCs for this step. Also, an optimization of the stage generation number and LCs can be completed. Overall, this would not be time efficient for the application in this form for another OWT location.

Nevertheless, taking the disadvantage of a higher computation time, but having a higher accuracy for the creation of the primary steel mass versus lifetime graph, the constant LC approach is applied in Section 4.3, in which 120 LCs for the GA FLS constraint evaluation are used.

4.3 Genetic Algorithm - Mass versus Lifetime Curve

For each projected lifetime, two converged GA results are obtained by use of the constant LC approach with 120 LCs, explained in Section 3.4.1 . The converged GA results are subsequently evaluated with a full FLS LCT analysis. This full analysis results to the governing limiting actual lifetime. The resulting lifetime, critical weld location of full and reduced FLS LCT and generation number of GA convergence are shown in Table 4.11.

Table 4.11: *Key points of converged* GA *results including the projected lifetime* (PLT), actual lifetime (ALT), converged generation number (CGN) location D_{crit}^{loc} with circumferential weld (CW) and radial position information (RP) compared to the full (FLS LCT) analysis.

PLT [yrs]	ALT [yrs]	D_{crit}^{loc} Est. [CW|RP]	D_{crit}^{loc} Full [CW|RP]	CGN[#]
25	26.65	4|10	4|10	33
	26.37	4|10	4|4	37
50	49.05	5|4	4|12	23
	49.11	4|4	4|12	23
75	76.26	21|10	22|9	41
	74.07	21|10	21|9	27
100	106.18	5|10	23|9	32
	106.15	5|10	22|9	39

In the upper sub-Figures 4.27, 4.28, 4.29 and 4.30 the best fitness over generation number is illustrated. Additionally, in the lower subplots the populations best/worst and mean fitness per generation are shown.

The GA best fitness evolution for a projected lifetime of 25 years, seen in Figure 4.27, converges towards the same optimum over different paths. At generation four a fitness increase of approximately 15% for both GA runs is recorded. Also, the best/worst/mean fitness in the lower subplot is the same for the first eight generations. This can be explained by the methodology of the GA. The first generation is the same for both runs, since the GA forms the first population with the given optimization parameter boundaries, shown in Table 3.4. There, the GA uses the extreme values of the constrained parameters for a broad search space at the starting generation.

The best fitness increases significantly by 10% at generation 17 for the second GA run, see Figure 4.27, and increases with a small slope until convergence at different amount of generations. Hence, for the first run, the increase in fitness starts at generation 13 and increases smoother in comparison to the second GA run. Both runs, for a projected lifetime of 25 years, converge at a different amount of generations, but reach approximately the same MP mass and lifetime with a difference of 0.07% and 1.04% from run number one.

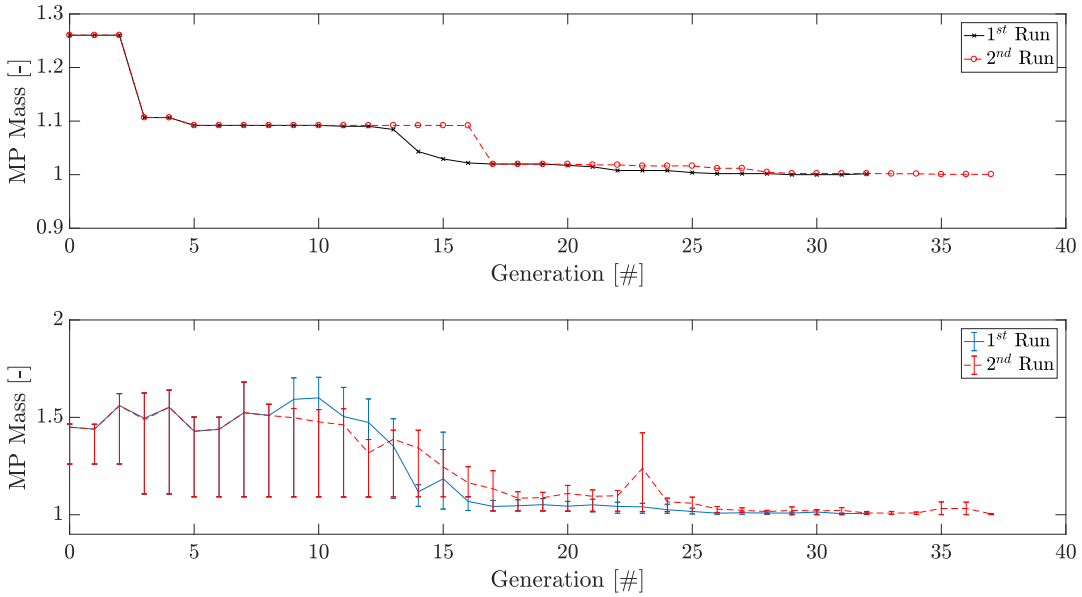

Figure 4.27: *Normalized* GA *best fitness (upper figure) and the populations best/worst and mean scores (lower Figure) for two* GA MP *optimization runs for a projected lifetime of 25 years.*

Figure 4.28 shows two GA runs with a projected lifetime of 50 years. There, the GA finds the same global optimum with the same best fitness evolution, but with different fitness distributions over the population after generation six. The fitness in Figure 4.28 increases per generation in small portions and converges at the same amount of generations. The final converged MP masses and lifetimes deviate by +0.28% and 0.12% from run number one.

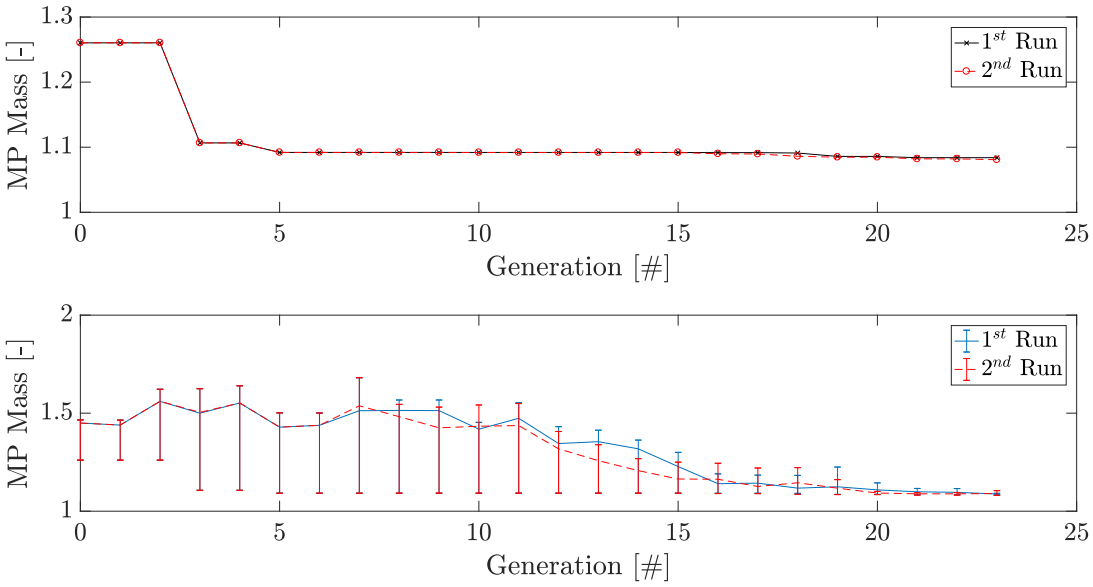

Figure 4.28: *Normalized* GA *best fitness (upper figure) and the populations best/worst and mean scores (lower Figure) for two* GA MP *optimization runs for a projected 50 years lifetime.*

The GA run for a projected lifetime of 75 years is illustrated in Figure 4.29. Both GA runs converge towards approximately the same MP mass and lifetime with a difference of +0.31% and -2.86% from run number one. Large fitness increases are recorded at different generations for both runs, i.e. generation 13, 18, 22 for GA run one and generation 13, 23. Significant difference between the runs is the generation number of convergence, which is 26 for run two and 41 for run one.

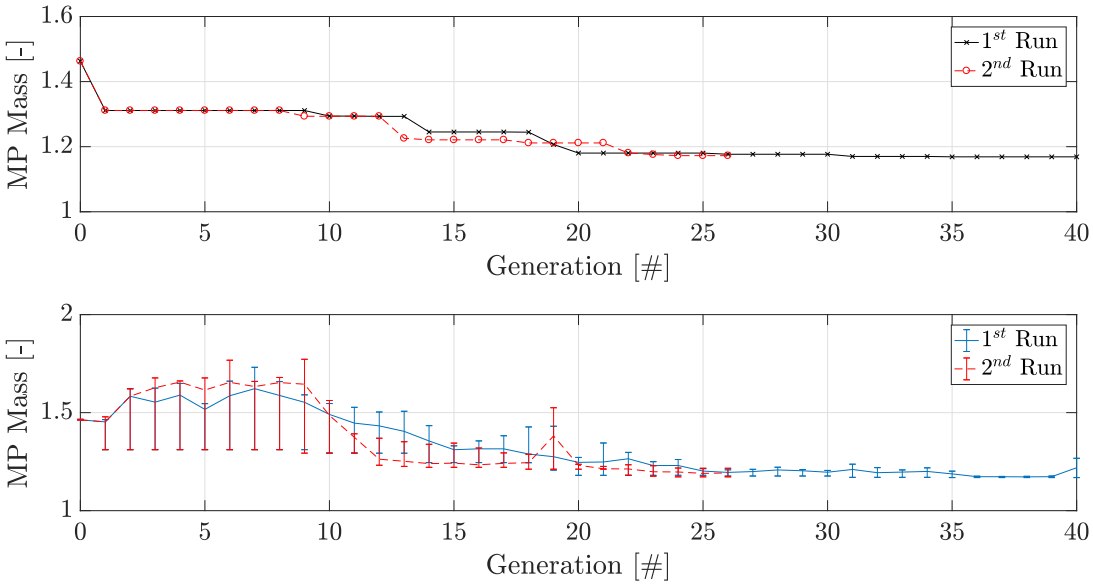

Figure 4.29: *Normalized* GA *best fitness (upper figure) and the populations best/worst and mean scores (lower Figure) for two* GA MP *optimization runs for a projected lifetime of 75 years.*

Figure 4.30 shows a large fitness increase at generation four, ten and twelve, of 6.5% 12.9% and 3.3% respectively. The difference of the MP with respect to mass and lifetime results to +1.01% and -0.03% from run number one. This result has the largest difference in terms of MP weight, whereas the lifetime difference is the smallest compared to the projected lifetime GA runs for 25, 50 and 75 years.

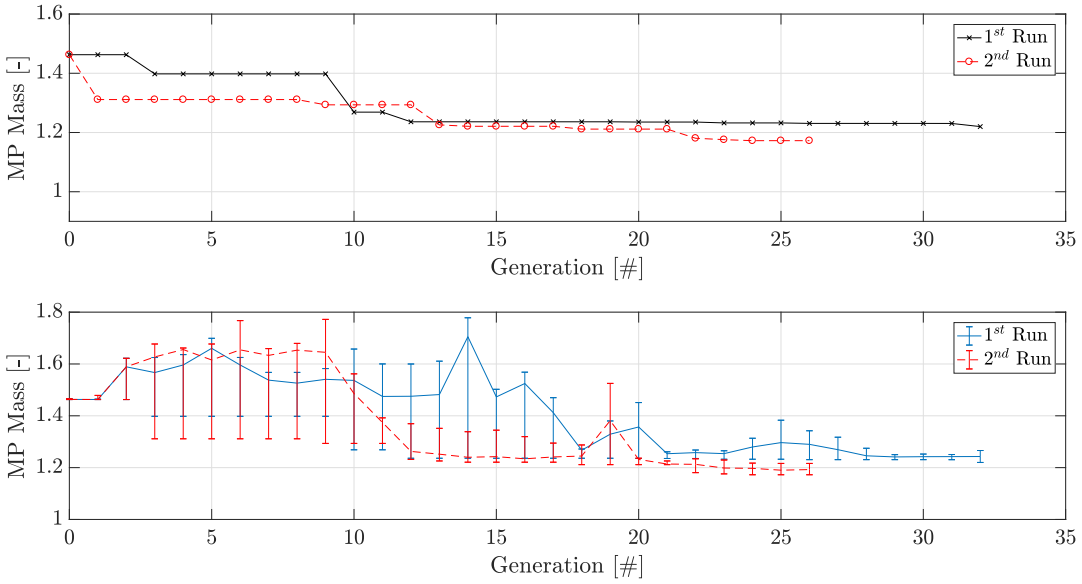

Figure 4.30: *Normalized* GA *best fitness (upper figure) and the populations best/worst and mean scores (lower Figure) for two* GA MP *optimization runs for a projected lifetime of 100 years.*

The overall time of one exemplary GA run is illustrated in Figure 4.31. This illustration gives an indication of the computation times per each individual, but may change depending on the cluster loading degree. The evaluation average per individual is at 7.85 minutes. This is approximately 60% higher than anticipated, i.e. the limit of approximately five minutes per individual. Computation times per individual in the individual range between 75-90, 270-305 and 335-360 are increased due to cluster loading within this time frame. Other computations are completed with an average of 6.6 minutes. This is still approximately 30% higher than planned. Results close to zero are designs that did not pass the frequency and buckling constraint and are therefore not evaluated for the FLS, i.e. the exiting mechanism explained Section 3.2.2 is activated.

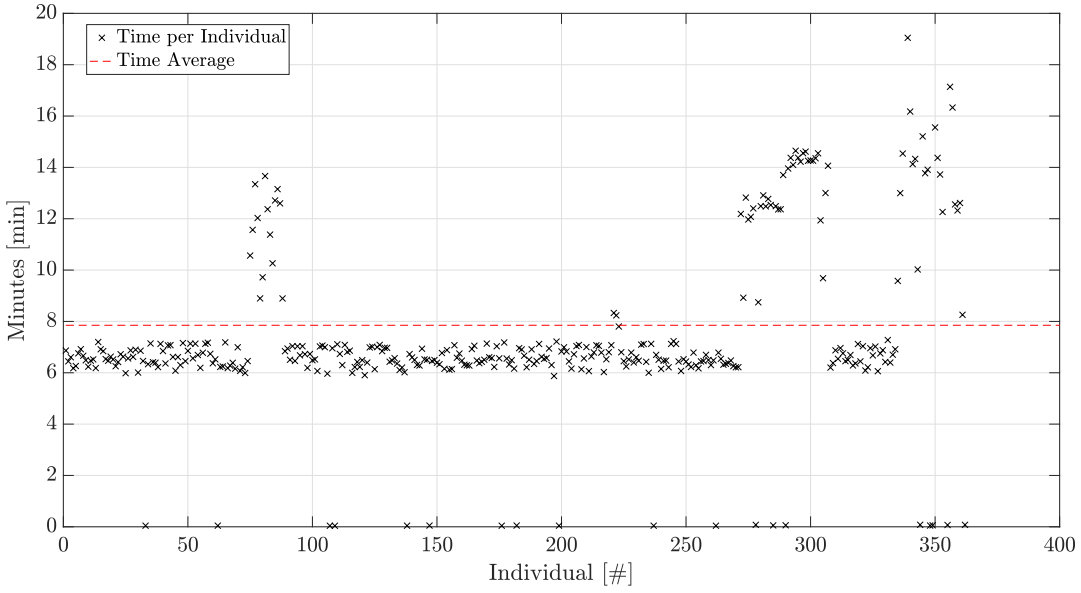

Figure 4.31: *Exemplary required time per individual for a GA optimization with a projected lifetime of 25 years.*

In Figure 4.32 the structure identifying parameters of converged GA results are plotted per projected lifetime. All results are normalized by the first GA run variables with a projected lifetime of 25 years. The averaged frequency is increasing approximately linearly by +3.4% from a projected lifetime of 25 to 75 years by +4.6% up to a projected lifetime of 100 years. Overall, the natural frequencies move towards the upper limit of the soft-stiff region. In comparison to other parameters in Figure 4.32 the frequency is the only increasing trend that can be observed in both GA runs. Therefore, it can be concluded that for one projected lifetime many

different designs with different geometries are possible, but the resulting frequencies and masses are similar. Also, the hot spots in terms of critical fatigue damage show similarities, see Table 4.11.

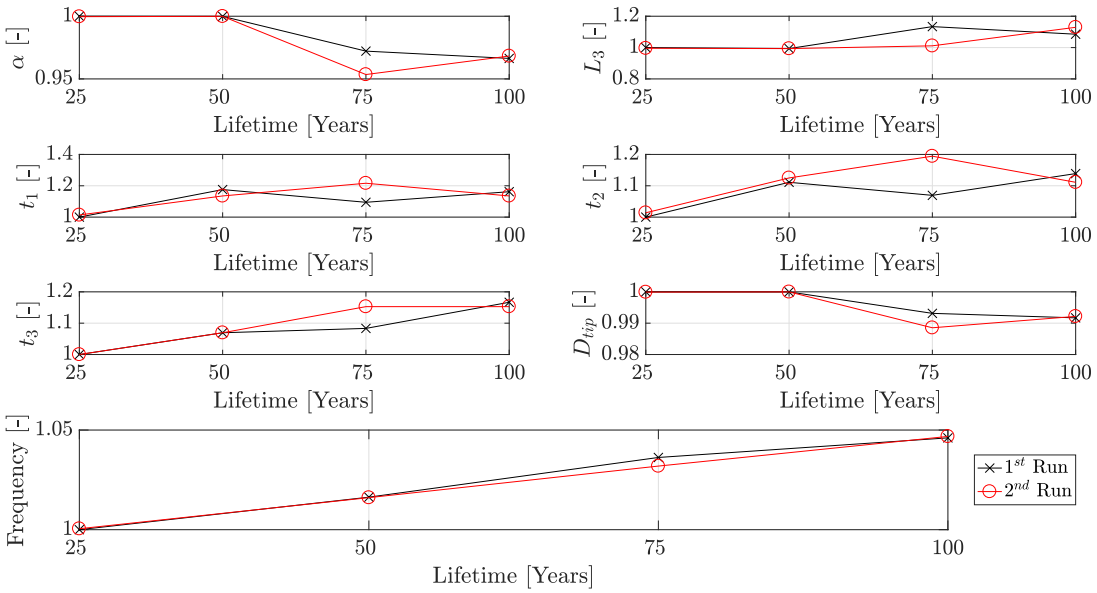

Figure 4.32: *Evolution of converged* GA MP *normalized designs parameters.*

For run number one the cone angle decreased from a projected lifetime of 25 to 50 years by -10^{-4}% and by -2.78% towards a projected lifetime of 75 years and -3.36% for 100 years. The cone angle decrease is leading to a MP tip diameter decrease for run number one of $2.2{\cdot}10^{-3}$ at 50 years, -0.68% at 75 years and additional -0.83% for a projected lifetime of 100 years. Run number two instead leads to decreases for 50, 75 and a projected lifetime of 100 years of -3.34%, -0.01%, -4.65% and -3.17%.

The block length L_3 for run number one increased by +13.38% from a projected lifetime of 50 to 75 years, while for run number two the increase results to only 1.01%. Thus, in the first run, the GA increased the structure frequency for a projected lifetime of 75 years significantly by augmenting the embedment depth, decreasing the wall thicknesses of block one and two and increasing the block three wall thickness. Hence, for run number two the frequency increase is reached by an increase of all wall thicknesses. From 75 years for GA run number one, the embedment depth L_3 of 100 years decreases by -4.85%, but the wall thicknesses t_1, t_2 and t_3 instead are increasing by 6.76%, 6.94% and 8.33% from 75 to 100 years. From a projected lifetime of 75 years the embedment depth L_3 increases by +12.9% and the wall thicknesses t_1, t_2 and t_3 decreases from a projected lifetime of 75 years by -4.1%, -4.2% and -6.9%

Significant differences in geometry between the GA runs for one projected lifetime can be observed at projected lifetimes of 75 and 100 years at block one, two and three wall thicknesses, i.e. t_1, t_2 and t_3. Nevertheless, for all runs the projected lifetimes are similar in terms of lifetime and MP mass.

Figure 4.33 and 4.34 show box plots for the optimization variables from eq. 3.1. The box plots are sorted by the projected lifetime and GA runs, i.e. two per projected lifetime, and normalized by the design of the first GA run with a projected lifetime of 25 years.

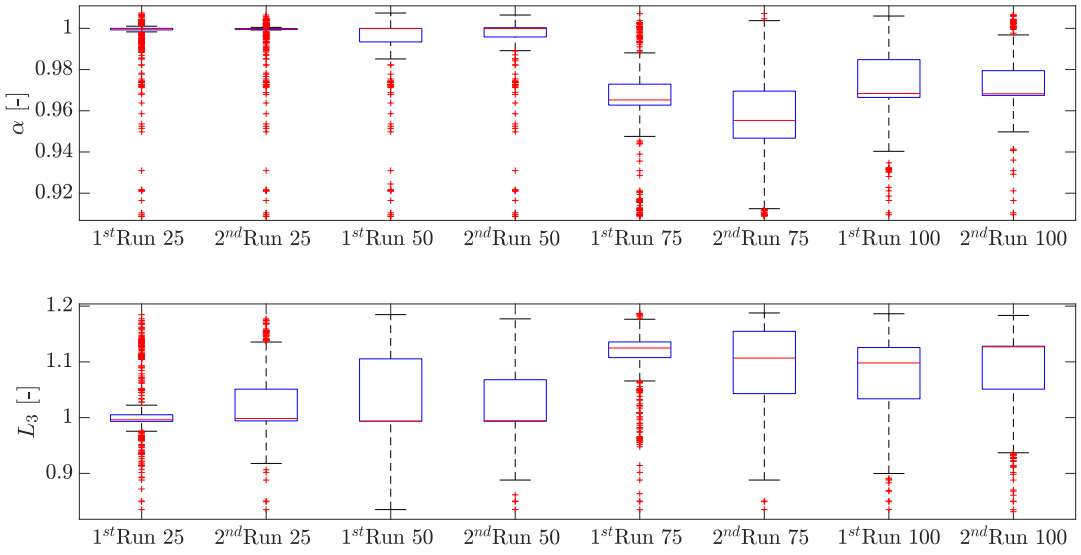

Figure 4.33: *Normalized cone angle α and segment length L_3 box plots per lifetime* GA *optimization runs.*

Overall, the cone angle is in the upper half of the boundaries listed in Table 3.4. The cone angle for a projected lifetime of 25 years shows a thin distribution containing some outliers. In comparison the cone angle distribution over the populations of a projected lifetime of 75 and 100 years are larger. Thus, the GA with a projected lifetime of 75 and 100 years searched in a larger cone angle region compared to a projected lifetime of 25 years. The algorithm searched for the global optimum more by variation of L_3 and the wall thicknesses as shown in sub-Figure 4.34.

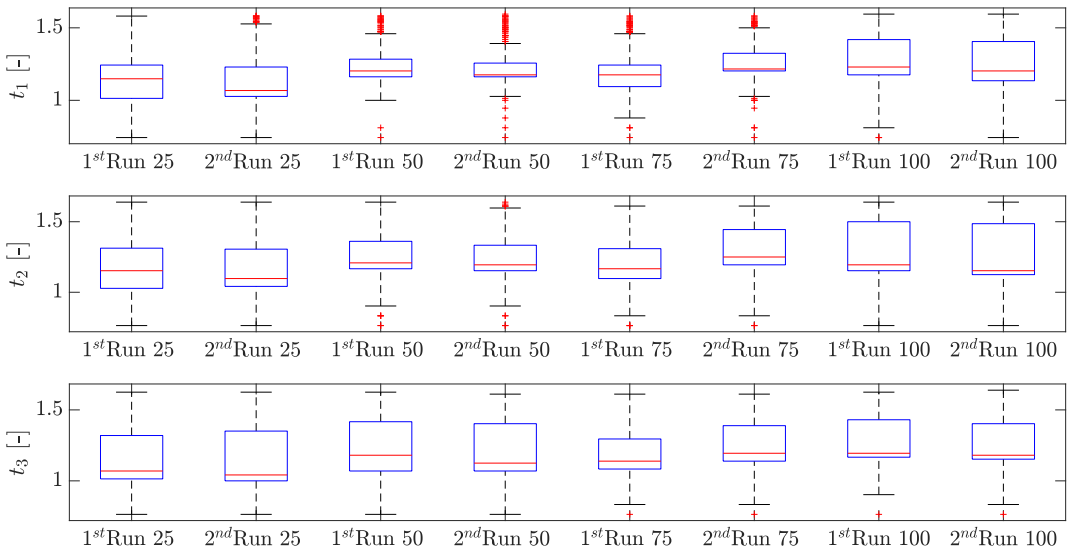

Figure 4.34: *Normalized wall thickness t_1,t_2 and t_3 box plots per lifetime* GA *optimization runs.*

Figure 4.34 shows larger variable distributions for all block wall thicknesses box plots. Combining the lifetime of Table 4.11 with the corresponding primary steel MP masses leads to the mass versus life time graph in Figure 4.35.

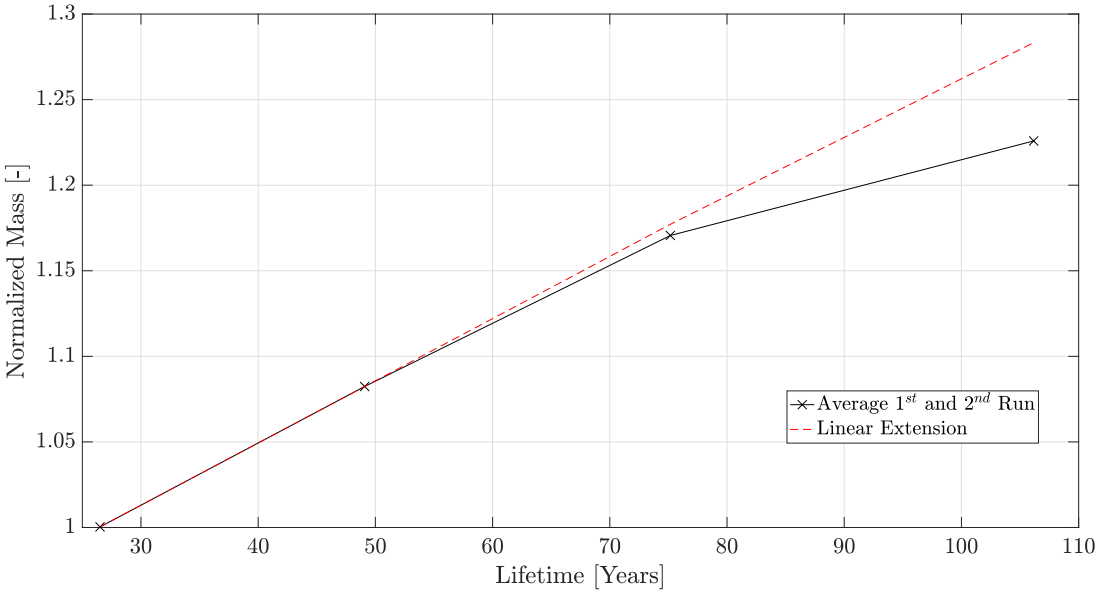

Figure 4.35: *Normalized primary steel mass versus lifetime curve with converged* GA MP *designs.*

The latter figure shows the average of the MP masses and lifetimes. The dashed red linear line is the linear extension of the MP mass with a projected lifetime of 25 and 50 years. A small deviation from the linear line can be observed at a projected lifetime of 75 years, i.e. 0.65% and a significant deviation at a projected lifetime of 100 years, i.e. 5.74%. Overall steepness of the curve is moderate. In terms of an extended projected lifetime, the flattening of the Curve towards a lifetime of 100 years illustrates an important finding, i.e. 90 years of projected lifetime with a design fatigue factor (DFF) equal to three results to 30 years. There, the steel mass required is approximately 3% lower compared to the linear line in Figure 4.35. The flattening curve of a physical point of view makes sense by regarding Figure 4.32. There, the increase of the frequency is almost linear. This implies that the first natural frequency is moving away from the wave excitation frequencies 4.36 and that the stiffness of the structure increases. It is expected that the flattening continues until reaching the 3P region, i.e. the right end of the soft-stiff region. The required frequency increase, on the basis of a projected lifetime of 25 years, to reach the lower 3P soft-stiff limit is approximately 25%. An increase of that rate until reaching the 3P region would be out of the feasible lifetime range, i.e. approximately 580 years with a DFF of one. Therefore, the conclusion is that the potential of a longer design lifetime with current fatigue estimation methods is present.

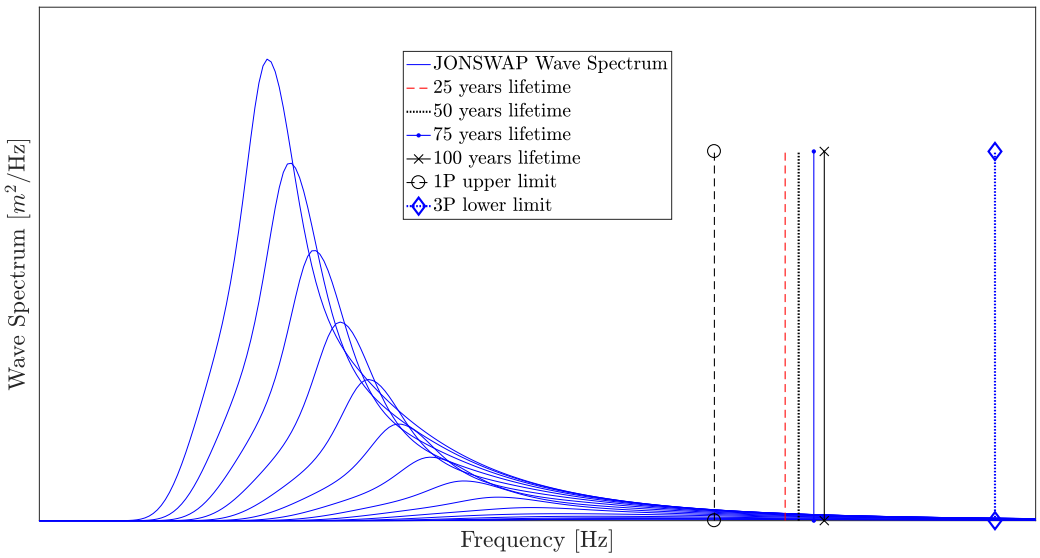

Figure 4.36: *Schematic illustration including averaged frequencies of the* GA MP *designs and the considered* JONSWAP *wave spectra.*

Note that the curve in Figure 4.35 is created for one specific OWT location. Since fatigue damage is influenced strongly by the environment, the steepness of the curve may change for other locations. Therefore, the presented curve should be interpreted as trend but not in terms of absolute numbers.

5 | Conclusions and Future Research

Within this graduation project a connection of the genetic algorithm (GA) with current state of the art in offshore wind energy fatigue limit state (FLS) monopile (MP) support structure certification is completed.

Firstly, different methodologies of load case reduction and GA implementations are presented. Best results in terms of accuracy and load case reduction are obtained by Importance Sampling (IS). With the latter, load case reductions of 93% of the original FLS load case table (LCT) can be achieved with a fatigue damage critical weld estimation accuracy up to 93.4%, compared to the full FLS LCT simulation for a full three dimensional MP support structure. An important outcome of this graduation project is the prove that the projected lifetime can be included in the GA as a constraint, despite numerous design evaluations with current state of the art rules and recommendations using industry design tools for OWT certification, in a feasible time frame. Therefore, the successful implementation of the IS method opened new doors for offshore wind energy support structure optimization.

Secondly, in terms of GA implementation a simple form of changing FLS constraint evaluations for overall optimization speed improvement is compared to a constant evaluation. The time reduction with changing constraint evaluation is attaining a 9% MP mass result difference by 60% faster computation. Therefore, the changing evaluation is a feasible candidate for fast optimization.

Thirdly, the implementation of discrete wall thickness steps in the GA optimization brought the resulting MP design towards real design conditions and produced satisfying results without the appearance of problems within the GA optimization. Similar to the changing constraint evaluation, discrete wall thickness steps are an intervention in the methodology of the original GA.

Fourthly, the GA model leads to converged GA MP designs for different projected lifetimes. Connection of the latter are results in the primary steel MP mass versus lifetime curve in Figure 4.35. The curve shows that the required added mass for this OWT site with a design fatigue factor of three and a projected lifetime of 25 years is below 18%. The flattening of the curve towards 100 years reaches 22% mass increase measured from a projected lifetime of 25 years with a design fatigue factor of three. This is considered to be an indicator of possible worth of extended design lifetime.

The completion of the four graduation project objectives mentioned above, leads in further steps to the answer of the research question in Chapter 1:

Is it worth planning for lifetime extension for monopile-based offshore wind turbines?

The answer is, yes, there is potential worth of planning for extended lifetime for offshore wind turbine MP based support structures for this location. In case the MP steel mass is directly related to the structure costs, the MP lifetime can be extended by additional small investments in steel mass compared to the full structure costs. Outcoming additional years of service will possibly decrease and in further steps the cost of energy. By use of this curve, a trade-off between maintenance strategy and additional mass can be completed. The chosen maintenance strategy is leading to a design fatigue factor and by comparison of the resulting additional steel and maintenance costs, the most favourable solution should be selected. Most striking point for this trade-off, is the location dependent distance to a nearby harbor. The maintenance planning over a lifetime brings larger uncertainty compared to more steel investments in the design phase, because maintenance is strongly depended on the weather windows for safe offshore work, which cannot be predicted far ahead. Therefore, in case of a tie in terms of costs, steel investments may be favored. Concluding from this, the possibility to complete an automatized optimization of OWT MP support structures following regulations can lead to a decision basis for the most favourable solution for a specific OWT site.

Within the trade-off between the increased projected lifetime and maintenance costs, the expenditures for the installation of the MPs, need to be accounted for. Subsequently, with increasing MP mass the amount of ships with the appropriate lifting capacity is decreasing. Therefore, the installation concepts with respect to the distance to the storage harbor, related operation costs and required conical piece for the driving hammer need to be included in the decision.

The presented mass versus lifetime graph is representing the primary MP steel mass. The secondary steel mass, such as cathodic protection, access ladders and boat landing steel masses are kept constant for all different designs. For different projected lifetimes the appurtenance wall thicknesses may increase as well, due to fatigue loading. Additionally, the cathodic protection mass increases with the diameter of the MP sections. This would increase the added mass along the structure and affect the frequency, i.e. a lowering effect. Since the changes are expected to be small, their overall impact on the graph is as well. Changes in geometry of the access ladders and boat landing in terms of size are not expected, since the water depth and sea environment, for which the wind turbine is planned, stays approximately the same, e.g. due to inclusion of sea level rise.

The turbine, tower and TP are not part of the optimization process within this graduation project. In case the turbine size increases, it leads to a tower and transition piece mass increase. With a larger mass to carry, the MP mass would increase as well. Subsequently, to match the frequency criteria, the MP diameter would increase. Further, the wave forcing would increase and thus also the fatigue loading, due to the larger diameter. Higher fatigue loading leads to larger wall thicknesses. From a certain point on, the heavy top mass has a frequency lowering effect [31]. The frequency for different lifetimes in Section 4.3 is almost increasing linearly, therefore the MP would need additional stiffness to cover the frequency requirement and to move away from the excitation range for the fatigue loading. An assessment for each specific project following the mentioned trade-off methodology is recommended.

Future research recommendations for offshore MP optimization using the GA on the basis of this thesis are:

- Implementation of more **optimization variables**. The inclusion of more parameters, such as wall thickness segments and cone section length, may lead to more a optimized structure. Also, the implementation of the TP and tower in the optimization process may lead to an overall optimized support structure.
- An FE model for the **soil modeling** may be implemented for the possibility of higher accuracy of soil damping instead of a constant parameter from experience.
- Variation of the **damping values** in order to obtain the effect on the mass versus lifetime curve.
- Implementation of **ultimate limit states** in the constraint evaluation would complete the full certification primary steel analysis. There, a pre- analysis of governing load cases should be completed in order to save computational effort.
- Further analysis of the **changing constraint evaluation** within the GA. Within this graduation project a simplified accuracy step is tested. In case of creating a conditional based accuracy increase, the methodology may lead to a faster convergence of the algorithm. Also, the same methodology can be pursued by implementing different safety factors of the IS fatigue damage load case reduction for different accuracy steps.
- Within this thesis only mass optimization is completed. By implementation of a logistic cost reduction and other optimization processes the optimization can be increased to a **multi-objective optimization**.
- Elaboration of the **mass versus lifetime graph** with different settings, such as location, water depth, environment. This will show the changing slope for different influencing parameters. In general, this study can be completed for each project. This curve can give the worth of extended design lifetimes for a given site beforehand.
- Performance testing of the **Importance Sampling** method. This includes the application for other offshore wind turbine locations. The creation of the probability distribution curve for the load case selection by only one or two designs of a location will show the fast applicability of the method for the offshore wind industry. Also the applicability of the IS method for variating and not fixed circumferential weld locations over the MP height should be elaborated. Since the methodology is dealing with design load cases, it is recommended to test this method for other support structure types, e.g. jackets. Due to the complicated geometry of the latter structure type, this method may be limited.

Bibliography

[1] I. Pineda, A. Ho, A. Mbistrova, and G. Corbetta. The European offshore wind industry - key trends and statistics 2015. Technical report, EWEA, 2016.

[2] J. van der Tempel. *Design of Support Structures for Offshore Wind Turbines*. PhD thesis, Delft University of Technology, April 2006. `https://repository.tudelft.nl/islandora/object/uuid:ae69666e-3190-4b22-84ed-2ed44c23e670?collection=research`.

[3] M.O.L. Hansen. *Aerodynamics of Wind Turbines*. Taylor Francis, 2nd edition, 2008.

[4] Ramboll. *Rosap Users Guide (Confidential)*, 2017.

[5] International Standard. *Wind turbines – Part 3: Design requirements for offshore wind turbines*, 2009. IEC-61400.

[6] Det Norske Veritas AS. *Support structures for wind turbines*, 2016. DNVGL-ST-0126.

[7] S.N. Sivanandam and S.N. Deepa. *Introduction to Genetic Algorithms*. Springer-Verlag Berlin Heidelberg, 2008. doi:10.1007/978-3-540-73190-0.

[8] Det Norske Veritas AS. *Fatigue Design of Offshore Steel Structures*, 2014. DNVGL-RP-C203.

[9] J. Moccia, A. Arapogianni, J. Wilkes, C. Kjaer, and R. Gruet. Pure Power -Wind energy targets for 2020 and 2030 - A report by the European Wind Energy Association. Technical report, EWEA, 2011.

[10] A. Arapogianni et al. Deep water The next step for offshore wind energy. Technical report, EWEA, July 2013.

[11] Det Norske Veritas AS. *Design of Offshore Wind Turbine Structures*, 2014. DNV-OS-J101.

[12] S. Duffuaa and A. Raouf. *Planning and control of maintenance systems : modelling and analysis*. Cham: Springer, 2nd edition, 2015. doi:10.1007/978-3-319-19803-3.

[13] T. Fischer. *Mitigation of Aerodynamic and Hydrodynamic Induced Loads of Offshore Wind Turbines*. PhD thesis, University of Stuttgart, July 2012.

[14] W.E. De Vries, N.K. Vemula, P. Passon, T. Fischer, D. Kaufer, D. Matha, B. Schmidt, and F. Vorpahl. Final report wp 4.2: Support Structure Concepts for Deep Water sites: Deliverable d4.2.8 (wp4: Offshore Foundations and Support Structures). Technical report, Upwind, 2011. `https://repository.tudelft.nl/islandora/object/uuid:4d009175-4cc4-4a90-881c-9ffb056b0806?collection=research`.

[15] M. Muskulus and S. Schafhirt. Design Optimization of Wind Turbine Support Structures—A Review. *Journal of Ocean and Wind Energy*, 1(1):12–22, February 2014.

[16] K.H. Chew, E.Y.K. Ng, K. Tai, M. Muskulus, and D. Zwick. Offshore Wind Turbine Jacket Substructure: A Comparison Study Between Four-Legged and Three-Legged Designs. *Journal of Ocean and Wind Energy*, 1(2):74–81, 2014.

[17] T. Gentils, L. Wang, and A. Kolios. Integrated structural optimisation of offshore wind turbine support structures based on finite element analysis and genetic algorithm. *Applied Energy*, 199(1):187–204, August 2017. doi: 10.1016/j.apenergy.2017.05.009.

[18] S. Yoshida. Wind Turbine Tower Otimization Method using a Genetic Algorithm. *Wind Engineering*, 30(6):453–469, December 2006. doi:10.1260/030952406779994150.

[19] S. Schafhirt, D. Zwick, and M. Muskulus. Reanalysis of Jacket Support Structure for Computer-Aided Optimization of Offshore Wind Turbines with a Genetic Algorithm. *Journal of Ocean and Wind Energy*, 1(4):209–216, November 2014.

[20] L.B. Pasamontes, F.G. Torres, D. Zwick, M. Muskulus, and S. Schafhirt. Support Structure Optimization for Offshore Wind Turbines with a Genetic Algorithm. *Proceedings of the ASME 2014 33rd International Conference on Ocean, Offshore and Arctic Engineering Offshore and Arctic Engineering*, June 2014.

[21] Germanischer Lloyd. *Rules and Guidelines, IV - Industrial Services, Part 1 Guideline for the Certification of Offshore Wind Turbines*, 2010.

[22] M. Randolph and S. Gourvenec. *Offshore Geotechnical Engineering.* Taylor& Francis, 2011.

[23] Germanischer Lloyd. *Rules and Guidelines, IV - Industrial Services, Part 2 Guideline for the Certification of Offshore Wind Turbines*, 2005.

[24] M. Durstewitz and B. Lange. *Sea-Wind-Power: Research at the first german offshore wind farm alpha ventus.* Springer-Verlag Berlin, 2016.

[25] S. Yıldırım and İ. Özkol. Wind Turbine Tower Optimization under Various Requirements by Using Genetic Algorithm. *Engineering*, 2:641–647, 2010. doi: 10.4236/eng.2010.28082.

[26] T. Worzyk. *Submarine power cables : design, installation, repair, environmental aspects.* Springer Dordrecht, 2009.

[27] E. Topham and D. McMillan. Sustainable decommissioning of an offshore wind farm. *Renewable Energy*, 102:470–480, 2017. doi:10.1016/j.renene.2016.10.066.

[28] P.D. Andersen, A. Bonou, J. Beauson, and P. Brøndsted. Recycling of Wind Turbines. *DTU International Energy Report 2014*, pages 91–97, 2014.

[29] S. Schwartz and K. Argyriadis. Analysis of the Fatigue Loading of an Offshore Wind Turbine using Time and Frequency Domain Methods. *Proceedings of the European Wind Energy Conference*, 2017.

[30] F. Vorpahl, H. Schwarze, T. Fischer, M. Seidel, and J. Jonkman. Offshore Wind Turbine Environment, Loads, Simulation, and Design. *WIREs Energy Environ*, 2(5):548–570, 2013. doi: 10.1002/wene.52.

[31] M.L.A. Segeren and N.F.B. Diepeveen. Influence of the Rotor Nacelle Assembly Mass on the Design of Monopile Foundations. *Heron*, 59(1):17–36, 2014.

[32] J.R. Morison. The Force Distribution Exerted by Surface Waves on Piles. Technical report, University of California, Berkeley, 1953.

[33] R.C. MacCamy et al. Wave Forces on Piles: A Diffraction Theory. Technical report, Corps of Engineers, 1954.

[34] O.M. Faltinsen. *Sea Loads on Ships and Offshore Structures.* Cambridge University Press, 1990.

[35] Det Norske Veritas AS. *Environmental Conditions and Environmental Loads*, 2014. DNV-RP-C205.

[36] American Petroleum Institute. *Recommended Practice for Planning, Designing and Constructing Fixed Offshore Platforms—Working Stress Design*, 2000.

[37] R.M. Osgood. Dynamic Characterization Testing of Wind Turbines. Technical report, NREL, May 2001. NREL/TP-500-30070.

[38] C. LeBlanc. *Design of Offshore Wind Turbine Support Structures.* PhD thesis, Aalborg University, 2009.

[39] M. Arshad and B. O'Kelly. Offshore Wind Support Structures - A Review. *Proceedings of the Institution of Civil Engineers - Energy*, 166(4):139–152, November 2013. doi:10.1680/ener.12.00019.

[40] H.M. Hegm and K.M. Maalawi. Structural Design Optimization of Wind Turbine Towers. *Computers and Structures*, 74(6):649–666, February 2000. doi:10.1016/S0045-7949(99)00079-6.

[41] F.J. Savenije and J.M. Peeringa. Aero-elastic simulation of offshore wind turbines in the frequency domain. Technical report, ECN, November 2009. ECN-E–09-060.

[42] A.F. Hobbacher. *Recommendations for Fatigue Design of Welded Joints and Components.* Springer International Publishing, 2016.

[43] J. Schijve. *Fatigue of Structures and Materials.* Dordrecht:Springer, 2009.

[44] M. Matsuishi and T.Endo. Fatigue of Metals Subjected to Varying Stress. *The Japan Society of Mechanical Engineering*, pages 37–40, 1968.

[45] NORSOK. *Design of steel structures*, 2004. NORSOK N-004.

[46] 4C Offshore. `http://www.4coffshore.com/windfarms/vessels.aspx?catid=3`. Online, accessed 01-September-2017.

[47] O. Kramer. *Genetic Algorithms Essentials.* Springer, 2017. doi:10.1007/978-3-319-52156-5.

[48] M.Mitchell. *An Introduction to Genetic Algorithms*. Cambridge, Mass.: MIT Press, 5th edition, 1996.

[49] R. Haupt and H. Douglas. *Genetic algorithms in electromagnetics*. Hoboken, N.J.: IEEE Press, 2007. doi:10.1002/047010628X.

[50] MathWorks ®. Global Optimization Toolbox. User's Guide. Matlab R2017a. Technical report, MathWorks, 2017.

[51] K. Hasselmann et al. *Measurements of Wind-Wave Growth and Swell Decay during the Joint North Sea Wave Project (JONSWAP)*. Deutschess Hydrographisches Institut, Hamburg, 1973.

[52] Germanischer Lloyd. *Guideline for the Certification of Offshore Wind Turbines, Rules and Guidelines, IV - Industrial Services, Part 1 Guideline for the Certification of Offshore Wind Turbines*, 2010.

[53] J.D. Wheeler. Method for Calculating Forces Produced by Irregular Waves. *Society of Petroleum Engineers*, 22(03):359–367, March 1970.

[54] S. Øye. *FLEX5 manual*, 1999.

[55] P.A. Passon. *Offshore Wind Turbine Foundation Design*. PhD thesis, Technical University of Denmark, March 2015.

[56] K. Deb. An efficient constraint handling method for genetic algorithms. *Computer Methods in Applied Mechanics and Engineering*, 186(2):311–338, June 2000. doi:10.1016/S0045-7825(99)00389-8.

[57] W.H. Press. *Numerical Recipes in C: The Art of Scientific Computing*. Cambridge University Press, 2nd edition, 2002.

[58] J. Bucklew. *Introduction into Rare Event Simulation*. Springer, 2004. doi:10.1007/978-1-4757-4078-3.

[59] Det Norske Veritas AS. *Loads and site conditions for wind turbines*, 2016. DNVGL-ST-0437.

[60] S.K. Haigh. Foundations for offshore wind turbines. *8th International Conference on Physical Modelling in Geotechnics*, January 2014. doi:10.1201/b16200-13.

[61] D. Kallehave, B.W. Byrne, C. LeBlanc Thilsted, and K.K Mikkelsen. Optimization of monopiles for offshore wind turbines. *Philosophical transactions. Series A, Mathematical, physical, and engineering sciences*, 373(2035), January 2015. doi: 10.1098/rsta.2014.0100.

[62] C. Leth. *Improved Design Basis for Laterally Loaded Large Diameter Pile: Experimental Based Approach*. PhD thesis, Aalborg University, December 2013.

[63] C.M.Fontana, W.Carswell, S.R. Arwade, D.J. DeGroot, and A.T. Myers. Sensitivity of the Dynamic Response of Monopile-Supported Offshore Wind Turbines to Structural and Foundation Damping. *Wind Engineering*, 39(6):609–628, December 2015.

[64] M.C. Bampton and R. R. Craig Jr. Coupling of Substructures for Dynamic Analyses. *AIAA Journal*, 6(7):1313–1319, July 1968. doi:10.2514/3.4741.

[65] F. Brennan and I. Tavares. Fatigue design of offshore steel mono-pile wind substructures. *Proceedings of the Institution of Civil Engineers*, 167(4):196–202, November 2011. http://dx.doi.org/10.1680/ener.14.00005.

A | Figures

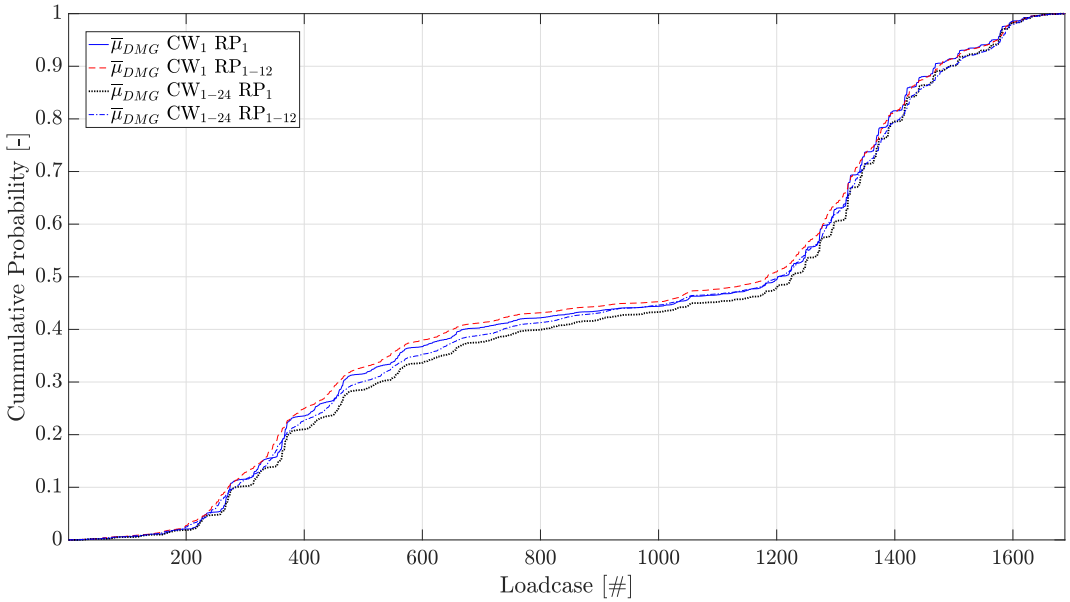

Figure A.1: *Cumulative probability curves according to different fatigue damage mean values over the* MP*.*

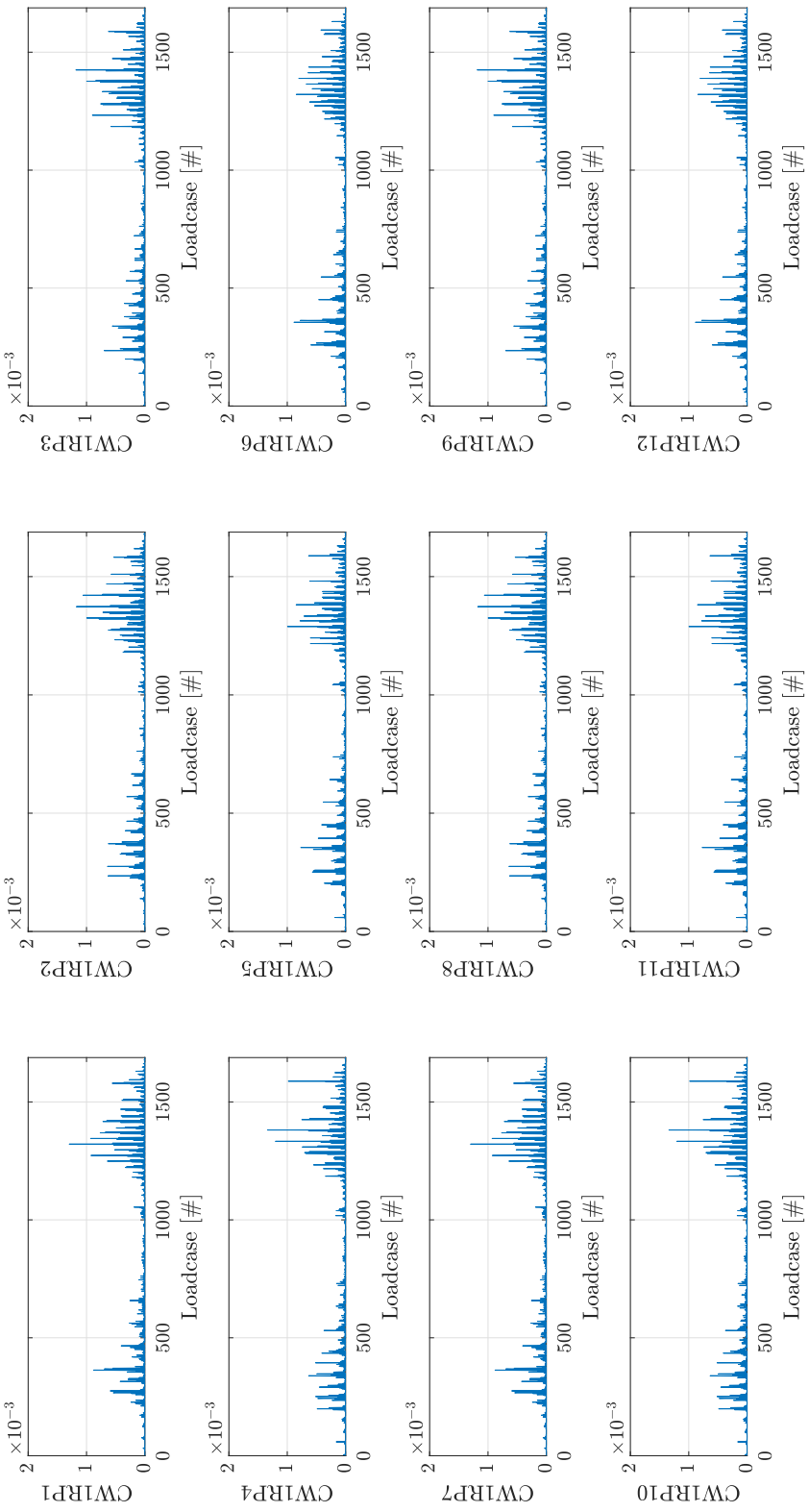

Figure A.2: *Fatigue damage standard deviation of circumferential weld (CW) per radial position and load case.*

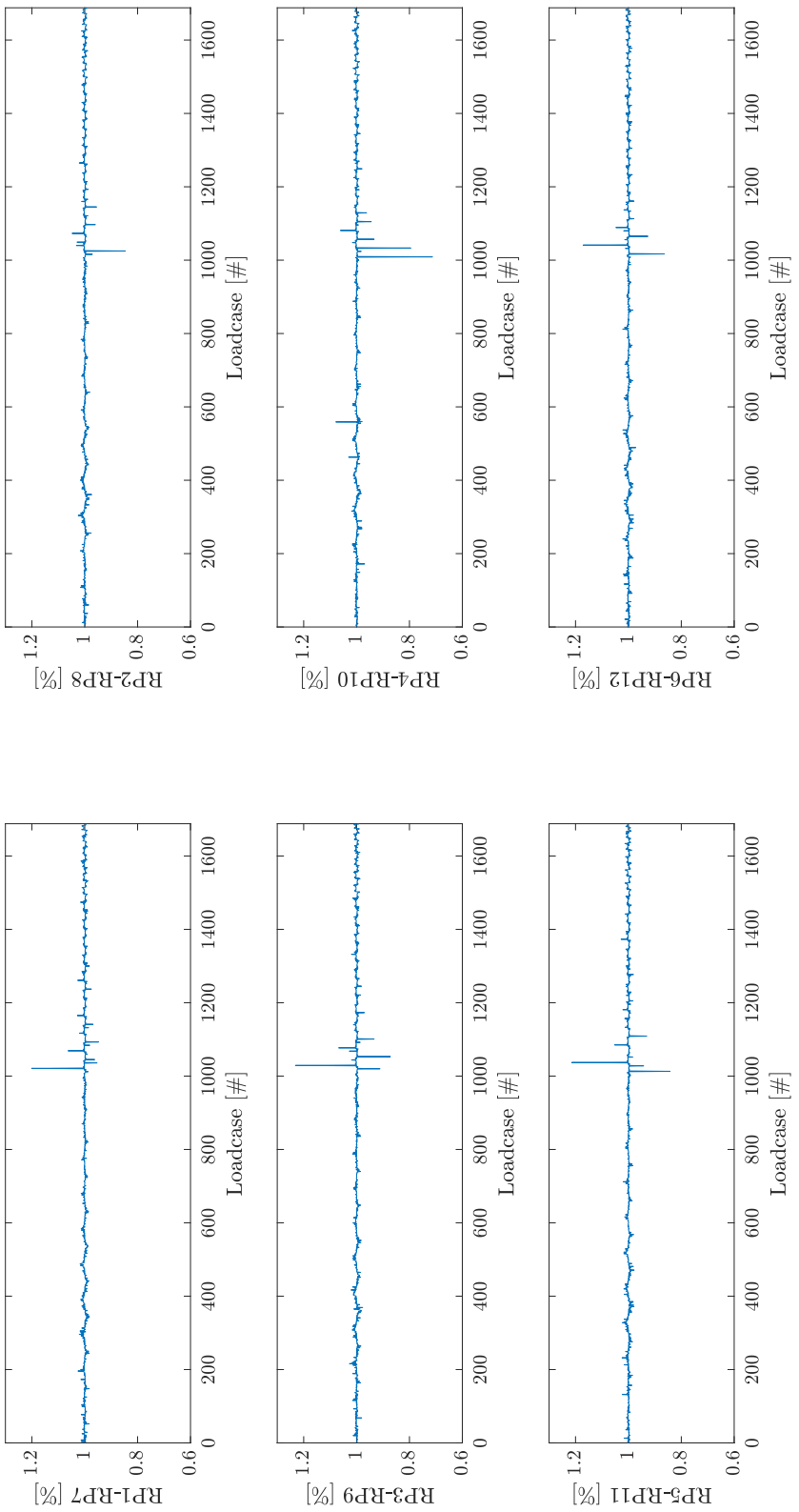

Figure A.3: *Fatigue damage standard deviation difference of opposite welds per load case.*

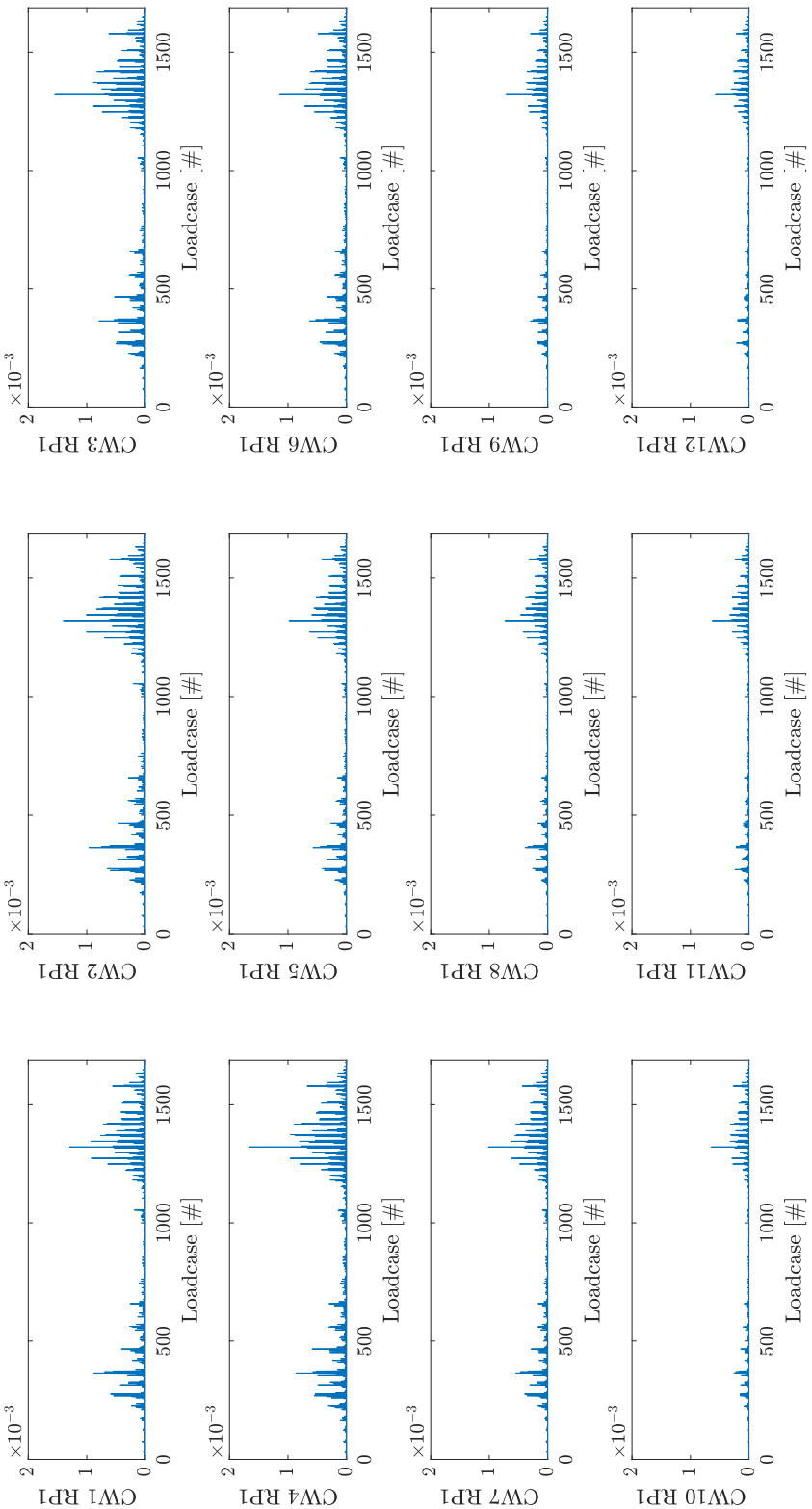

Figure A.4: *Fatigue damage standard deviation σ_{DMG} weld location CW1-12 RP1 per LC.*

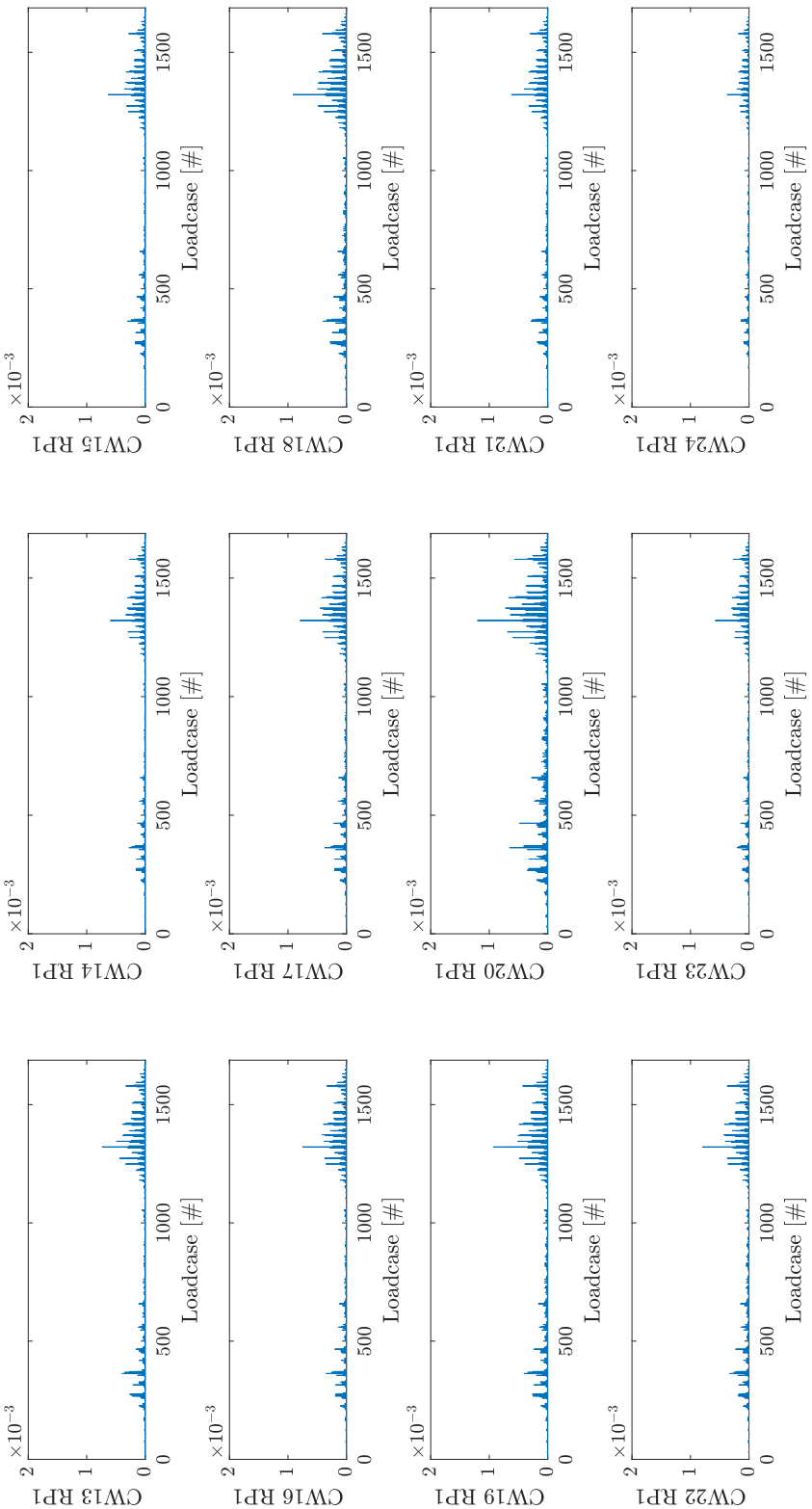

Figure A.5: *Fatigue damage standard deviation σ_{DMG} weld location CW13-24 RP1 per LC.*

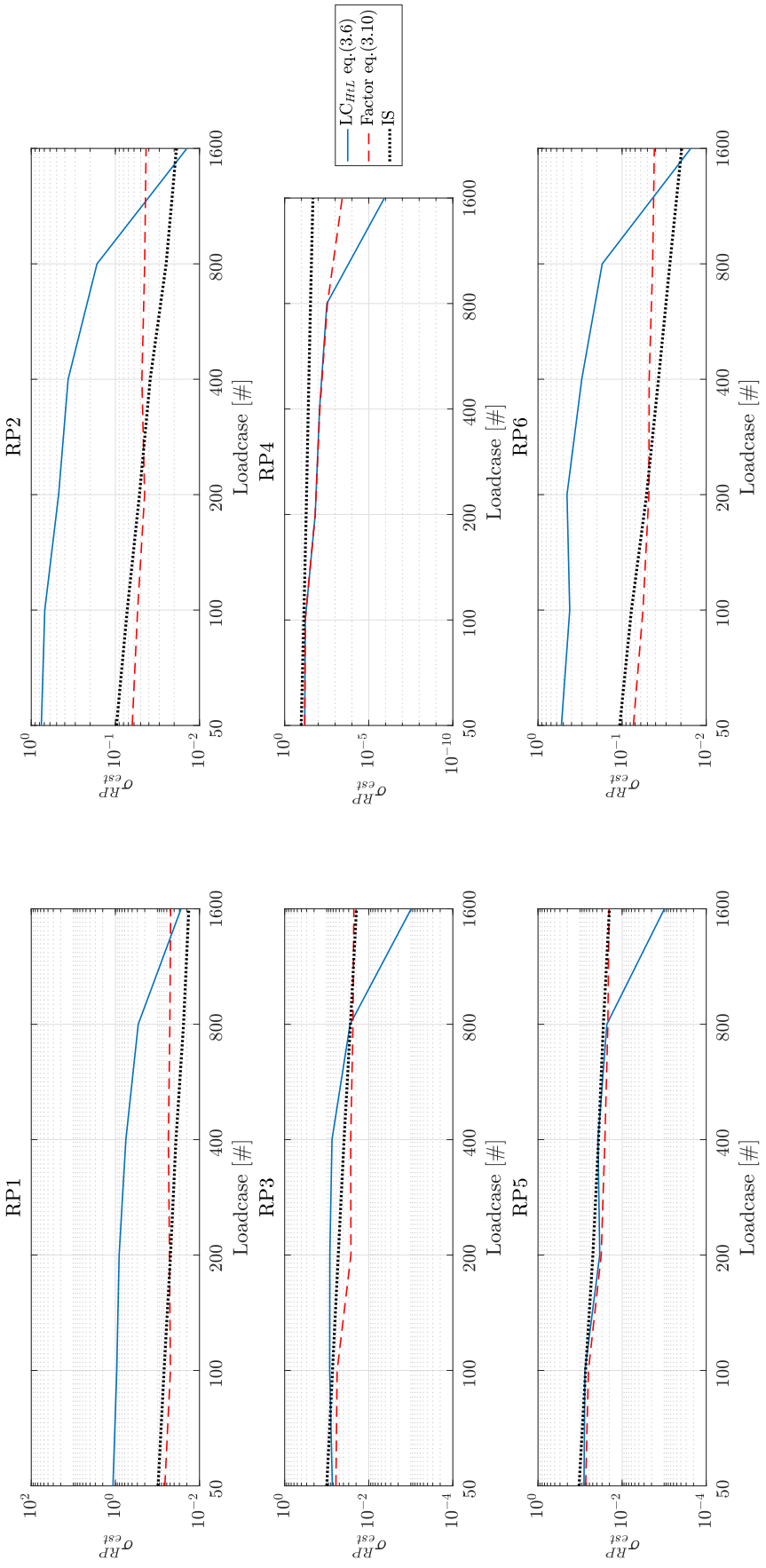

Figure A.6: *σ_{est}^{RP} comparison of approaches in sub-Section 4.1.2 for radial positions* CW1 RP1-RP6.

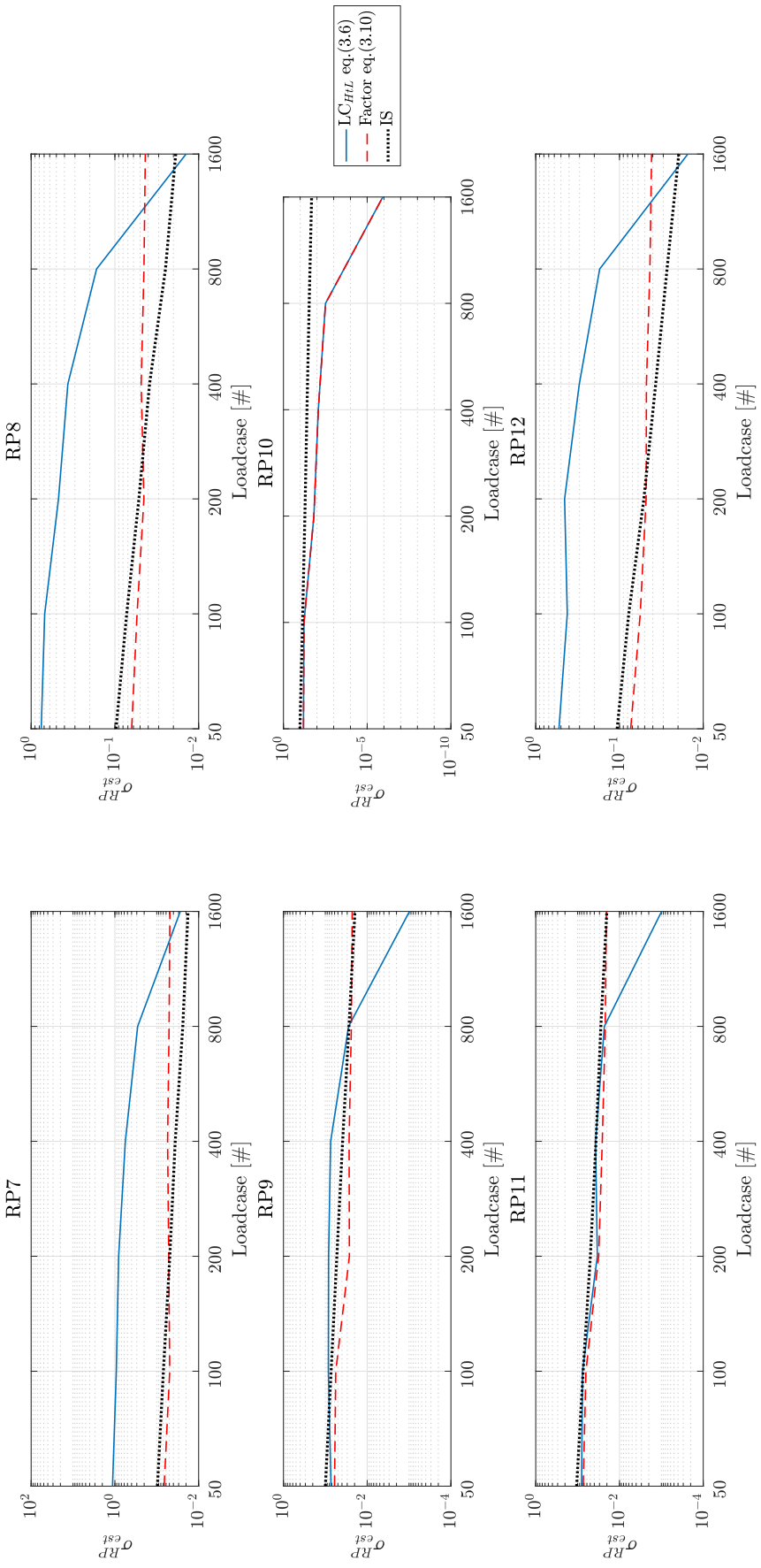

Figure A.7: *σ^{RP}_{est} comparison of approaches in sub-Section 4.1.2 for radial positions* CW1 RP7-RP12.

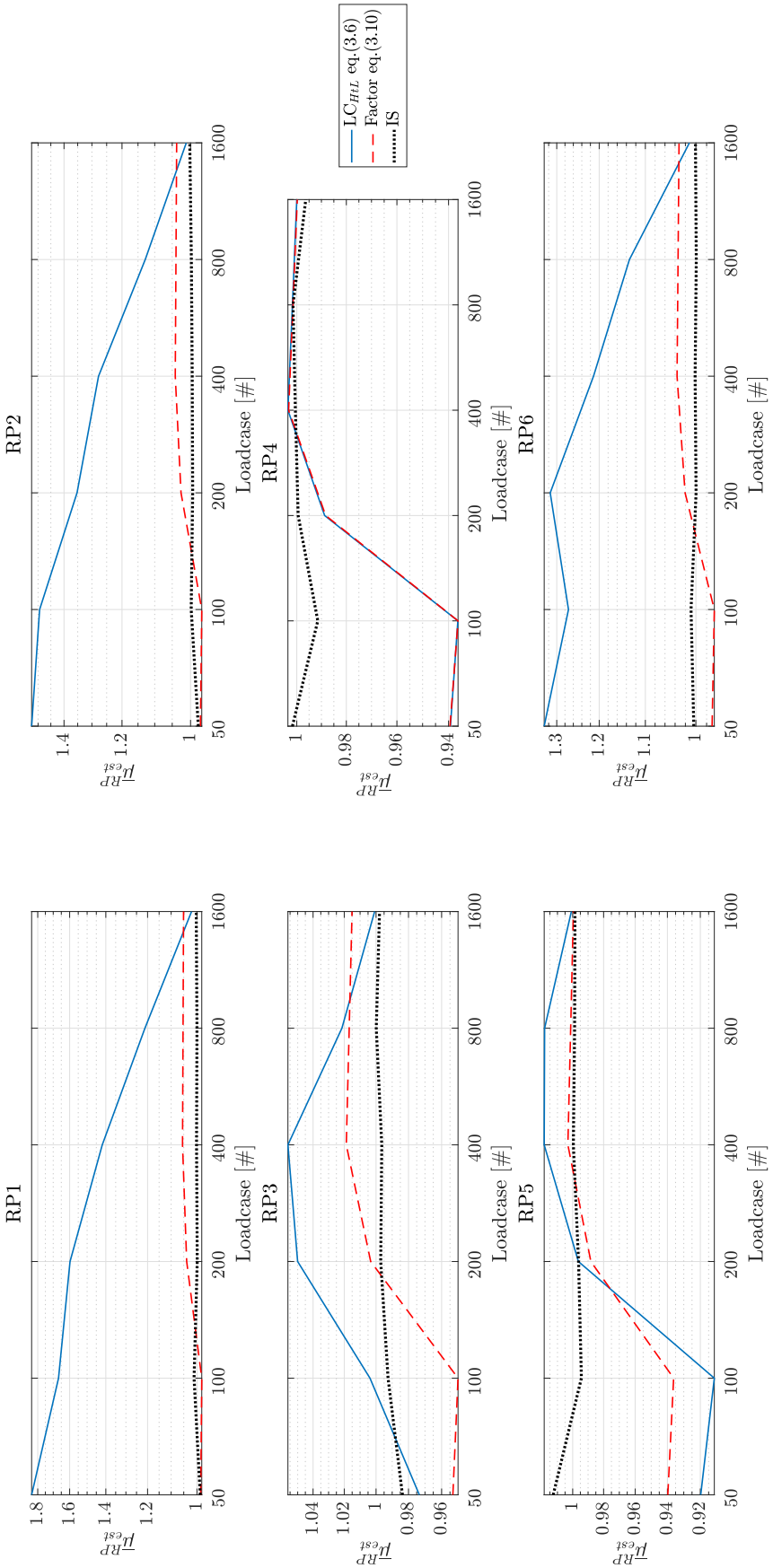

Figure A.8: *$\overline{\mu}_{est}^{RP}$ comparison of approaches in sub-section 4.1.2 for radial positions* CW1 RP1-RP6.

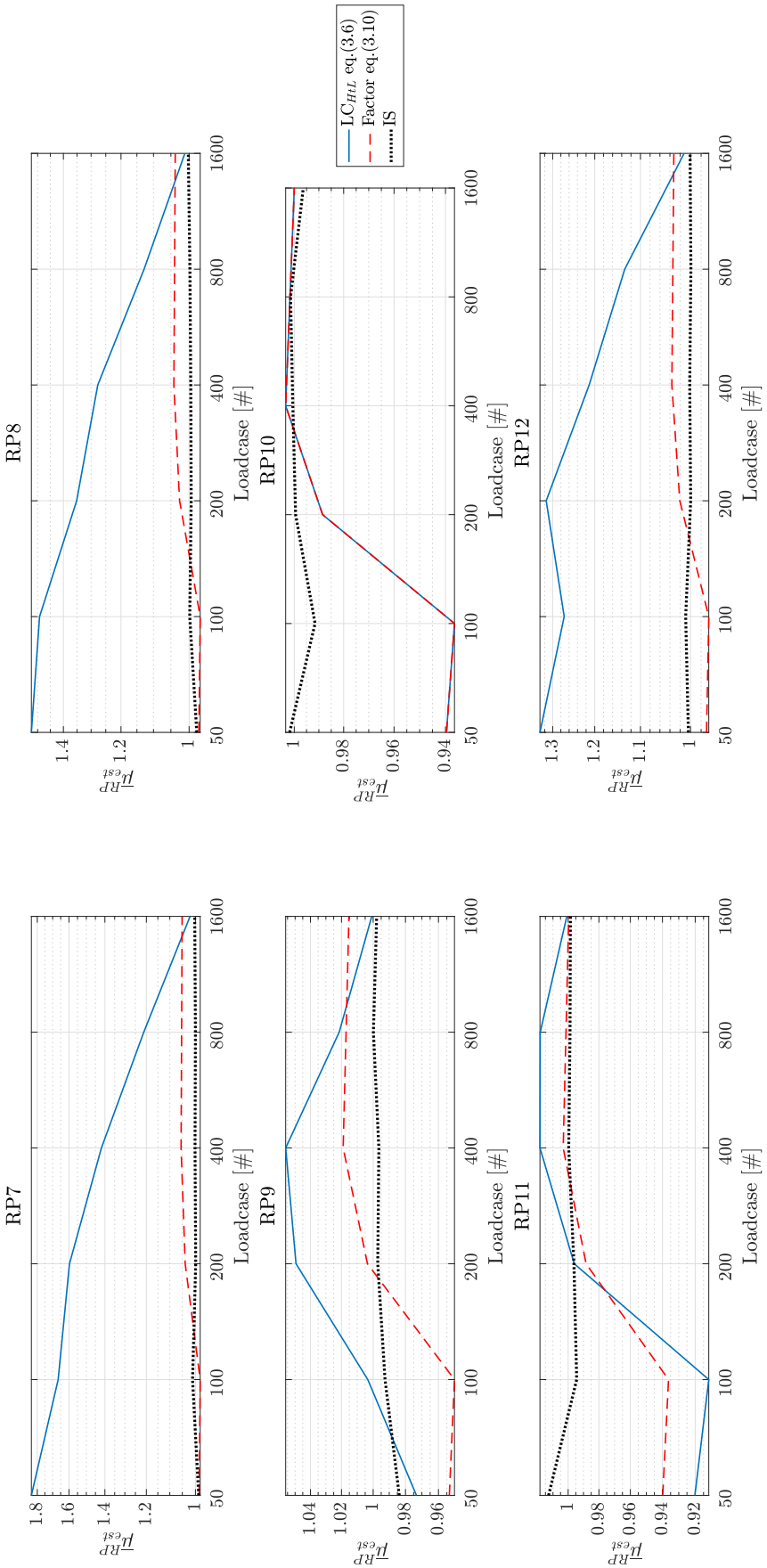

Figure A.9: *$\overline{\mu}_{est}^{RP}$ comparison of approaches in sub-Section 4.1.2 for radial positions* CW1 RP7-RP12.

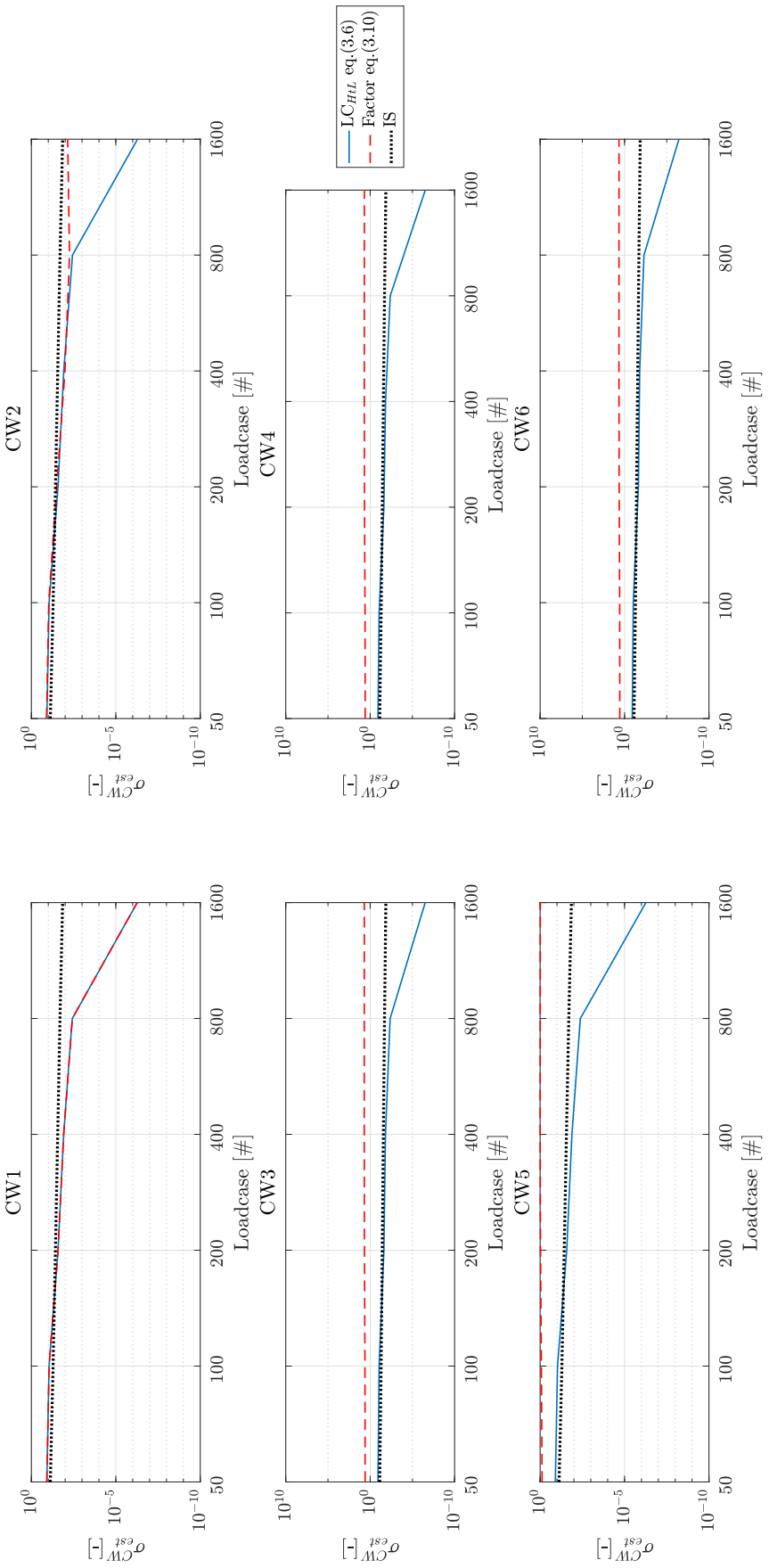

Figure A.10: *σ^{CW}_{est} comparison of approaches in sub-Section 4.1.3 for circumferential welds* CW1-6 RP1.

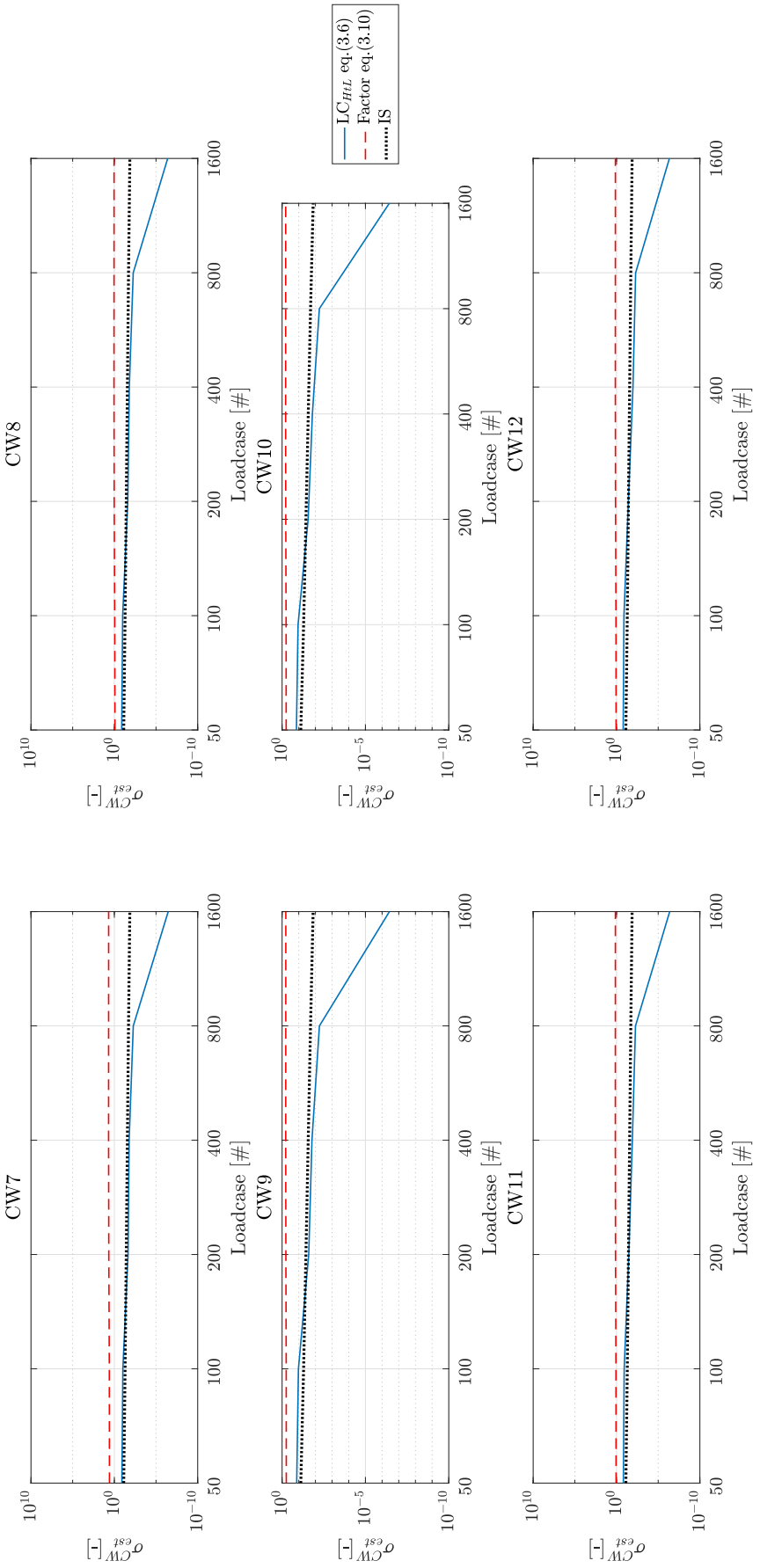

Figure A.11: *σ^{CW}_{est} comparison of approaches in sub-Section 4.1.3 for circumferential welds* CW7-12 RP1.

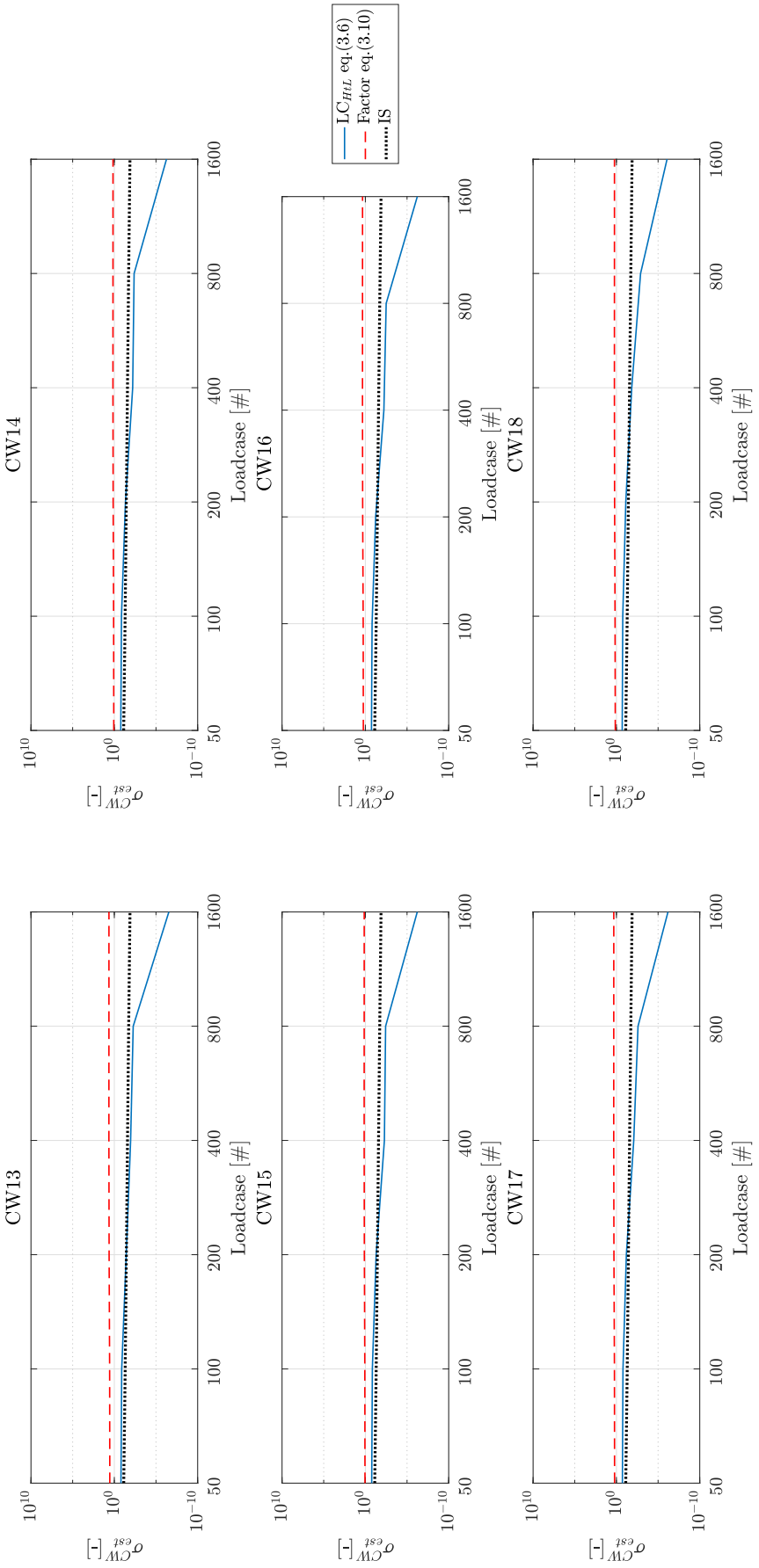

Figure A.12: σ_{est}^{CW} *comparison of approaches in sub-Section 4.1.3 for circumferential welds* CW13-18 RP1.

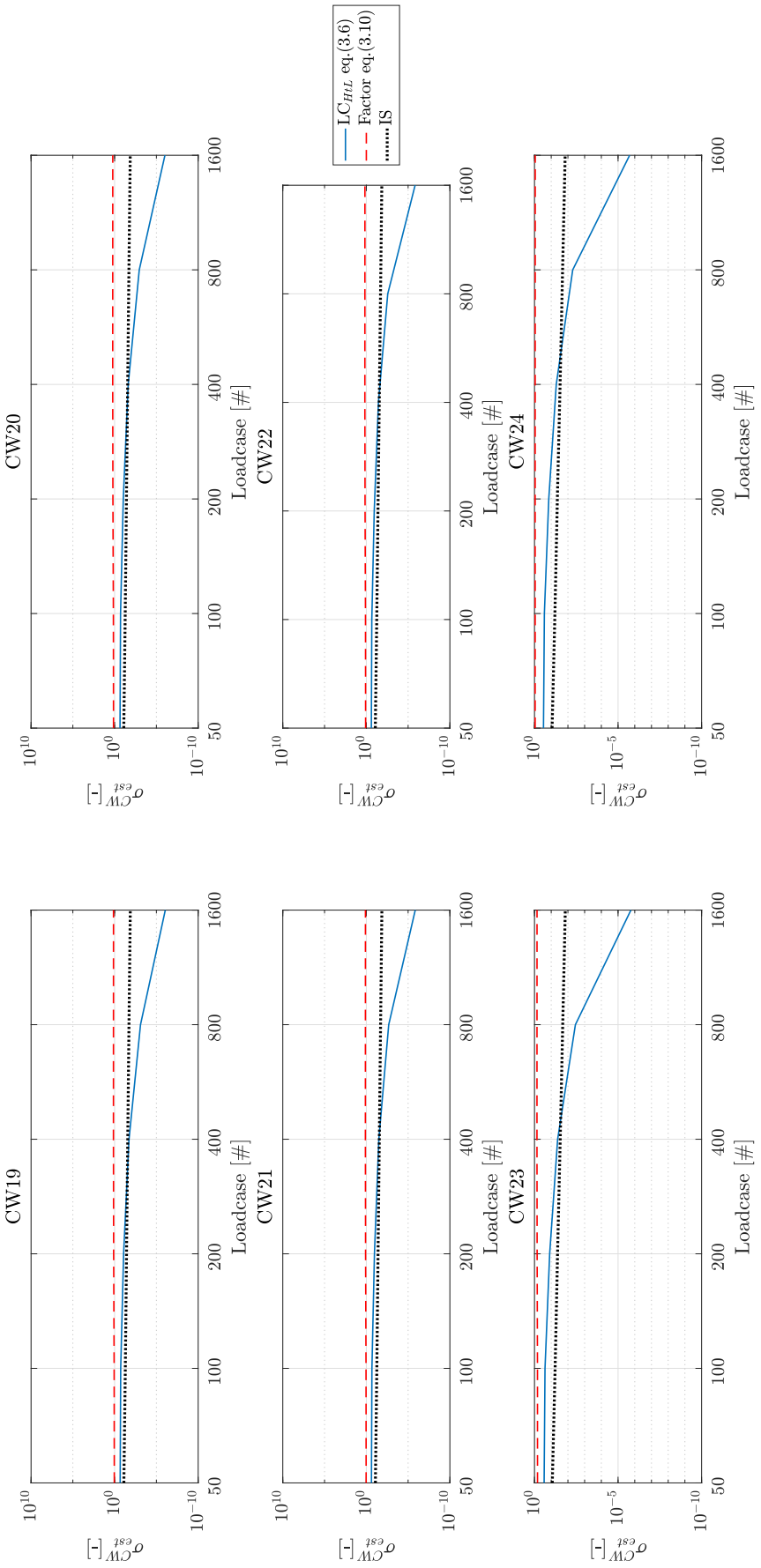

Figure A.13: *σ_{est}^{CW} comparison of approaches in sub-Section 4.1.3 for circumferential welds* CW19-24 RP1.

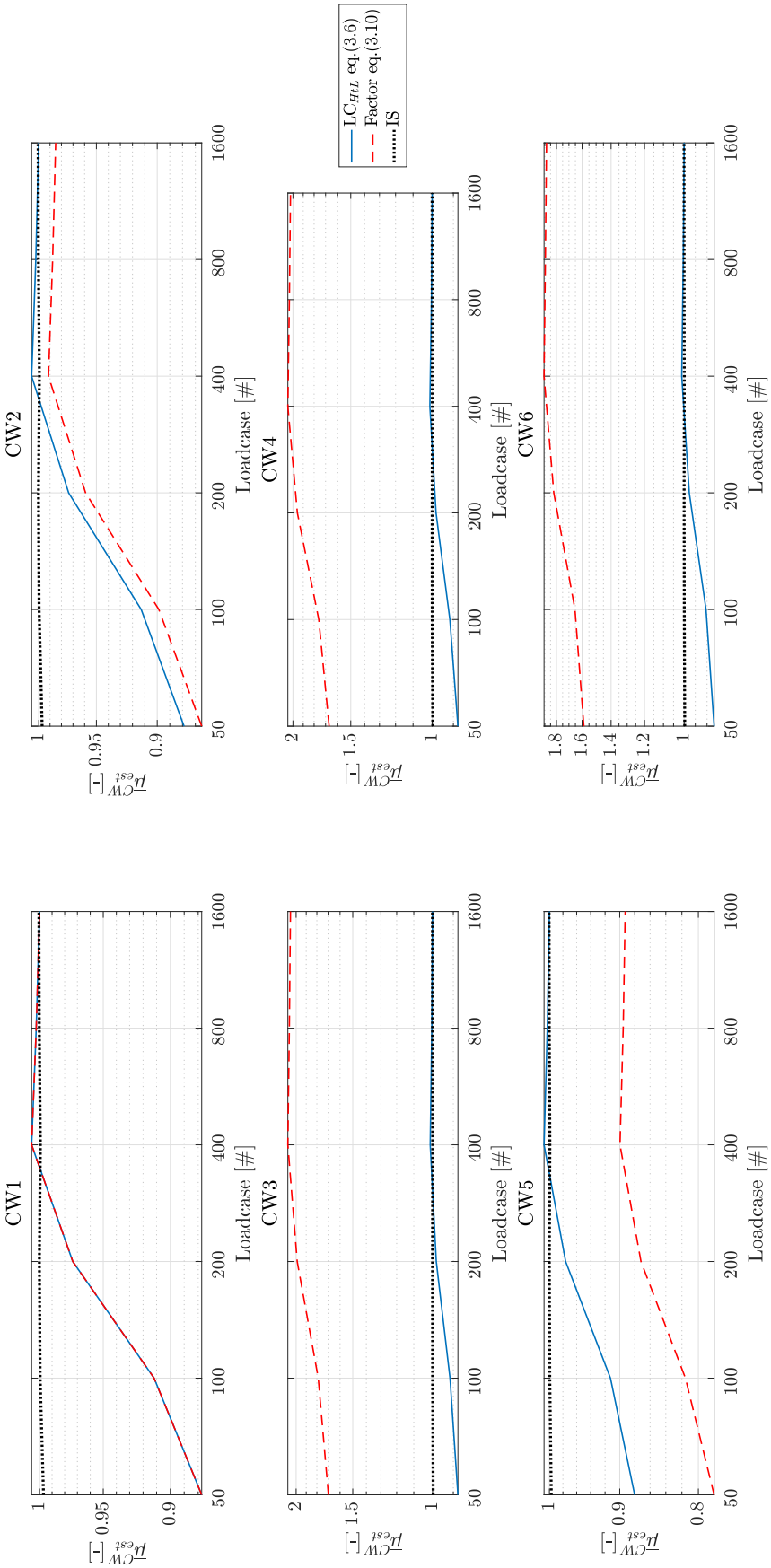

Figure A.14: *$\overline{\mu}_{est}^{CW}$ comparison of approaches in sub-Section 4.1.3 for circumferential welds* CW1-6 RP1.

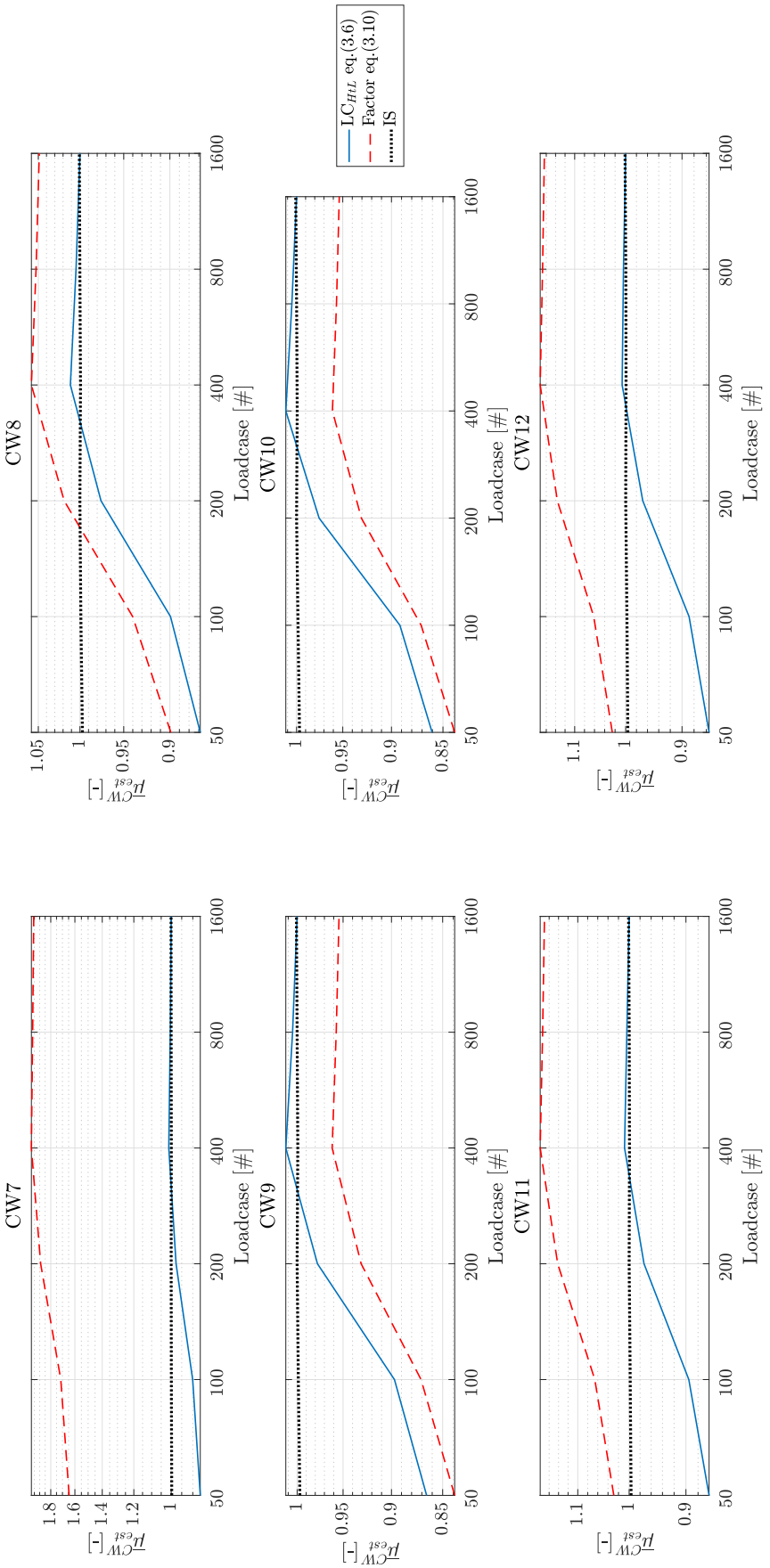

Figure A.15: *$\overline{\mu}_{est}^{CW}$ comparison of approaches in sub-Section 4.1.3 for circumferential welds* CW7-12 RP1.

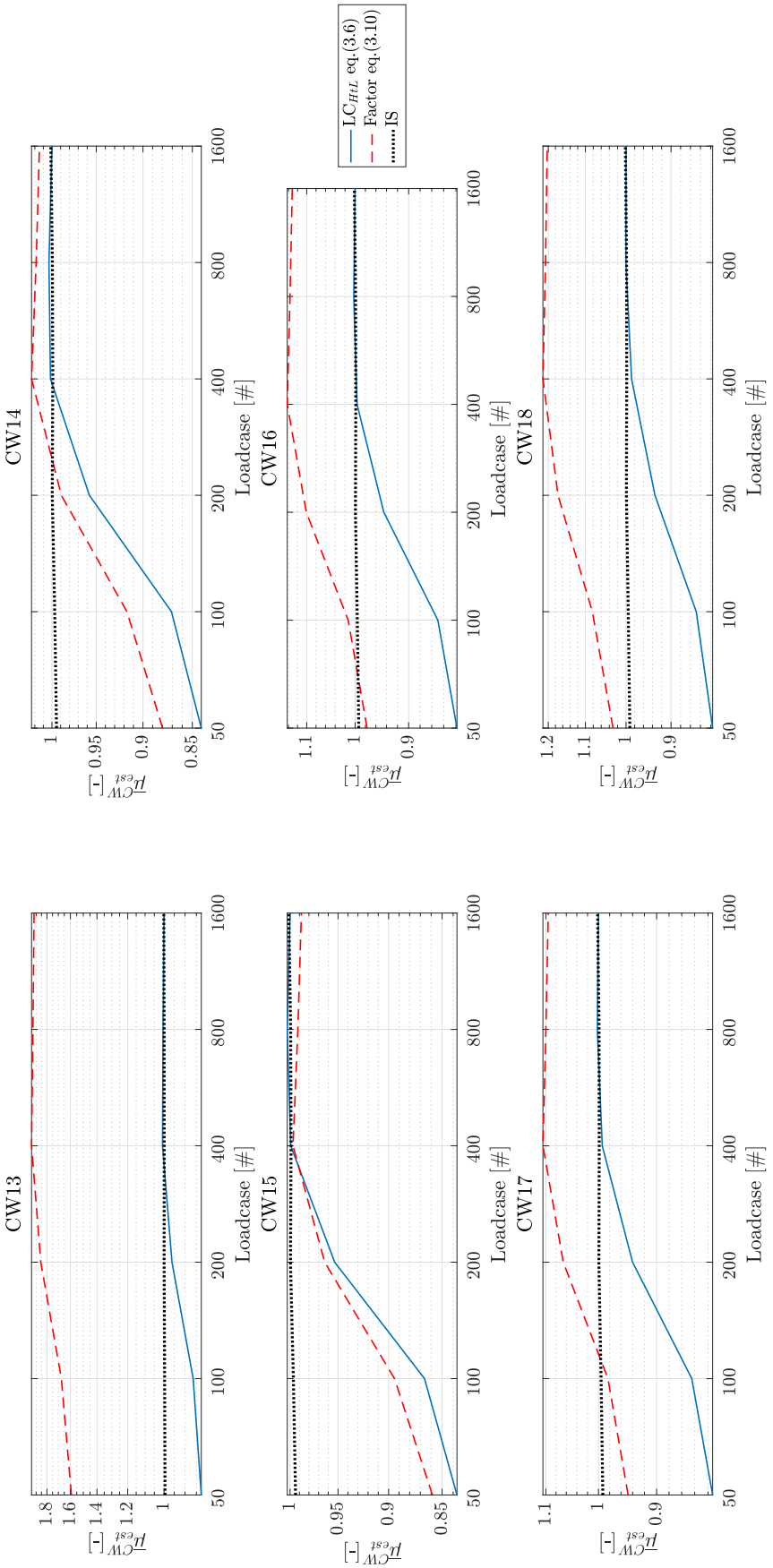

Figure A.16: *$\overline{\mu}_{est}^{CW}$ comparison of approaches in sub-Section 4.1.3 for circumferential welds* CW13-18 RP1.

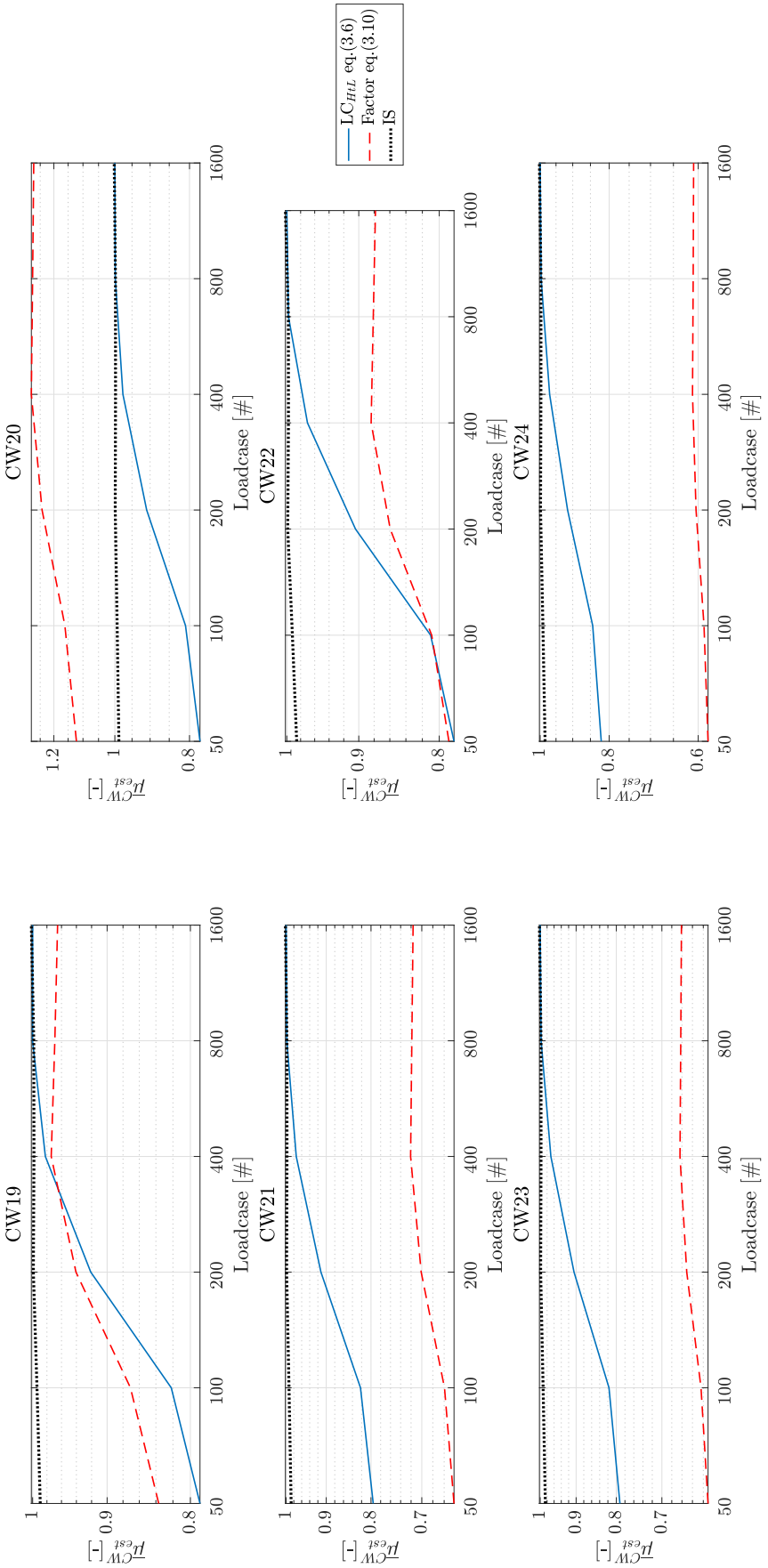

Figure A.17: *$\overline{\mu}_{est}^{CW}$ comparison of approaches in sub-Section 4.1.3 for circumferential welds* CW19-24 RP1.

Figure A.18: *Radial position and circumferential weld fatigue damage standard deviation* $\sigma_{DMG}^{CW,RP}$ *over the design set of* CW1-6 RP1-12.

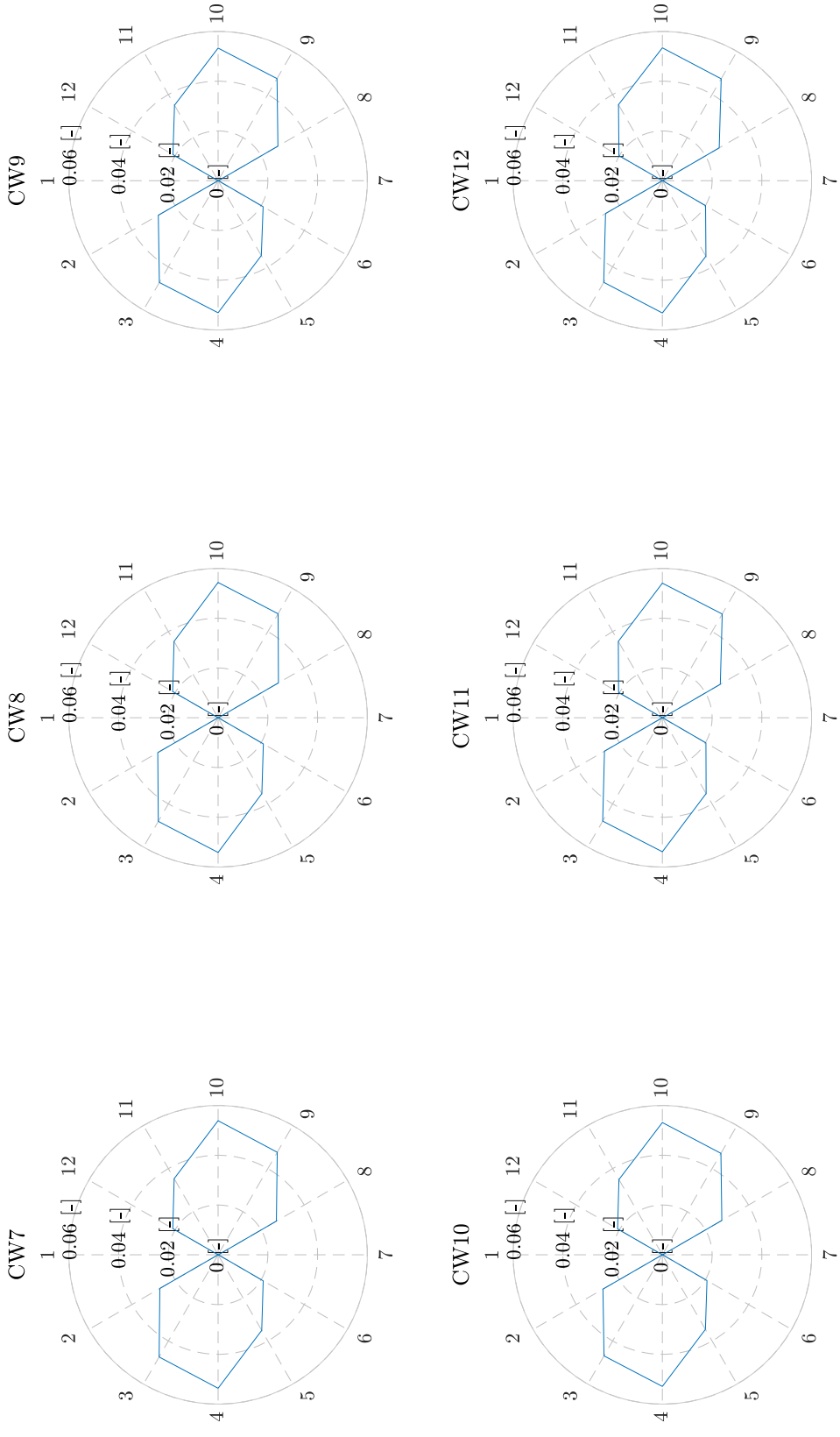

Figure A.19: *Radial position and circumferential weld fatigue damage standard deviation* σ_{DMG}^{CWRP} *over the design set of* CW7-12 RP1-12.

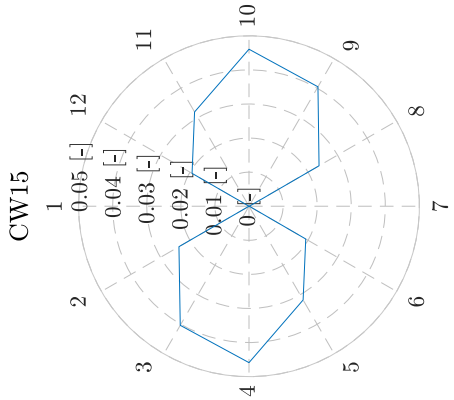

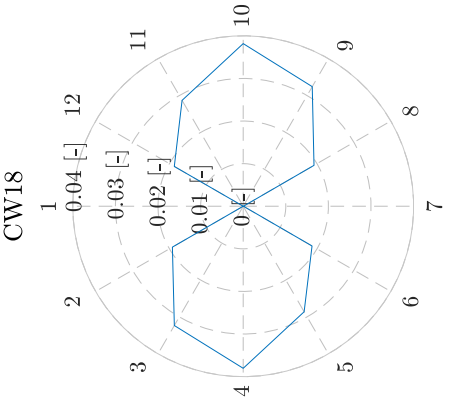

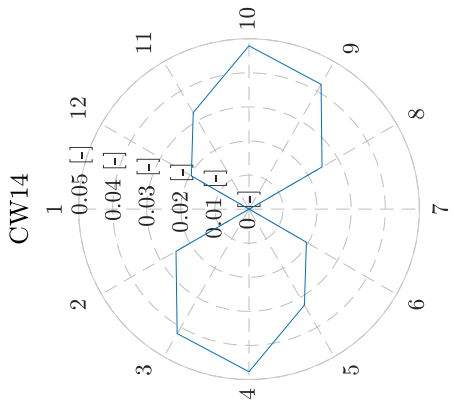

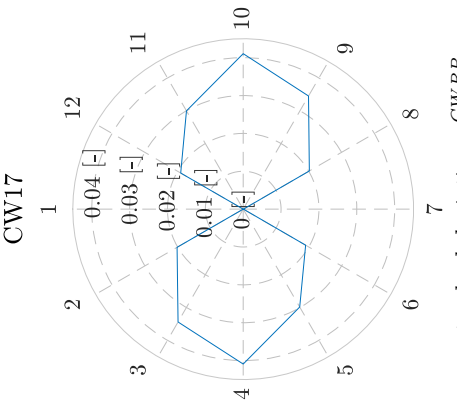

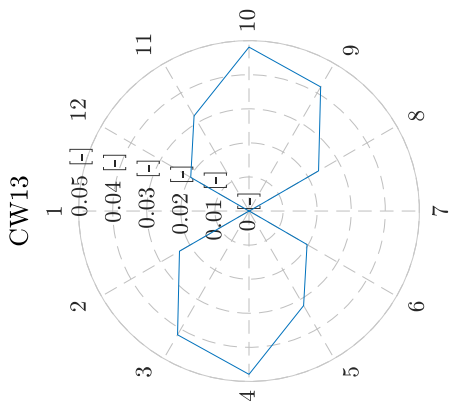

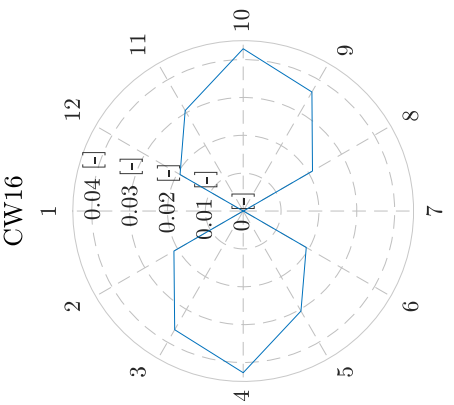

Figure A.20: *Radial position and circumferential weld fatigue damage standard deviation* σ_{DMG}^{CWRP} *over the design set of* CW13-18 RP1-12.

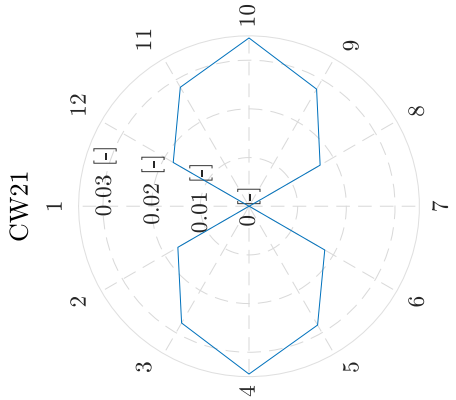

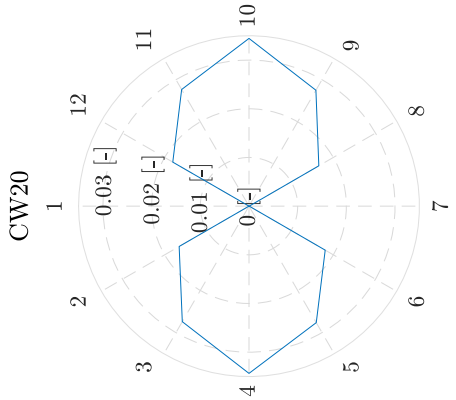

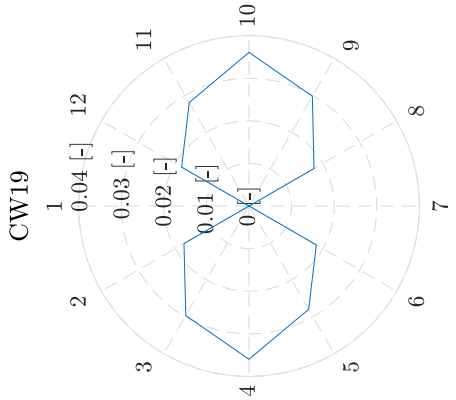

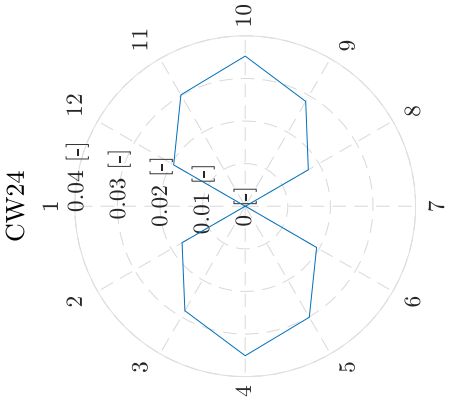

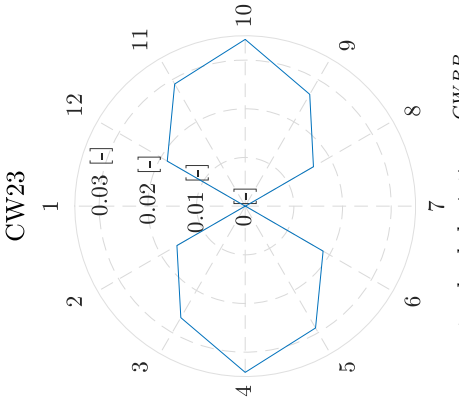

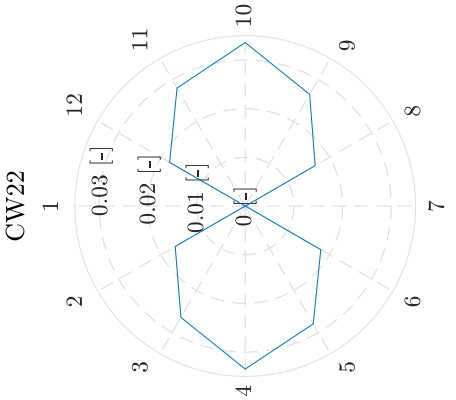

Figure A.21: *Radial position and circumferential weld fatigue damage standard deviation* $\sigma_{DMG}^{CW,RP}$ *over the design set of* CW19-24 RP1-12.

Figure A.22: *Radial position and circumferential weld fatigue damage mean value* $\overline{\mu}_{DMG}^{CW,RP}$ *over the design set of* CW1-6 RP1-12.

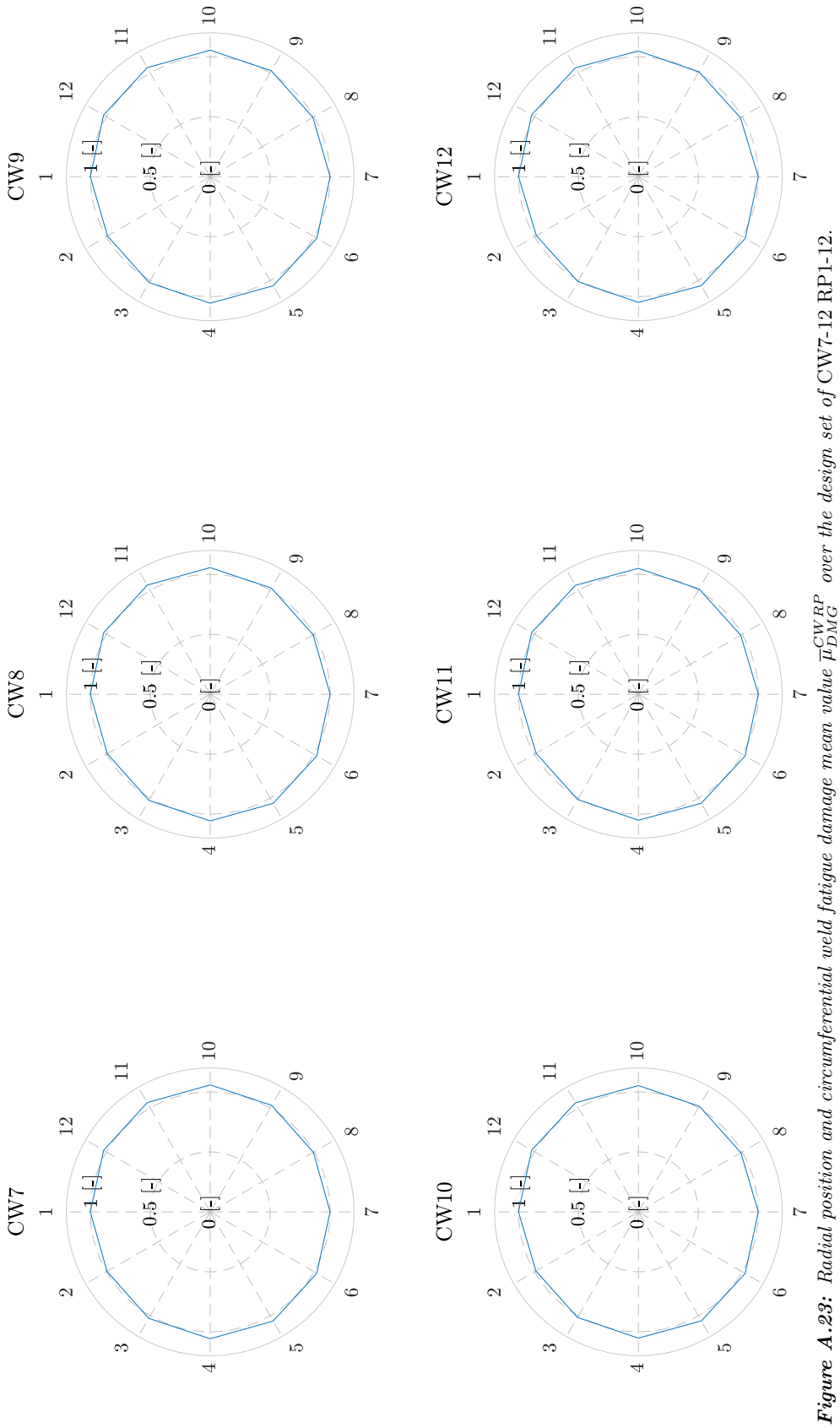

Figure A.23: *Radial position and circumferential weld fatigue damage mean value* $\overline{\mu}_{DMG}^{CW,RP}$ *over the design set of* CW7-12 RP1-12.

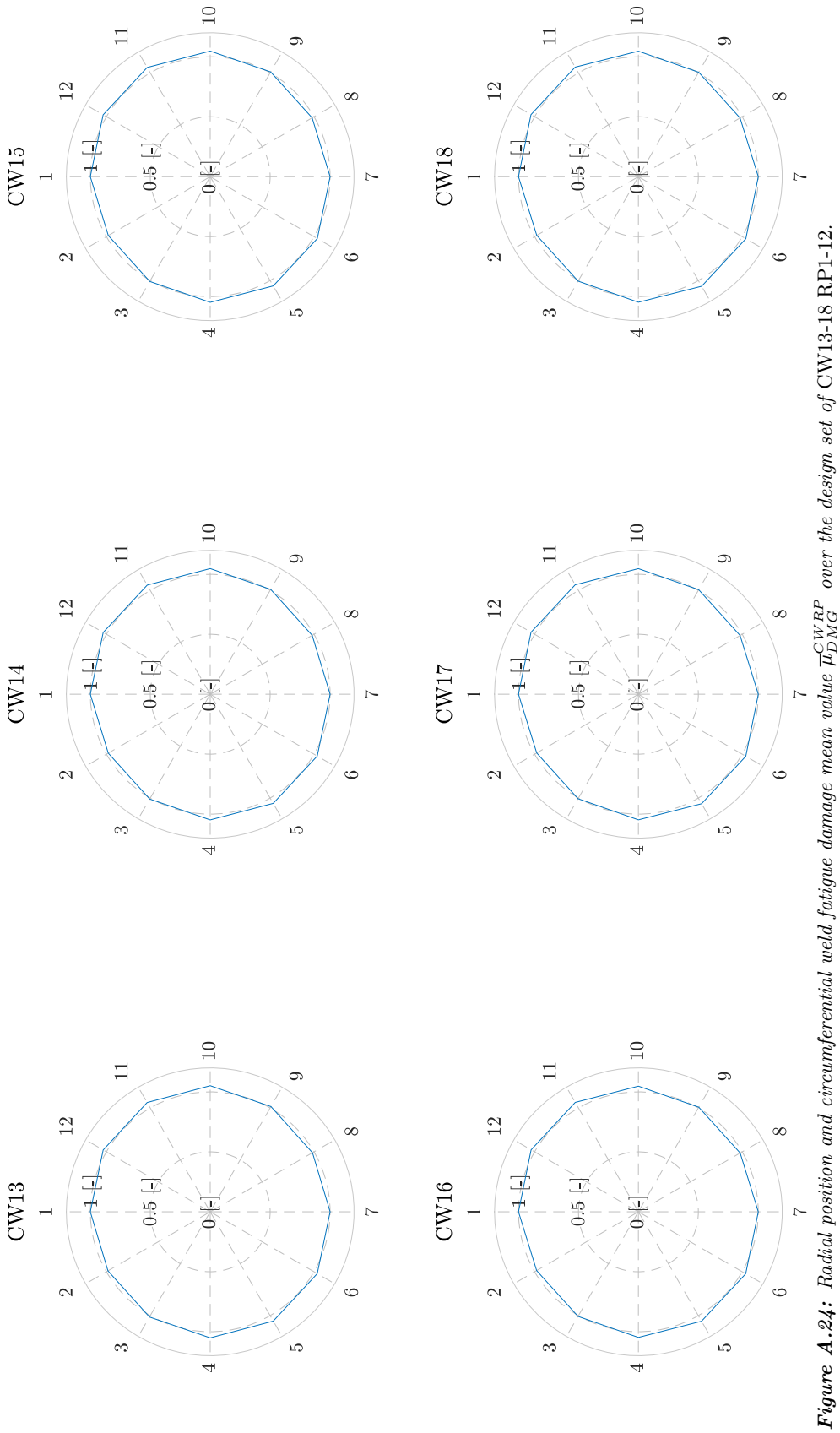

Figure A.24: *Radial position and circumferential weld fatigue damage mean value* $\overline{\mu}_{DMG}^{CW,RP}$ *over the design set of* CW13-18 RP1-12.

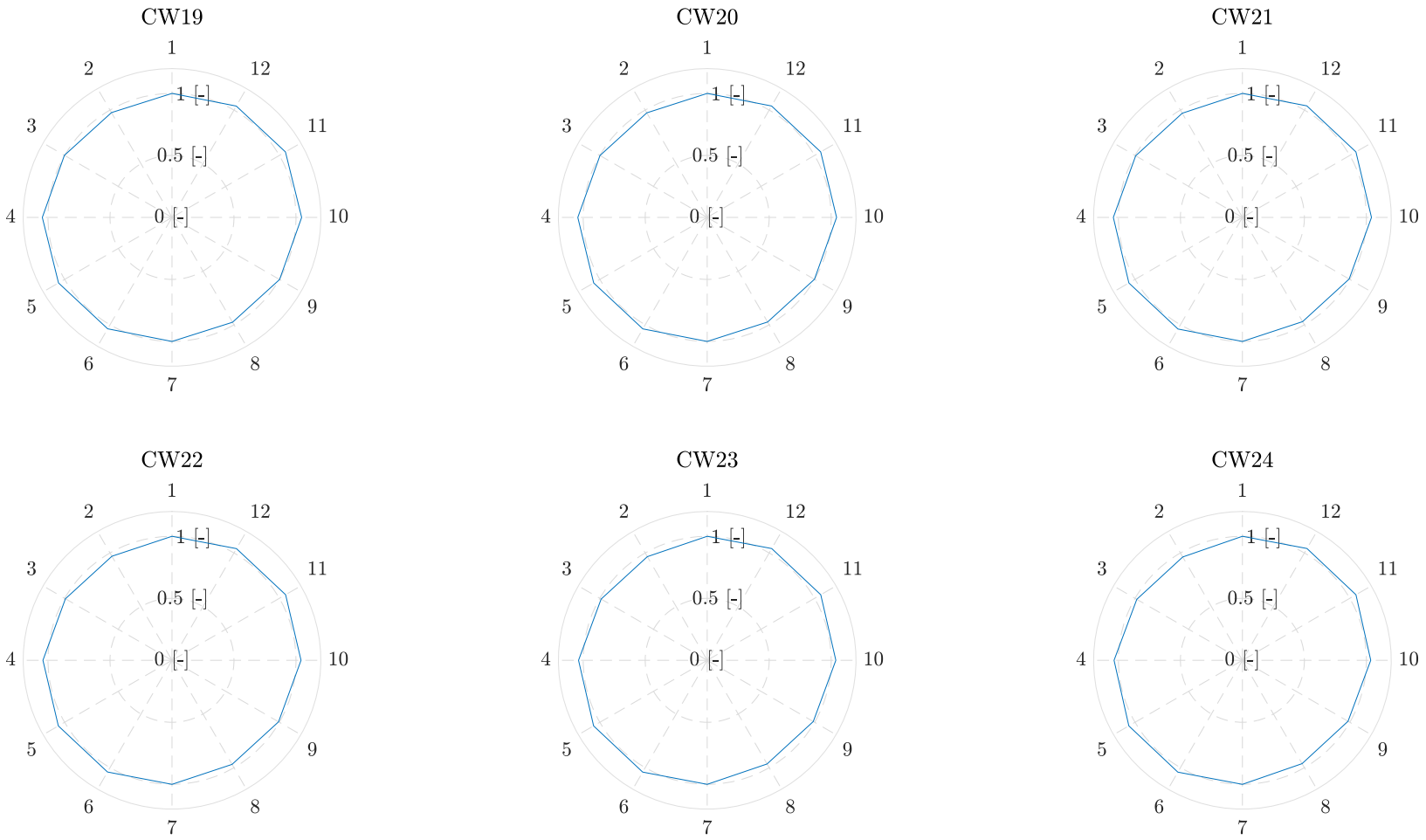

Figure A.25: *Radial position and circumferential weld fatigue damage mean value* $\overline{\mu}_{DMG}^{CWRP}$ *over the design set of* CW19-24 RP1-12.

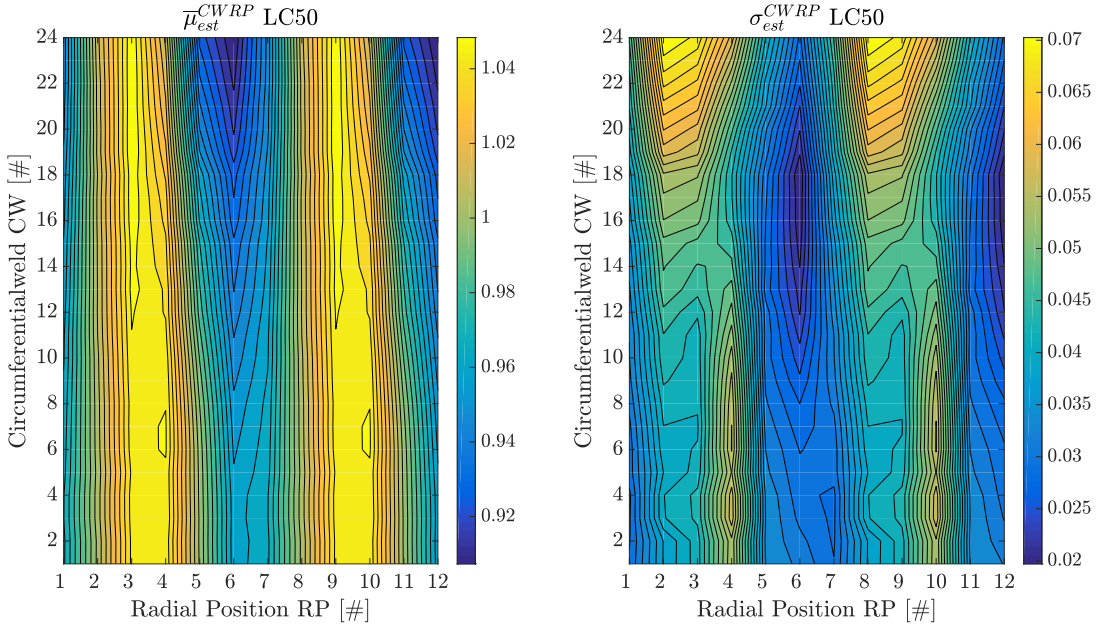

Figure A.26: *Importance Sampling fatigue damage mean value* $\overline{\mu}_{est}^{CWRP}$ *and standard deviation* σ_{est}^{CWRP} *after 50 computed* LCs *using 20 seeds.*

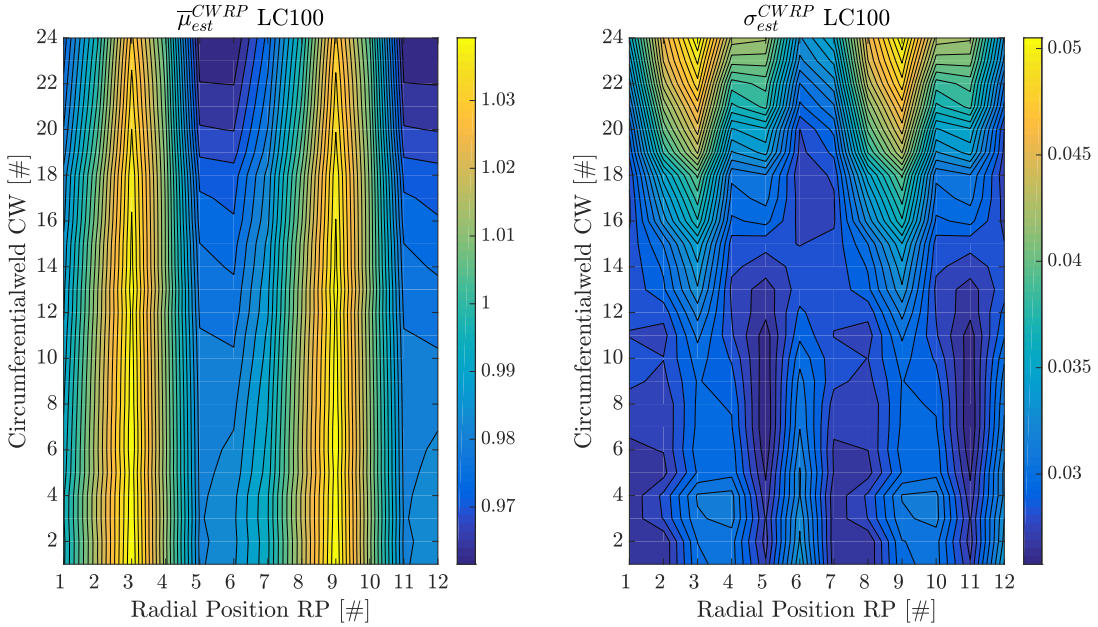

Figure A.27: *Importance Sampling fatigue damage mean value* $\overline{\mu}_{est}^{CWRP}$ *and standard deviation* σ_{est}^{CWRP} *after 100 computed* LCs *using 20 seeds.*

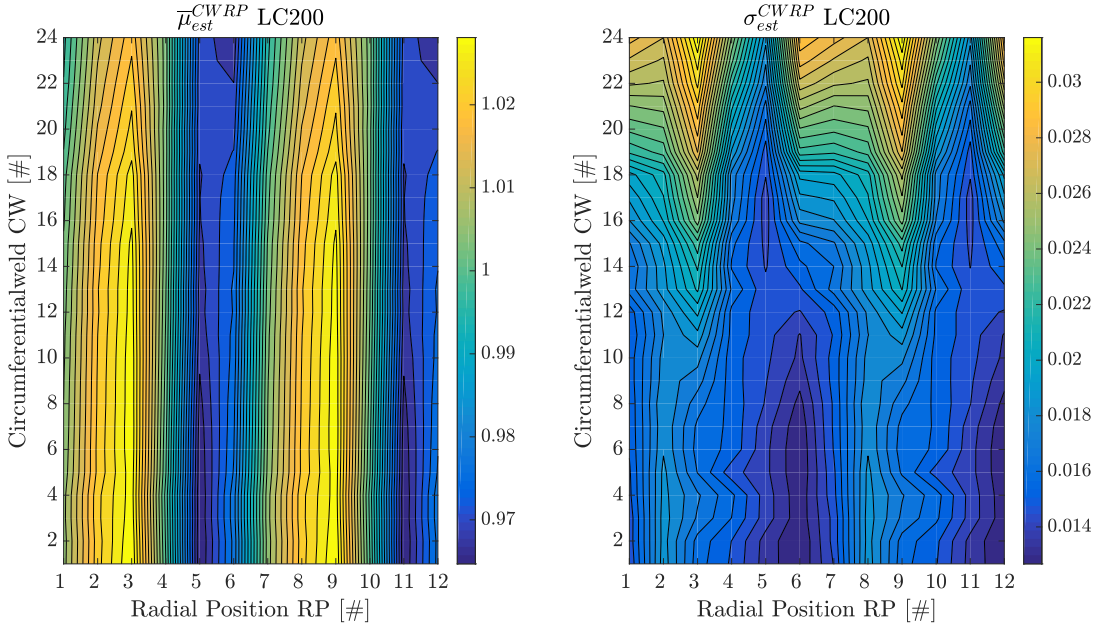

Figure A.28: *Importance Sampling fatigue damage mean value* $\overline{\mu}_{est}^{CWRP}$ *and standard deviation* σ_{est}^{CWRP} *after 200 computed* LCs *using 20 seeds.*

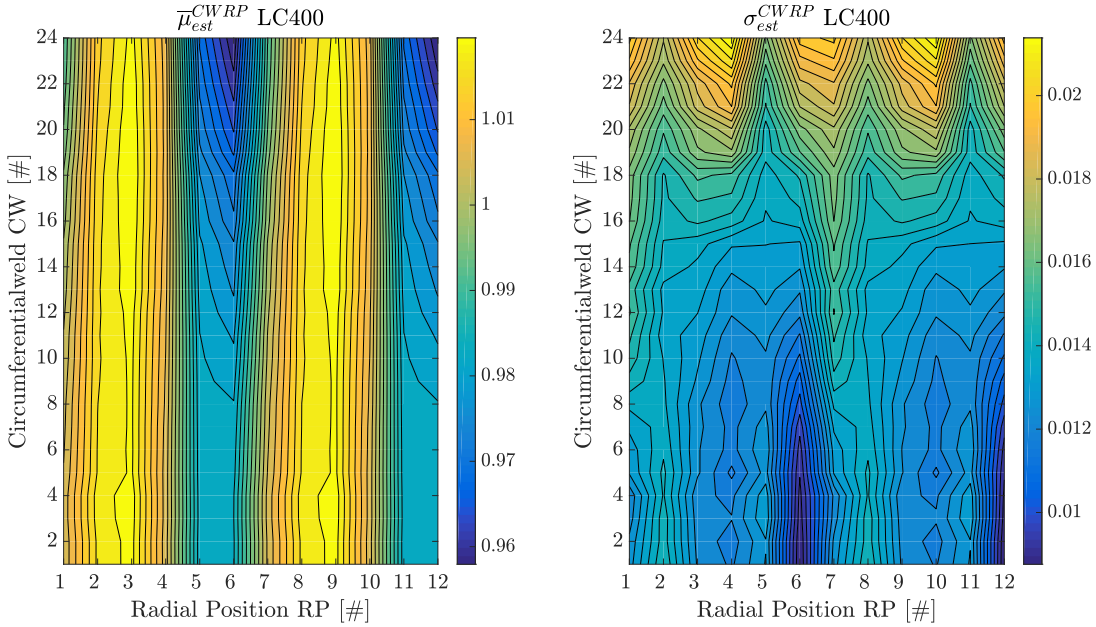

Figure A.29: *Importance Sampling fatigue damage mean value* $\overline{\mu}_{est}^{CWRP}$ *and standard deviation* σ_{est}^{CWRP} *after 400 computed* LCs *using 20 seeds.*

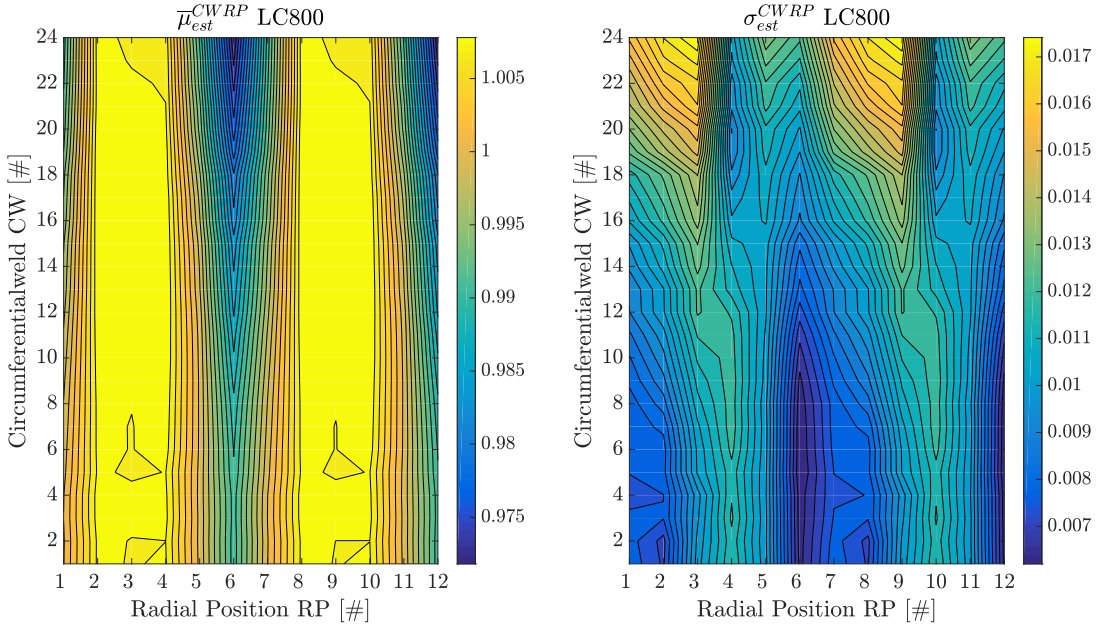

Figure A.30: *Importance Sampling fatigue damage mean value* $\overline{\mu}_{est}^{CWRP}$ *and standard deviation* σ_{est}^{CWRP} *after 800 computed* LCs *using 20 seeds.*

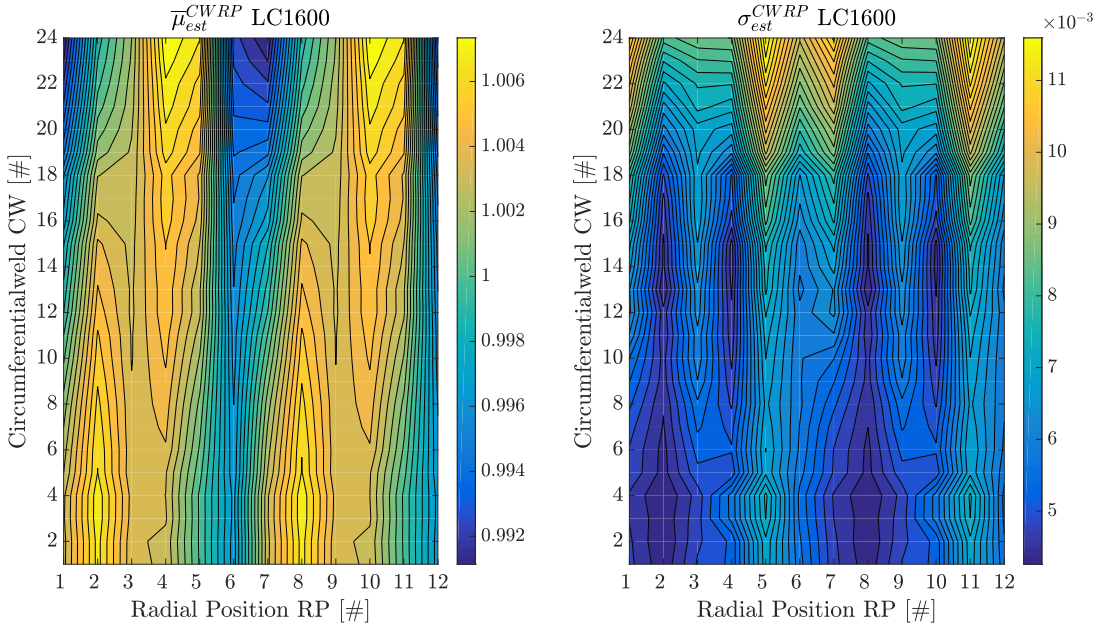

Figure A.31: *Importance Sampling fatigue damage mean value* $\overline{\mu}_{est}^{CWRP}$ *and standard deviation* σ_{est}^{CWRP} *after 1600 computed* LCs *using 20 seeds.*

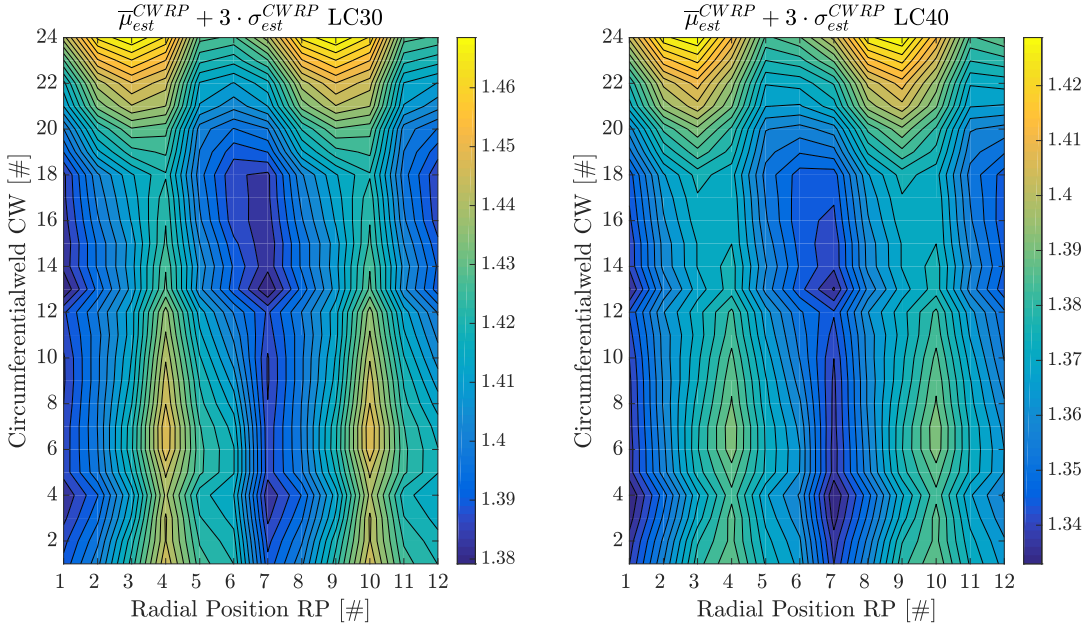

Figure A.32: *Resulting fatigue damage estimate mean $\overline{\mu}_{est}^{CWRP}$ and standard deviation $\overline{\mu}_{est}^{CWRP}$ after repeating 100 random load case selection loops for 30 and 40 computed load cases using Importance Sampling.*

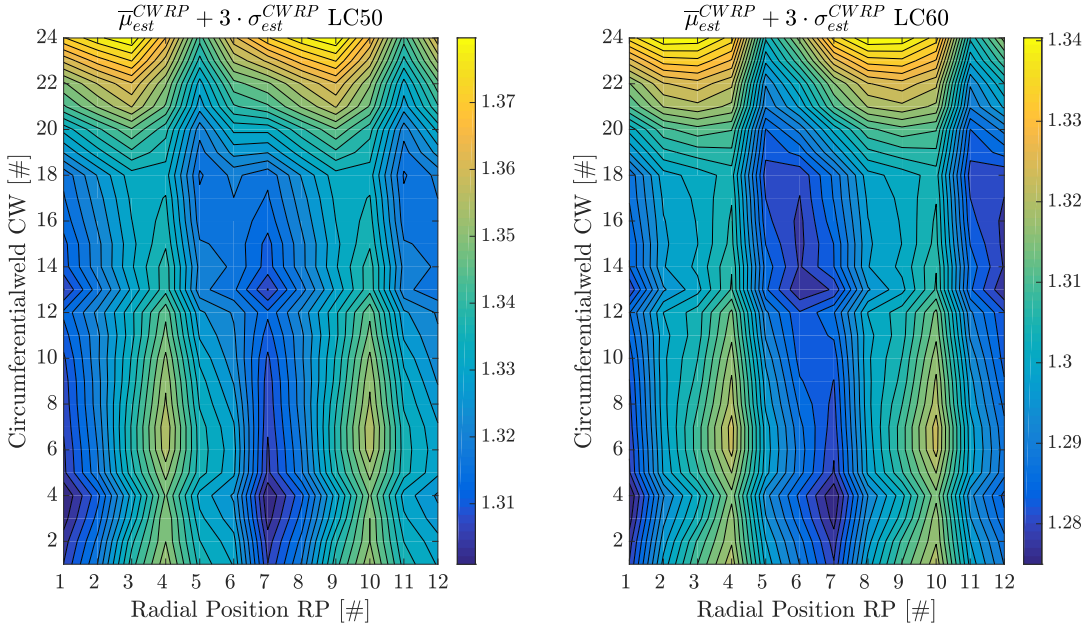

Figure A.33: *Resulting fatigue damage estimate mean $\overline{\mu}_{est}^{CWRP}$ and standard deviation $\overline{\mu}_{est}^{CWRP}$ after repeating 100 random load case selection loops for 50 and 60 computed load cases using Importance Sampling.*

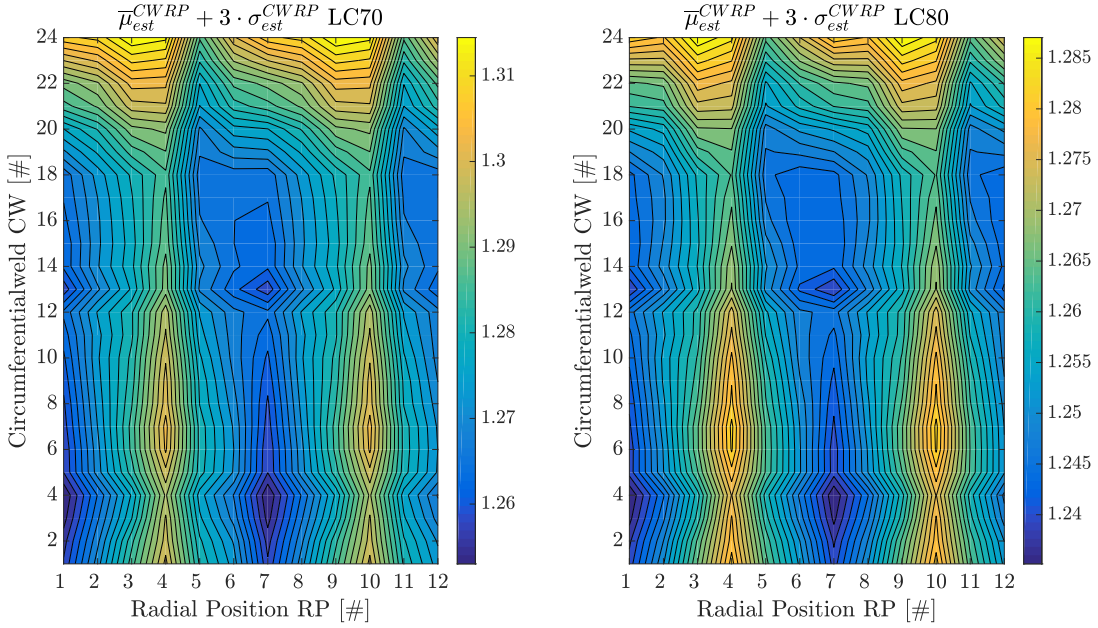

Figure A.34: *Resulting fatigue damage estimate mean $\overline{\mu}_{est}^{CWRP}$ and standard deviation $\overline{\mu}_{est}^{CWRP}$ after repeating 100 random load case selection loops for 70 and 80 computed load cases using Importance Sampling.*

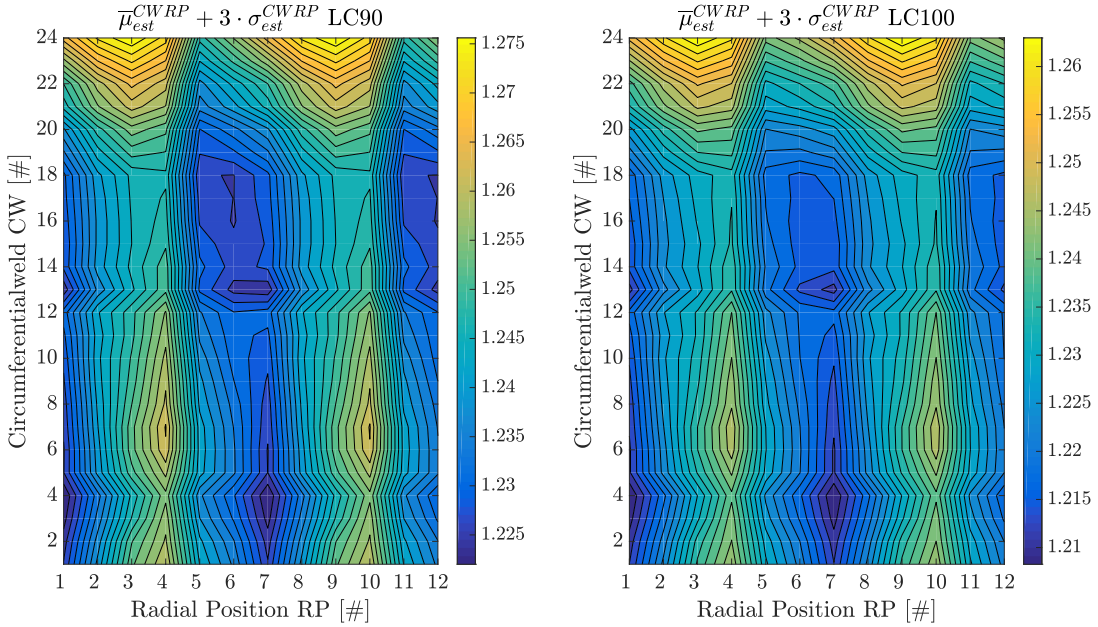

Figure A.35: *Resulting fatigue damage estimate mean $\overline{\mu}_{est}^{CWRP}$ and standard deviation $\overline{\mu}_{est}^{CWRP}$ after repeating 100 random load case selection loops for 90 and 100 computed load cases using Importance Sampling.*

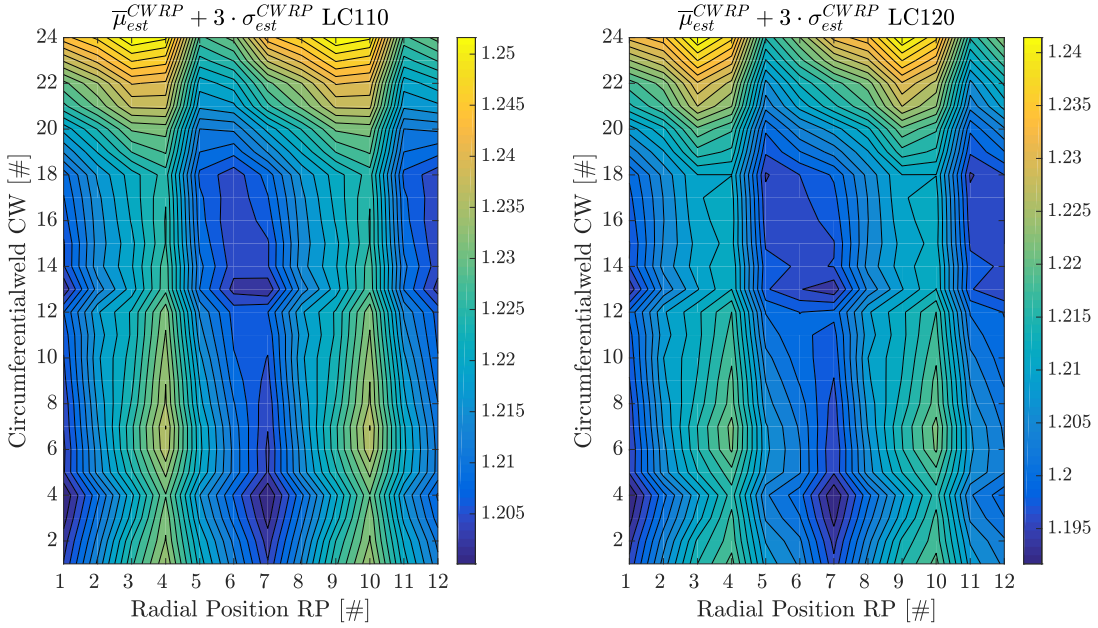

Figure A.36: *Resulting fatigue damage estimate mean $\overline{\mu}_{DMG}^{CWRP}$ and standard deviation $\overline{\mu}_{DMG}^{CWRP}$ after repeating 100 random load case selection loops for 110 and 120 computed load cases using Importance Sampling.*

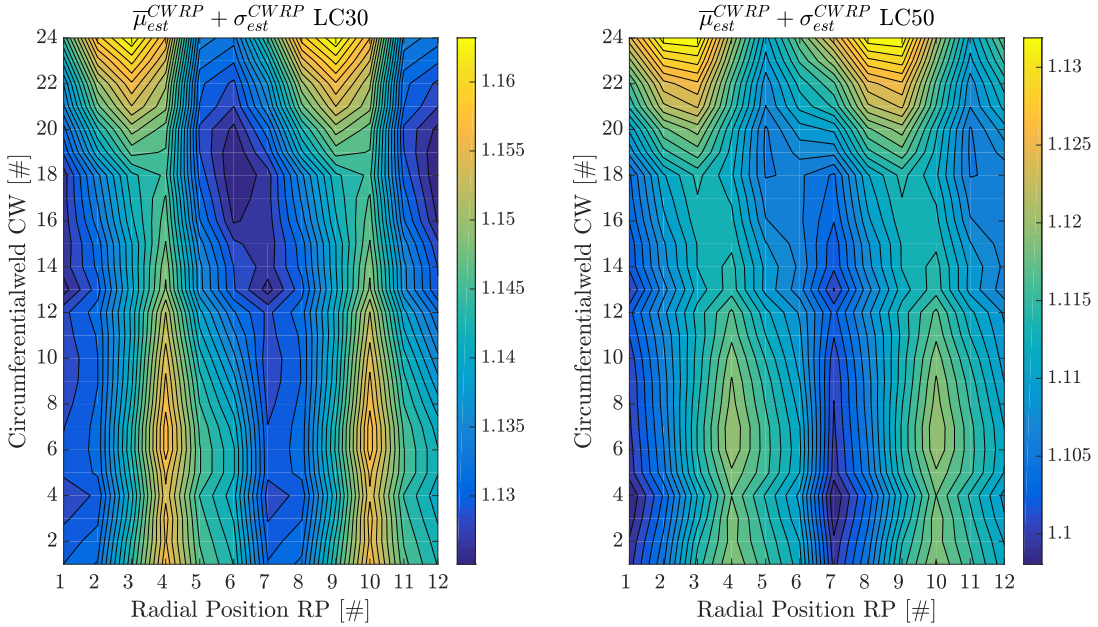

Figure A.37: *Final fatigue damage mean value $\overline{\mu}_{DMGest}^{CWRP}$ and standard deviation σ_{est}^{CWRP} combination for* GA IS FLS *reduction implementation for* LC *set 30 and 50.*

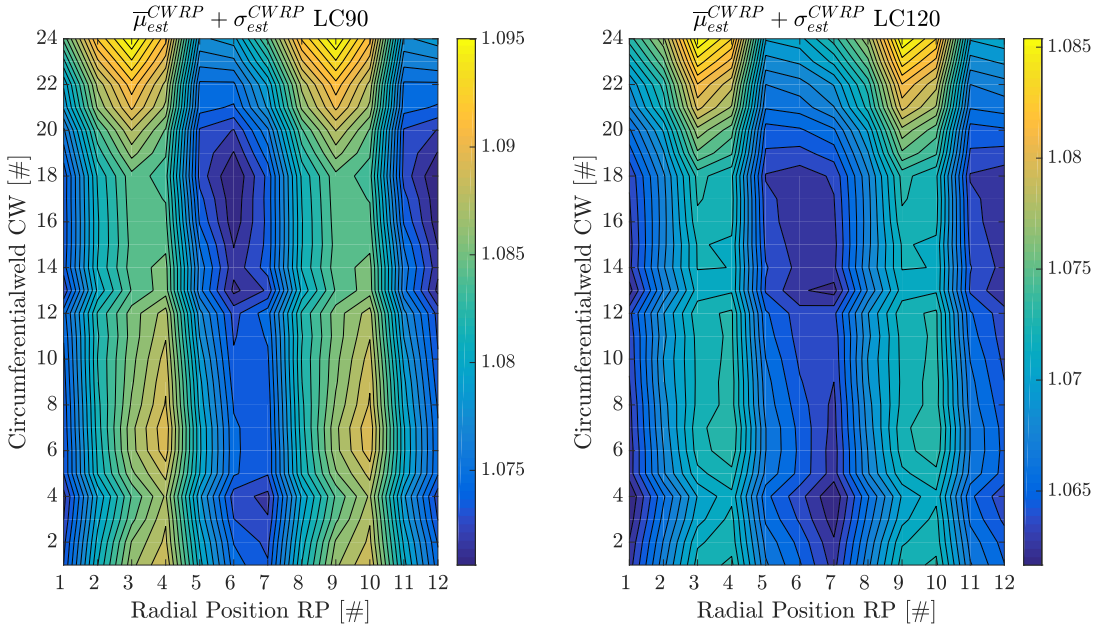

Figure A.38: *Final fatigue damage mean value* $\overline{\mu}_{DMGest}^{CWRP}$ *and standard deviation* σ_{est}^{CWRP} *combination for* GA IS FLS *reduction implementation for* LC *set 90 and 120.*